

Lorentz Nanoplasmonics for Nonlinear Generation

by

Esmail Rahimi

B.Sc., Persian Gulf University, 2014

M.Sc., Shiraz University, 2016

A Dissertation Submitted in Partial Fulfillment of the  
Requirements for the Degree of

DOCTOR OF PHILOSOPHY

in the Department of Electrical and Computer Engineering

© Esmail Rahimi, 2020

University of Victoria

All rights reserved. This dissertation may not be reproduced in whole or in part, by  
photocopying or other means, without the permission of the author.

# Lorentz Nanoplasmonics for Nonlinear Generation

by

Esmail Rahimi

B.Sc., Persian Gulf University, 2014

M.Sc., Shiraz University, 2016

Supervisory Committee

---

Dr. Reuven Gordon Supervisor Main, Supervisor  
(Department of Electrical and Computer Engineering)

---

Dr. Ilamparithi Thirumarai Chelvan, Departmental Member  
(Department of Electrical and Computer Engineering)

---

Dr. Byoung Chul Choi, Outside Member  
(Department of Physics & Astronomy)

## ABSTRACT

Plasmonic metasurfaces enable functionalities that extend beyond the possibilities of classical optical materials and as a result, have gained significant research interest over the years. This thesis aims towards introducing plasmonic metamaterials and metasurfaces, a two-dimensional subset of metamaterials. The thesis also provides insights into the nonlinear optical responses from subwavelength metallic nanostructures manifesting as extraordinary physical phenomenon like the second harmonic generation (SHG).

The hydrodynamic Drude model is a theory that characterizes electron conduction in a hydrodynamic way to predict optical responses of metals. The thesis discusses the various contributions to the second-order optical nonlinearities from the terms in the hydrodynamic model: Coulomb, convection, and the Lorentz magnetic force. The significance of these terms, specifically the Lorentz magnetic term, is validated in contrast with existing research. The details of the work carried out to achieve a significant contribution to SHG from the Lorentz magnetic term are provided. A dominant Lorentz magnetic force for SHG was achieved through engineering T-shaped aperture arrays milled into a thin gold film. The dimensions of these structures were tuned for fundamental wavelength resonance. The structures exhibit both magnetic and electric field enhancements at the plasmonic resonance.

Furthermore, a revised theoretical model is developed to accurately predict both linear and nonlinear optical responses of metamaterials. The model is based on the hydrodynamic Drude model and nonlinear scattering theory. Results from the finite difference time domain simulations performed on the metasurface are presented. It is observed that the T-shaped structure provides 65% greater nonlinear generation from the Lorentz magnetic term than the sum of the other two hydrodynamic terms. The influence of incident beam polarization on SHG conversion efficiency was also

investigated. It was discovered that even though the contributions of hydrodynamic (Coulomb and convection) terms are maximum at  $0^\circ$  and  $90^\circ$ , the metasurface shows maximum SHG intensity at  $45^\circ$  which indicates a dominant Lorentz magnetic term. Experimental validation was performed using the fabricated metasurface and a good agreement between the experiment and theoretical calculations was observed.

Another aspect of the magnetic Lorentz force contribution, the Bethe's aperture theory, was evaluated for a circular aperture at off-normal incident light. It is shown that the Lorentz force dominates the SHG by an order of magnitude at angled incidence where the generation is maximized. The angular dependence was observed to match the magnetic and electric dipole interaction effects as predicted from Bethe's theory. The revised theory developed in this thesis predicts the linear and nonlinear optical responses of metamaterials including their angular dependency. The analysis and numerical calculations for a circular aperture agree well with past experiments.

To conclude, the thesis provides an outlook on the future developments in the field of nonlinear plasmonic research with regards to the development of highly efficient nonlinear metasurfaces through optimization of the Lorentz contributions. An insight into the recent developments in nanofabrication capabilities, design methodologies, nano-characterization techniques, modern electromagnetic simulations is discussed as avenues for future research in nanophotonic and nanoplasmonic device design and development.



# Contents

Supervisory Committee	ii
Abstract	iii
Table of Contents	v
List of Tables	viii
List of Figures	ix
Acknowledgements	xvii
Dedication	xviii
Glossary	xix
<b>1 Preface</b>	<b>1</b>
1.1 Research Objectives . . . . .	2
1.2 Author Contributions . . . . .	2
1.3 Report Structure . . . . .	2
<b>2 Introduction and Background Study</b>	<b>4</b>
2.1 Light-Matter Interaction . . . . .	5
2.2 Photonics Using Metals (Plasmonics) . . . . .	6
2.3 Surface Plasmon Polaritons . . . . .	8

2.4	Localized Surface Plasmons . . . . .	13
2.5	Extraordinary Optical Transmission . . . . .	16
2.6	Metamaterials . . . . .	19
2.7	Second Harmonic Generation . . . . .	22
2.7.1	SHG in Non-Centrosymmetric Media . . . . .	25
2.7.2	The Theory of Surface and Bulk Contributions to SHG . . . . .	27
2.7.3	Interband Transitions . . . . .	29
2.7.4	SHG Relation to Two-Photon Absorption . . . . .	30
2.8	Transmission of Light Through Sub-wavelength Apertures (Waveguide Modes) . . . . .	30
2.9	Design Consideration . . . . .	37
2.9.1	Optimizing Gap Plasmons . . . . .	37
2.9.2	Thermal Effects of the Incident Laser Beam on Nanostructures . . . . .	39
<b>3</b>	<b>Theoretical Approach and Analytical Model</b>	<b>41</b>
3.1	Nonlinear Optics . . . . .	42
3.2	Hydrodynamic Theory . . . . .	45
3.3	Nonlinear Scattering Theory . . . . .	51
3.4	Force on Magnetic Dipole from Electric Dipole . . . . .	56
3.5	Angled Hydrodynamic SHG Theory . . . . .	57
3.6	SHG Conversion Efficiency . . . . .	59
<b>4</b>	<b>Simulation Model</b>	<b>61</b>
4.1	Finite Difference Time Domain Method . . . . .	62
4.2	Convergence, Stability, and Accuracy of the FDTD . . . . .	63
4.2.1	Sources of Error in an FDTD Simulation . . . . .	65
4.3	Lumerical FDTD Software . . . . .	66

4.3.1	Grid Size . . . . .	68
4.3.2	Boundary Conditions . . . . .	69
4.3.3	Sources . . . . .	70
4.4	Simulation Model . . . . .	72
<b>5</b>	<b>Nanofabrication and Experimental Details</b>	<b>75</b>
5.1	Nanofabrication . . . . .	76
5.2	Scanning Electron Microscopy . . . . .	78
5.3	Optical Transmission Setup . . . . .	81
<b>6</b>	<b>Results Evaluation, Analysis and Comparison</b>	<b>84</b>
6.1	Magnetic Lorentz for Nonlinear Generation . . . . .	85
6.1.1	SHG Experimental Results of T-shaped Apertures . . . . .	93
6.2	Angled Lorentz Contribution . . . . .	98
<b>7</b>	<b>Conclusion and Outlook</b>	<b>104</b>
<b>A</b>	<b>Publications</b>	<b>108</b>
<b>B</b>	<b>Matlab Script</b>	<b>110</b>
	<b>Bibliography</b>	<b>118</b>

# List of Tables

Table 5.1 FIB fabrication parameters. . . . .	78
---	----

# List of Figures

Figure 2.1	A sample schematic of the SP wave at the interface of metal and dielectric. A typical representation of an SPP wave indicating field decay in the transverse direction [12]. . . . .	9
Figure 2.2	A planar two-medium system under the illumination of an EM field $\vec{E}$ . . . . .	10
Figure 2.3	Dispersion relation of SPPs at the interface between a Drude metal with negligible collision frequency and air (gray curves) and silica (black curves) [13]. . . . .	12
Figure 2.4	Configurations of SPP coupling techniques. a) and b) Two configurations of SPP excitation by total internal coupling (prism couplings). The angle $\theta$ determines the SPP propagation constant ( $k_{spp}$ ). c) Surface imperfections such as holes, ridges, protrusions, slots, or grooves can excite SPPs due to the diffraction. d) Near field excitation such as scanning near field microscope, scanning tunneling microscope is possible to excite SPPs by generating evanescence waves from the apex of an extremely fine tip. e) Grating coupling. $\theta$ and $\Lambda$ denote the incident angle and the period of the grating [14]. . . . .	13
Figure 2.5	A spherical metallic nanoparticle of radius $a$ placed in a constant electric field of magnitude $\vec{E}_0$ . . . . .	15

Figure 2.6 Diffraction and typical transmission spectrum of visible light through a subwavelength hole in an infinitely thin perfect metal film. A schematic of Bethe's law [17]. . . . .	17
Figure 2.7 Material characterized by their electric permittivity ( $\epsilon$ ) and magnetic permeability ( $\mu$ ) parameters [36]. . . . .	20
Figure 2.8 a) Simplified concept of metamaterials b) Metasurfaces are the 2D equivalent of bulk metamaterials. c-d) Various wavelength functionalities of metasurfaces. . . . .	22
Figure 2.9 A concept of plasmonic nanoparticles irradiated via EM and displacement of their conduction electron cloud correspondingly [12]	25
Figure 2.10a) Comparison between fundamental transmission (+ markers) and produced SHG intensity (* markers) through a periodic array of circular holes, b) Comparison of SHG output for the disordered (+ markers) and periodic arrays of circular holes (solid line) [23]. . . . .	27

- Figure 2.11 Comparing two frequency doubling phenomenons: SHG and two-photon absorption (two-photon excited fluorescence). Upon radiation of intense light at the original frequency  $\omega_i$ , the polarization of the medium results in re-emitting light at the frequency  $2\omega_i$ . Unlike two-photon excited fluorescence, all of the incident radiation energy at frequency  $\omega_i$  is converted in the process of SHG to radiation at the SHG frequency  $2\omega_i$ . Whereas two-photon excited fluorescence involves real energy transition of electrons, SHG involves only virtual energy transition. Moreover, the response time of SHG is at the femtosecond level, about several orders of magnitude faster than the nanosecond response time of fluorescence [77]. . . . . 31
- Figure 2.12 A cylindrical waveguide with a radius  $r$  much smaller than the wavelength  $\lambda_i$  of the incident electromagnetic field milled in a metal film of thickness  $h$ . The exponentially decreasing tail represents the attenuation of the subwavelength regime [17]. . . . . 32
- Figure 2.13 Two types of propagation modes in slab waveguides. The grey arrow indicates the direction of wave propagation. The blue lines and red lines represent the electric field and magnetic field respectively [14]. . . . . 33
- Figure 2.14 A schematic of the rectangular waveguide in a metal. The effective dielectric constant of the lowest TE mode is derived by considering the TM mode of the slab [32]. . . . . 34

Figure 2.15	Calculated cutoff wavelength for modes in a rectangular hole with a long edge of 270 <i>nm</i> in silver. When the size of the hole is decreased, the cutoff wavelength increases. PEC cutoff wavelength of 540 <i>nm</i> and 1D (without SP-enhancement) cutoff wavelength of 630 <i>nm</i> are also shown for comparison [81]. . . .	36
Figure 2.16	Absorption and scattering cross-section (black) and resonant THG prediction based on nonlinear scattering theory (red) for different gap sizes. Note that the optimal THG is predicted to occur when the absorption and scattering cross sections are equal [86].	38
Figure 2.17	Examples of damaged structures caused by the high intense laser beam a) Closed loop (disconnected) apertures b) Connected structures [86] . . . . .	40
Figure 3.1	a) An illustration of the most common nonlinear processes. b) Nonlinear processes energy-level diagrams. The solid lines indicate the ground state while the dotted lines indicate virtual levels [65]. . . . .	46
Figure 3.2	Volume containing two sets of electric sources and their corresponding EM fields . . . . .	52
Figure 3.3	An illustration of nonlinear scattering theory. Depicted is a system of a nonlinear optical material and a detector. The source at the detector position radiates a field at the harmonic wavelength toward the structure [99]. . . . .	54
Figure 3.4	a) Schematic of SHG from a T-shaped aperture array. b) Simulated configuration for incident fundamental and second harmonic waves (the source at the detector position radiates a field at the harmonic wavelength toward the structure). . . . .	55



Figure 4.1 A schematic of Yee's unit cell . . . . .	63
Figure 4.2 A screenshot of platform of the Lumerical computation space. .	67
Figure 4.3 A screenshot of proposed designed structure in lumerical computational space. . . . .	68
Figure 4.4 A schematic of the simulated structure for off-normal incident along with the simulation elements. Shining the P-polarized electromagnetic field at angle $\theta$ on the structure. . . . .	74
Figure 5.1 Hitachi FB2100 FIB machine at the University of Victoria. . . .	77
Figure 5.2 Hitachi S-4800 FESEM machine at the University of Victoria. .	79
Figure 5.3 A sample SEM image of the fabricated structures. . . . .	80
Figure 5.4 LSM 880 Zeiss machine used for optical measurements . . . . .	81
Figure 5.5 a) Simplified schematic of experimental setup. b) Blue filter spectrum . . . . .	82
Figure 6.1 Field and boundary conditions in a) PEC and b) PMC. $\perp$ and $\parallel$ are denoting the vertical and parallel components of the fields in the wall. . . . .	86
Figure 6.2 Comparison of the second harmonic conversion efficiency with and without Lorentz force contributions for the U-shaped SRR. Schematic of the SRR configuration is depicted with its dimensions based on Ref. [98]. . . . .	87
Figure 6.3 The past work results for comparison of the second harmonic conversion efficiency with and without Lorentz force contributions for the U-shaped SRR [98]. . . . .	88

Figure 6.4 Schematic of the proposed T-shaped structure and its dimensions. L shows the length of apertures, W width and G, the separation gap between two horizontal and vertical apertures. . . . .	89
Figure 6.5 Transmittance and reflectance spectrum of the designed structure showing resonance at 850 nm (L=240 nm, W=50 nm and G=50 nm) . . . . .	90
Figure 6.6 a) Top view schematic of T-shaped structure (gold on glass). Simulated field intensity for b) the $y$ component of $\vec{E}$ , c) the $z$ component of $\vec{E}$ , d) the $y$ component of $\vec{H}$ and e) the $z$ component of $\vec{H}$ . f) The Lorentz magnetic force contribution to the nonlinear source current proportional to $\vec{E} \times \vec{H}$ . . . . .	91
Figure 6.7 Lorentz magnetic force dominates SHG at the resonance of T-shaped aperture (same dimensions as described previously). . . . .	92
Figure 6.8 Incident EM field at 45° polarization results in horizontal polarized generated Lorentz magnetic force field. . . . .	93
Figure 6.9 Color map of calculated SHG intensity for different aperture length and incident polarizations, for a) total SHG, results from equation 3.19b, and b) considering only the Lorentz magnetic contribution to the SHG. . . . .	94
Figure 6.10 Simulation of the SHG signal expected from the surface contribution. . . . .	95
Figure 6.11 DC current density map for a) 45° and b) 135° incident beam polarization. . . . .	96

Figure 6.12a) T-shaped apertures of different sizes and orientations. b) Scanning electron image of fabricated apertures on a gold film. c) SHG measured in transmission mode shows the highest response for 45° aperture, indicating that the Lorentz force is the prominent contribution. d) A 45° analyzer further confirms the dominant role of the Lorentz force in SHG. . . . .	97
Figure 6.13 Captured images of the fabricated structures at different polarizations showing detected SHG signal as white spots. . . . .	98
Figure 6.14a) Captured images of the fabricated structures at different detection wavelengths varied from 400 <i>nm</i> to 450 <i>nm</i> representing detected SHG signal as white spots. Showing a significant high intensity at second harmonic wavelength ( $\sim 425$ <i>nm</i> ). b) The spectrum of detected signal for the same wavelength range. . .	99
Figure 6.15 SEM image of disordered array of circular apertures along with a plot of fundamental transmission (dashed linestyle) and SH signal (solid linestyle) as a function of incidence angle of the past work. The apertures are roughly 235 <i>nm</i> by 241 <i>nm</i> in size. Both curves are normalized to their maximum values [63]. . . .	100
Figure 6.16 Calculated filed intensity distribution of the 260 <i>nm</i> diameter aperture in 100 <i>nm</i> thick gold film under normal and two different angles of incident illumination, at 800 <i>nm</i> of the past work [63].	101
Figure 6.17 The FDTD simulation of the transmittance spectrum of the fundamental beam through the circular unit cell as a function of incidence angle, along with a digitized plot of the past experimental result of the same structure in Ref. [63]. Both curves are normalized to their maximum values. . . . .	102

Figure 6.18 SHG calculation based on NLS theory as a function of incident angle for Lorentz, the sum of two Coulomb and convective terms, and  $|\sin \theta \times \cos \theta|^2$ ; along with the digitized plot of the corresponding experimental SHG results in Ref [63]. The inset shows the curves plotted for small angles. The curves are normalized to their maximum value of total SHG. . . . . 103

## ACKNOWLEDGEMENTS

*If we knew what we were doing, it would not be called research*

Albert Einstein

I would like to begin by expressing my gratitude to my supervisor Dr. Reuven Gordon for his contentious guidance and support throughout my program of study.

I was lucky to be surrounded by a great group of friends and excellent members of the Nanoplasmonics Research Lab and would like to thank them all for their support and help. Specially Adarsh L. Ravindranath, Ryan Peck, and Noa Hacoheh for their time editing my thesis.

Finally, I would like to thank my parents for their unending love and support in every stage of my life.

## DEDICATION

...to future me who will be a better me and to remember me...

## GLOSSARY

### Common Abbreviations

Abbreviations	Meaning
ABC	absorbing boundary condition
AMF	advanced microscopy facility
DFG	difference frequency generation
EM	electromagnetic
EOT	extraordinary optical transmission
FDTD	finite difference time domain
FIB	focused ion beam
fcc	face-centered cubic
FWM	four wave mixing
IR	infrared
LSP	localized surface plasmon
LSPR	localized surface plasmon resonance
LSM	laser scanning microscope
NA	numerical aperture
NLS	nonlinear scattering
NLO	nonlinear optics
OR	optical rectification
PEC	perfect electric conductor
PMC	perfect magnetic conductor
PBC	periodic boundary condition
PML	perfectly match layer
SEM	scanning electron microscope
SHG	second harmonic generation
SPP	surface plasmon polariton
SP	surface plasmon
SPR	surface plasmon resonant
SRR	split ring resonator
SFG	sum frequency generation
TE	transverse electric field
TFSF	total-field scattered-field
THG	third harmonic generation
TM	transverse magnetic field

## GLOSSARY

### Symbols

Symbols	Meaning
$\vec{E}$	electric field strength
$\vec{H}$	magnetic field strength
$\vec{v}$	charge velocity
$\vec{D}$	dielectric displacement
$\vec{P}$	polarization factor
$\vec{B}$	magnetic flux density
$\vec{p}$	electric dipole moment
$\vec{m}$	magnetic dipole moment
$\vec{J}$	current density
$\mu$	permeability
$\rho$	charge density
$\alpha$	polarizability
$\vec{K}$	wave vector
$\epsilon$	permittivity
$\omega$	angular frequency
$\lambda$	wavelength
$c$	light speed
$I$	transmission intensity
$T$	transmission coefficient
$n$	number of charge density
$e$	electron charge
$m$	electron mass
$\beta$	Thomas-Fermi theory constant
$\gamma$	electron collision rate
$\chi^{(1)}$	first-order nonlinear optical susceptibility
$\chi^{(2)}$	second-order nonlinear optical susceptibility
$\chi^{(3)}$	third-order nonlinear optical susceptibility
$P_{\text{SHG}}$	SHG conversion efficiency
$P_{\text{THG}}$	THG conversion efficiency



# Chapter 1

## Preface



The study of the light matter interaction at the nanoscale has evolved into a multidisciplinary field of nanophotonics with applications in physics, chemistry, applied science, and biology. Also, recent developments in fabrication capabilities have enabled us to design and develop exciting new devices.

Metallic nanostructures are the main focus of this work. These nanostructures have been investigated extensively in the past decade, the study of these structures is receiving considerable attention. Their background study, theoretical concepts, and applications will be discussed briefly within the scope of this thesis.

## **1.1 Research Objectives**

The main objective of this research project was to characterize the capability of golden subwavelength apertures in second harmonic nonlinear generation with the goals of optimization and achieving high power efficiencies. Subsequently, developing a simple but reliable theoretical approach aiming towards understanding both the linear and nonlinear responses. Lastly, we hope that the outcomes of this research can pave the way for more efficient and applicable nanophotonic and nanoplasmonic devices.

## **1.2 Author Contributions**

This thesis is based on research projects which have either been published or submitted to peer-reviewed scientific journals. The list of author publications is available in Appendix A.

## **1.3 Report Structure**

After this Preface chapter, this report is organized as follows:

**Chapter 2 "Introduction and Background Study"** gives a brief introduction and overview of the nonlinear plasmonic metasurfaces and their background principal features in nonlinear optics.

**Chapter 3 "Theoretical Approach and Analytical Model"** reviews the theory behind nonlinear plasmonic metasurfaces and our developed hydrodynamic description in prediction the linear and nonlinear optical responses.

**Chapter 4 "Simulation Mode"** provides an introduction to the simulation model hired in the FDTD calculation method and simulation details in Lumerical software.

**Chapter 5 "Nanofabrication and Experimental Details"** describes the nanofabrication method and related machine tools in the fabrication of the experimental samples along with this research.

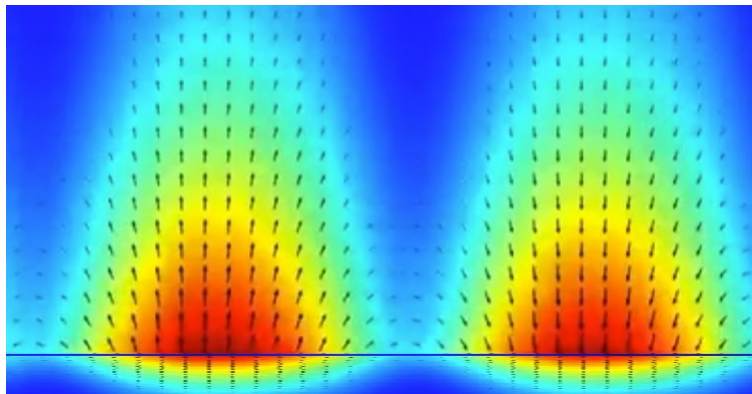
**Chapter 6 "Results Evaluation, Analysis and Comparison"** represents the simulation and experimental results of proposed metallic nanostructures.

**Chapter 7 "Conclusion and Outlook"** summarizes the work done and outlines proposed future directions and prospective research possibilities.

## Chapter 2

# Introduction and Background Study

This chapter provides a brief introduction and overview of the nonlinear plasmonic metasurfaces and their background in nonlinear optics, plasmonic effects, and harmonic generation. Lastly, it also covers some design considerations for optimizing metasurface structures.



## 2.1 Light-Matter Interaction

Achieving higher switching speed is one of the main goals of modern photonic devices. While semiconductor-based switching is fundamentally limited by their speed of carriers, the high speed nonlinear optical switching due to their no carrier transport limitation [1,2] gives nearly instantaneous interaction of light with materials. Hereby nonlinear optics was introduced as an alternate method that makes achieving higher possible speed by replacing electronic signals with optical signals [3].

On the other hand, the inherently weak interaction of light with matter results in a weak response that limits the achieved nonlinear power efficiency [2]. Fortunately, this efficiency limit can be overcome by increasing the light intensity and squeezing the incident light into a smaller material volume to achieve stronger nonlinear response when compared to unfocused light. One possibility is using regular lenses that can focus light onto a small region and increase the local field intensity. However, lenses are restricted to the diffraction limit [1]. Abbe's diffraction limit predicts that for conventional optics, light with wavelength  $\lambda$ , traveling in a medium with refractive index  $n$  can be focused just on spots with a diameter ( $d$ ) of approximately half of the wavelength of the incident light [4]:

$$d = \frac{\lambda}{2n \sin \theta} \approx \frac{\lambda}{2NA} \quad (2.1)$$

Plasmonics introduces another approach to increase the local field intensity. Plasmonics, as the interaction of light with metals, provides a simple approach squeezing light into subwavelength regions well below the diffraction limit.

## 2.2 Photonics Using Metals (Plasmonics)

Linear optics or the optics of weak light intensities describes the optical properties like scattering, reflection, or refraction. Within the range of weak light intensities on a material system light cannot interact with light and thus light cannot control light.

When the intensity of the incident light increases, the response of the medium is no longer linear. The refractive index, and consequently the speed of light in an optical medium does change with the light intensity. Light can alter its frequency as it passes through a nonlinear optical material, thus light can control light.

The study of the optical phenomena occurring when intense fields interact with material systems is known as nonlinear optics (NLO). NLO was born only one year after the invention of the laser in 1961 by Franken et al. [5].

Sufficiently intense optical fields excite a nonlinear polarization response from the medium, which in turn leads to re-radiation of new harmonic frequencies. The point to emphasize here is that, as well as the generation of new frequencies, nonlinear optics provide the ability to control light with light and so to transfer information directly from one beam to another without the need for electronic media.

Any materials can show nonlinear behavior; however, a huge electric field is usually required. In a special kind of material, metals, the combination of the obtained strong near-field intensity and their intrinsic nonlinearities readily result in efficient nonlinear optical processes. This has given rise to the new research field of nonlinearity, known as plasmonics.

Plasmonics forms a major part of the fascinating field of nanophotonics, which explores how the electromagnetic field can be confined over dimensions on the order of or smaller than the incident wavelength. It is based on interaction processes between electromagnetic radiation and conduction electrons in metals. This leads to enhanced optical near field and subsequently enhanced nonlinear effects with ultrafast response

times.

The enhanced local fields are naturally appealing for nonlinear optical processes, such as switching. There are also various other advantages of the effect of plasmonics on nonlinear optics; for instance, the processing of optical signals at ultrafast speed and enhancement of optical linear and nonlinear processes by producing a strong electromagnetic field. Research in plasmonics demonstrates how a distinct and often unexpected behavior can occur if discontinuities or sub-wavelength structure is imposed.

The plasmonic structures come in two distinct varieties: resonant and nonresonant structures.

In resonant structures, the time-varying electric field associated with the light waves applies a force on the gas of negatively charged electrons inside a metal and drives them into a collective oscillation, known as a surface plasmon (SP). At specific optical frequencies, this oscillation is resonantly driven to produce a very strong charge displacement and associated field concentration.

Plasmon resonance occurs at a frequency where the energy inside the metal and surrounding dielectric is equal [6]. Spherical nanoparticles, for instance, exhibit a dipolar plasmonic resonance at the wavelength where  $\epsilon_m = -2\epsilon_d$  ( here  $\epsilon_m$  and  $\epsilon_d$  are the permittivities of the metal and dielectric, respectively).

Although quasi-static resonance frequencies are independent of particle size, metallic nanoparticles can be made resonant over a wide range of frequencies by changing the type of metals, particle shape, or dielectric environment [7].

Nonresonant structures and their nonlinear effects can also be used to further enhance light concentration within the plasmonics area. For instance, in a study, strong subwavelength light localization in retardation based resonators was achieved by introducing a small gap in the metal structure (known as a feed gap) [8, 9]. In

other words, plasmonic tapers, such as metal cones or wedges, were used to provide broadband, nonresonant enhancements [10, 11]. Such structures support SP waves. As the light concentrators, they can substantially boost the field intensity within the region of interest.

The basic idea behind nonlinear plasmonics is to use the enhanced electric field associated with plasmon resonances to increase the strength of nonlinear optical effects. Thereby plasmonic structures have been used to enhance the efficiency of various nonlinear optical processes.

The two main ingredients of plasmonics, surface plasmon polaritons (SPPs), and localized surface plasmons (LSPs) have been clearly described for more than a century. The incident light can couple to the electron oscillations in the form of SPPs or LSPs, depending on the nanostructure's geometry. Both SPPs and LSPs are electromagnetic fields localized at the surface of the metal; both of which show significant field enhancement in comparison to the excitation field.

## 2.3 Surface Plasmon Polaritons

When the dimension of a photonic element approaches the incident light wavelength, due to the diffraction phenomena, there will be a huge issue with the confinement of the propagating light. However, when it comes to dimensions less than incident wavelength, SPs provide the possibility of localization and the guiding of light in subwavelength structures.

An SPP is a specific type of two-dimensional electromagnetic surface wave which is propagating and confined at the planar interface between a conductor and a dielectric. The energy of the wave is shared between the electron charge density (plasmon) of the metal and the electromagnetic field. These electromagnetic surface waves arise



via the coupling of the electromagnetic field to oscillations of the conductor's electron plasma. The most interesting feature of an SPP is that the electromagnetic field has components both perpendicular and parallel to the metal surface but the field is maximum at the interface of the metal and dielectric. SPs are bound to the metallic surface with an exponentially decaying field along the transverse direction in both neighboring media.

Figure 2.1 shows a sample SP wave at the interface of a metal and a dielectric.

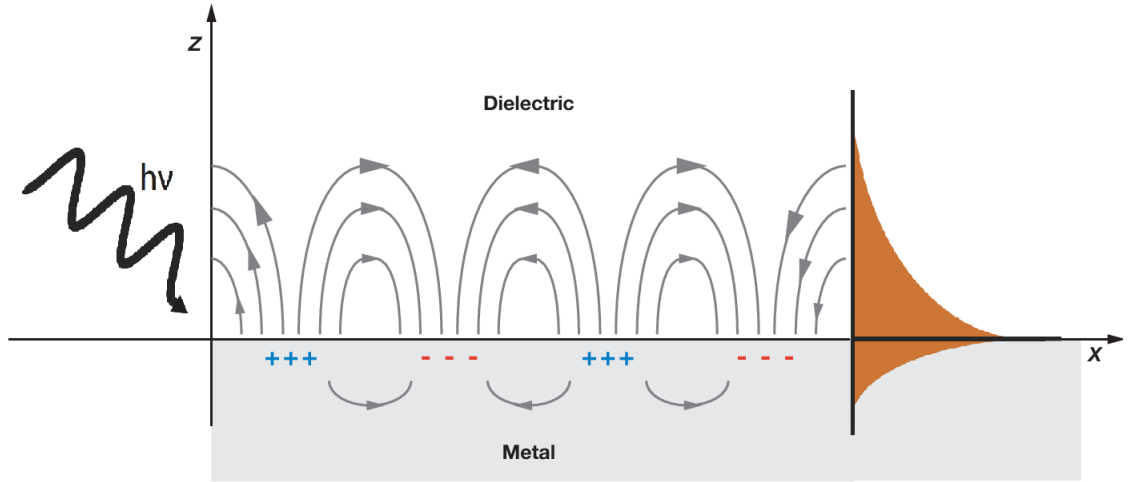


Figure 2.1: A sample schematic of the SP wave at the interface of metal and dielectric. A typical representation of an SPP wave indicating field decay in the transverse direction [12].

The bound and non-radiative character of SPs prevents power from propagating away from the surface, also providing the possibility of localization and guiding of light in subwavelength metallic structures.

An attractive aspect of SPPs is that they concentrate and channel light using subwavelength structures. By designing and tailoring the geometry of metallic nanostructures, and consequently their surface plasmon resonant (SPR) properties, these structures have been exploited for a variety of applications in the field of nanophotonics and plasmonics such as photonic integrated circuits, nonlinear optics, and

chemical/biological sensors.

In order to investigate the physical properties of SPPs, let us consider a planar two-medium system under the illumination of an EM field  $\vec{E}$  (Figure 2.2). By applying Maxwell's equations and the necessary boundary conditions to the flat interface of two media, one can derive the Helmholtz wave equation [13]:

$$\nabla^2 \vec{E} + k_0^2 \epsilon \vec{E} = 0 \quad (2.2)$$

where  $k_0 = \frac{2\pi}{\lambda_0}$  is the free space wave vector and  $\lambda_0$  is the vacuum wavelength.

Equation 2.2 gives two sets of self-consistent solutions with different polarization properties of the propagating waves.

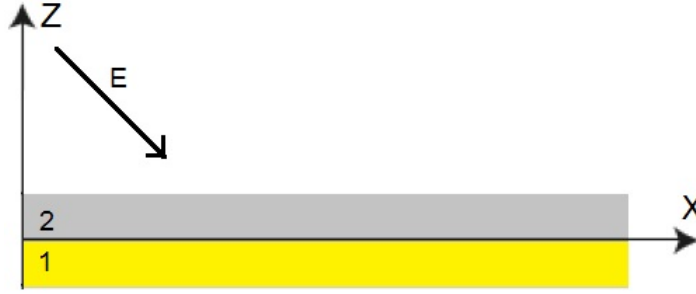


Figure 2.2: A planar two-medium system under the illumination of an EM field  $\vec{E}$

For the transverse magnetic field (TM or P) where there is no magnetic field component in the propagation direction, the solution shows that the surface waves exist only at interfaces between materials with opposite signs of the real part of their dielectric permittivities, i.e. between a conductor and an insulator. The dispersion relation for the structure and the corresponding field profile is written as [13]:

$$k_x^{sp} = k_0 \sqrt{\frac{\epsilon_m \epsilon_d}{\epsilon_m + \epsilon_d}} \quad (2.3)$$

where  $\epsilon_m$  and  $\epsilon_d$  are the dielectric constants of metal and dielectric respectively (represent the two media above).

It can be seen from equation 2.3 that the propagation constant  $k_x^{sp}$  tends to infinity as  $\epsilon_m$  approached  $\epsilon_d$  in case of negligible damping. This results in a very large imaginary transverse wave vectors and consequently, results in the wave to be confined to the surface, decaying exponentially on both sides of the interface surface (along  $z$ ) and a propagation wave at the interface (along  $x$ ).

Next, using a Drude model for the dielectric constant of metal results in the frequency of the SPPs, where it approaches the characteristic surface plasmon frequency [13]:

$$\omega_{sp} = \frac{\omega_p}{\sqrt{1 + \epsilon_d}} \quad (2.4)$$

where  $\omega_p$  is the bulk plasmon frequency of the metal.

The Drude model also describes the permittivity of a metal [13]

$$\epsilon_m(\omega) = 1 - \frac{\omega_p^2}{\omega(\omega + i\gamma_d)} \quad (2.5)$$

where  $\omega$  is the applied frequency,  $\gamma_d$  is the damping factor. The imaginary part of the permittivity is responsible for losses and is preferred to be minimized.

The bulk plasma frequency  $\omega_p$  can be recognized as the natural frequency of free oscillation of the electron sea. If the thermal motion of the electrons is ignored, it is possible to show that the charge density oscillates at the plasma frequency. The plasma frequency for metal with the number of charge density  $n$  can be expressed as:

$$\omega_p = \sqrt{\frac{ne^2}{\epsilon_m m_e}} \quad (2.6)$$

where  $e$  and  $m_e$  are the electron charge and mass respectively.

The dispersion relation in equation 2.3 is shown in Figure 2.3 for the interface between a Drude metal with negligible collision frequency, air, and silica for compar-

ison.

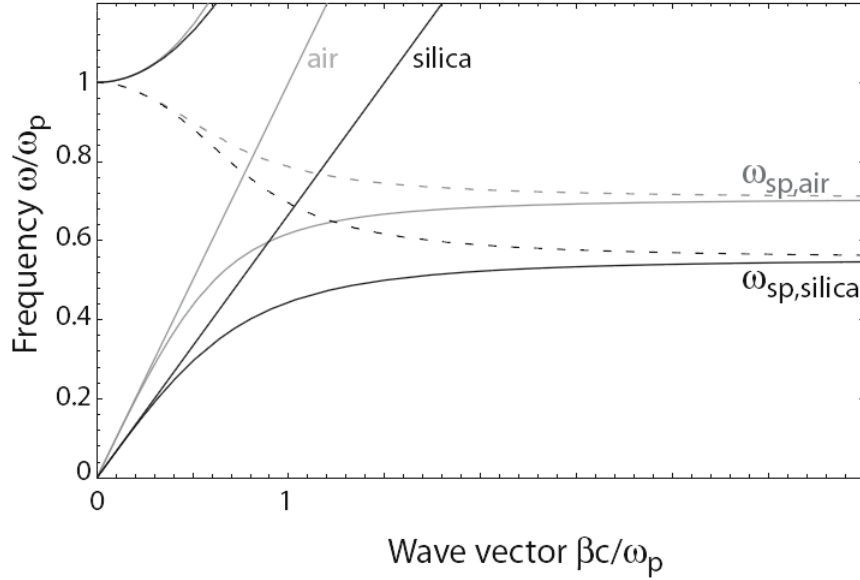


Figure 2.3: Dispersion relation of SPPs at the interface between a Drude metal with negligible collision frequency and air (gray curves) and silica (black curves) [13].

Solving equation 2.2 in case of the transverse electric field (TE or S) where there is no electric field component in the propagation direction shows that interface wave propagation has no propagation mode. Therefore it can be concluded that an SPP is only a TM wave mode.

In order to excite SPPs with photons, the wave vector of the SPPs has to match the wave vector of the photons. In other words, SPPs cannot be excited directly with photons incident from the dielectric. Several techniques have been devised for this purpose including total internal reflection coupling and grating coupling to account for the missing momentum.

Total internal reflection techniques are performed by propagating the incident light through a higher-index dielectric medium, usually in the form of a prism. The grating techniques use diffraction effects, for example, a periodic structure or from features on a rough surface to compensate for the missing momentum.

A schematic of these two processes along with some other approaches can be seen in Figure 2.4.

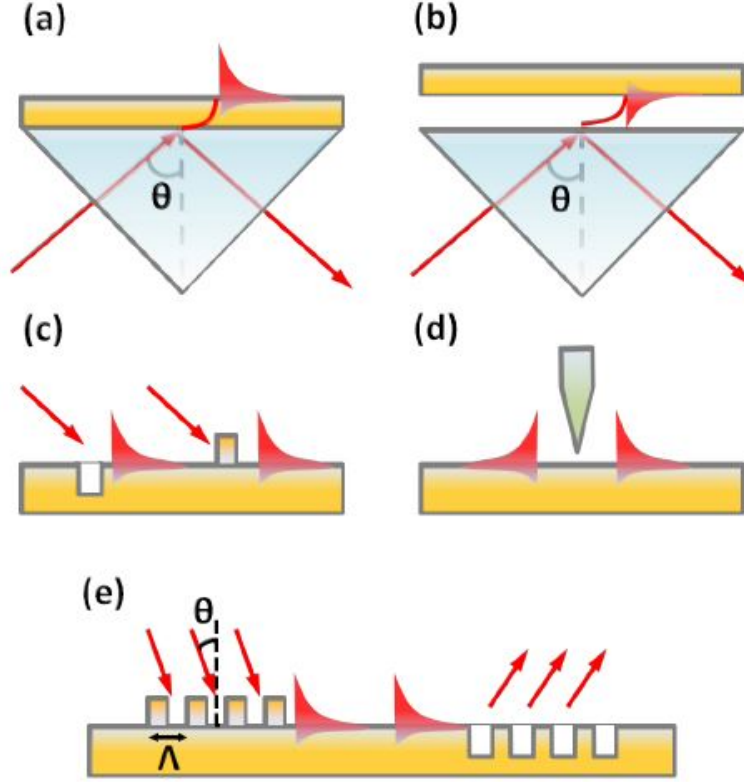


Figure 2.4: Configurations of SPP coupling techniques. a) and b) Two configurations of SPP excitation by total internal coupling (prism couplings). The angle  $\theta$  determines the SPP propagation constant ( $k_{spp}$ ). c) Surface imperfections such as holes, ridges, protrusions, slots, or grooves can excite SPPs due to the diffraction. d) Near field excitation such as scanning near field microscope, scanning tunneling microscope is possible to excite SPPs by generating evanescence waves from the apex of an extremely fine tip. e) Grating coupling.  $\theta$  and  $\Lambda$  denote the incident angle and the period of the grating [14].

## 2.4 Localized Surface Plasmons

Unlike propagating SPs that can travel along with the metal-dielectric interface and exist for a wide range of the frequency spectrum, LSPs are confined in a subwavelength

region, and their resonance is associated with the bound electron plasma inside the aperture or nanoparticle. They are very sensitive to the shape and the refractive index of the surrounding media.

Light through LSP can locally be coupled to the SPs inside an aperture, around a defect on the surface of the metal or in a metallic nanoparticle.

The LSP modes arise naturally from the scattering problem of a small, sub-wavelength conductive nanoparticle in an oscillating EM field. The curved surface of the particle takes an effective restoring force on the driven electrons so that resonance can arise, leading to field amplification both inside and in the near-field zone outside the particle. The resonance happens at a specific frequency, known as localized surface plasmon resonance (LSPR).

The LSPR of metal nanoparticles leads to the coloration of systems containing these nanoparticles, for example in the staining of glass for windows or ornamental cups. The most famous and probably the oldest example of this is the Lycurgus Cup.

Another interesting consequence of the curved surface is that plasmon resonances can be excited by direct light illumination, in contrast to propagating SPPs, where the phase-matching techniques have to be employed.

Let us consider a spherical metallic nanoparticle with radius  $a$ , permittivity  $\epsilon_m$ , surrounded by a dielectric medium with permittivity  $\epsilon_d$  under the illumination of a constant electric field with magnitude  $E_0$  as shown in Figure 2.5.

In the electrostatic approximation the electric field inside ( $\vec{E}_{in}$ ) and outside ( $\vec{E}_{out}$ ) of the particle can be derived using the Laplace equation [13]:

$$\vec{E}_{in} = \frac{2\epsilon_d}{\epsilon_m + 2\epsilon_d} \vec{E}_0 \quad (2.7a)$$

$$\vec{E}_{out} = \vec{E}_0 + \frac{3\vec{n}(\vec{n} \cdot \vec{p}) - \vec{p}}{4\pi\epsilon_m\epsilon_d r^3} \quad (2.7b)$$

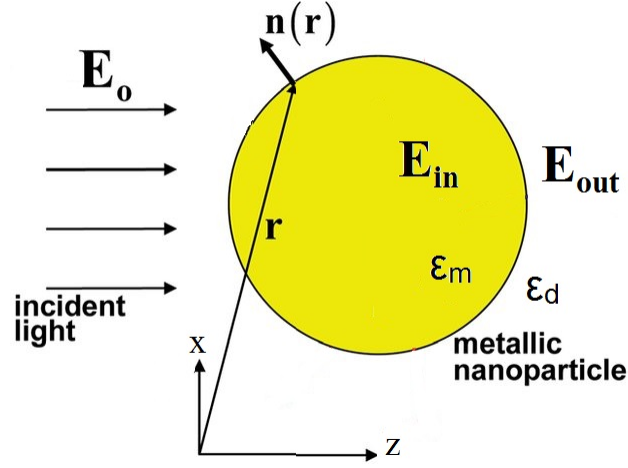


Figure 2.5: A spherical metallic nanoparticle of radius  $a$  placed in a constant electric field of magnitude  $\vec{E}_0$ .

where  $r$  is the radial distance of the observation point from the center of the particle,  $\vec{n}$  is a unit vector in the direction of observation point.  $\vec{p}$  in equation 2.7a is the dipole moment given by [13]:

$$\vec{p} = 4\pi\epsilon_0\epsilon_d a^3 \frac{\epsilon_m - \epsilon_d}{\epsilon_m + 2\epsilon_d} \vec{E}_0 \quad (2.8)$$

Polarizability  $\alpha$  as a property of matter is the ability to form instantaneous dipoles. If we introduce  $\alpha$  in an isotropic medium as the ratio of the induced dipole moment  $\vec{p}$  of an atom to the electric field  $\vec{E}_0$  that produces the dipole moment, it can be defined via  $\vec{p} = \epsilon_0\epsilon_d\alpha\vec{E}_0$ .  $\alpha$  can be expressed as [13]:

$$\alpha = 4\pi a^3 \frac{\epsilon_m - \epsilon_d}{\epsilon_m + 2\epsilon_d} \quad (2.9)$$

This polarizability gives infinite scattering so the nanoparticle acts as an electric dipole, if the Frölich condition is satisfied [13]:

$$Re[\epsilon_m(\omega)] = -2\epsilon_d \quad (2.10)$$

This resonant enhancement in turn enhances the field both inside and out of the particle. In fact, it is this field enhancement at the plasmon resonance on which several applications of optical devices rely.

For gold and silver nanoparticles, the resonance falls into the visible region of the electromagnetic spectrum [13]. A striking consequence of this is the bright colors exhibited by particles both in transmitted and reflected light, due to resonantly enhanced absorption and scattering.

## 2.5 Extraordinary Optical Transmission

Intuitively, the amount of transmitted light through an aperture in an opaque metal sheet should decrease with the hole area, but the light transmission through an aperture due to diffraction has been problematic to describe for years.

This process, which even in the simplest of geometries is very complex due to the wave nature of the light, can be described using various approximations developed in classical diffraction theory.

Let us define the transmission coefficient ( $T$ ) as the ratio of the total transmitted intensity to the total intensity impinging on the aperture area ( $I_0$ ) [13]:

$$T = \frac{\int I(\theta) d\Omega}{I_0} \quad (2.11)$$

For an aperture with radius  $r$  significantly larger than the wavelength of the impinging radiation ( $r \gg \lambda_0$ ) and normally-incident plane-wave, Huygens-Fresnel principle shows that  $T \approx 1$ .

The physics behind the regime of sub-wavelength apertures ( $r \ll \lambda_0$ ) was worked out more than 75 years ago by Bethe [15]. According to Bethe theory, the transmission efficiency of a single subwavelength aperture in an infinitely thin slab is given by [13,



16]:

$$T = \frac{64}{27\pi^2} (kr)^4 \approx \left(\frac{r}{\lambda_0}\right)^4 \quad (2.12)$$

Bethe's theory predicts that the transmission through a subwavelength hole drops as the fourth power of the hole-diameter, therefore, it is expected that almost no light would emerge from an array of subwavelength holes. Figure 2.6 demonstrates a schematic of Bethe's law.

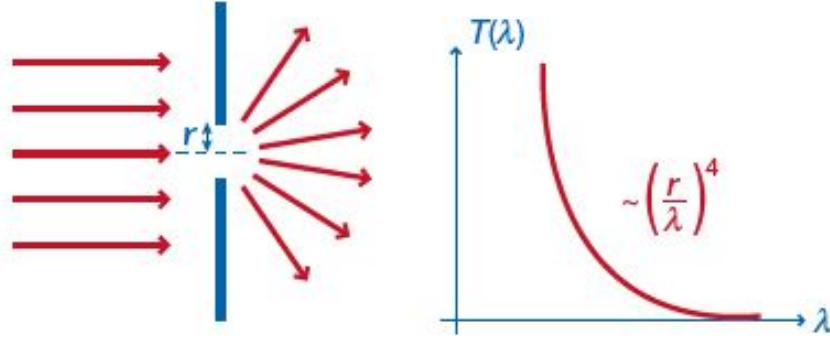


Figure 2.6: Diffraction and typical transmission spectrum of visible light through a subwavelength hole in an infinitely thin perfect metal film. A schematic of Bethe's law [17].

The classical electromagnetic theory supports these results as it is believed that apertures that are smaller than half of the wavelength of the transmitted light do not support any propagating modes [18]. Bethe's law remained unchallenged for 54 years until 1998 when Ebbesen and co-workers performed an experiment on the light transmission through square arrays of circular apertures in thin metallic films [19].

They found that the amount of transmitted light at certain wavelengths was much larger than predicted by the classical Bethe's aperture theory. They also demonstrated that there was more light transmitted than the actual amount impinging on the hole area. That means the material seemed much more transparent than it should be. This unexpected phenomenon was called extraordinary optical transmission (EOT).

The effect was observed for gold and silver films, but its magnitude decreased when other different metals were used [19].

Since introducing EOT a revolution has begun in the field of photonic devices research and many efforts have been made to improve functionalities of the regularly repeating periodic subwavelength apertures in metallic films in various applications [20–27].

The initial explanations of several authors attributed the EOT phenomenon to the excitation of surface plasmon resonances by grating coupling provided by the periodicity of the hole arrays leading to an enhanced light field on the top of the aperture. The efficient transmission happens by resonant excitation of SPPs on either or both sides of the metal films. After tunneling through the aperture, the energy in the SPP field is scattered into the far-field on the other side. The phase-matching condition imposed by the grating leads to a well-defined structuring of the transmission spectrum of the system, with peaks at the wavelengths where excitation of SPPs takes place. At these wavelengths,  $T > 1$  is possible. It means more light can travel through the aperture than incident on its area, in other words, the flux of photons per unit area emerging from the hole is larger than the incident flux per unit area. EOT is characterized by the appearance of a series of transmission peaks and dips in the transmission spectrum [28].

Although this interpretation has since been challenged [17], the evidence from several laboratories seems to consolidate the excitation of surface plasmons as the main contribution to the EOT effect [29, 30]. Moreover, the peaks of maximum transmission were related to the periodicity of the nanoholes.

Recent studies have also revealed that in observed EOT for single holes, contributions from localized waveguide modes inside the nano aperture (or LSPs effect), play a key role [31]. LSP modes enable the subwavelength apertures to act as a

propagating waveguide. For instance, a study shows that longitudinal and transverse LSP modes can be individually excited in rectangular holes by controlling the electric polarization of the incident light [32].

It should be noted that the past studies show that the field enhancement and subsequently transmittance enhancement depend on the hole geometry, the array periodicity, light wavelength, angle of incidence as well as material of the used film. These dependencies also have a large impact on the transmissivity, resonance wavelength, and polarization properties of the EOT [33, 34].

The effect of the hole shape on the transmission was further investigated from observations of arrays of nanoholes. An interesting result was that the cutoff wavelength for the transmission increases as the width of the rectangular holes is reduced [32].

One revolutionary emerging research field due to EOT was metamaterial and metasurface structures.

## 2.6 Metamaterials

The ability of deep subwavelength plasmonic structures to achieve strong light-matter interactions is forming the basis of an entirely new class of optical materials. When arranged into periodic arrays (or randomly distributed artificial structures), metallic structures can act as the functional units of an artificial medium known as metamaterials.

The term "metamaterial" first appeared in the literature in 2000 when Smith et al. published a seminal paper on a structured material with simultaneously negative permeability and permittivity at microwave frequencies [35].

The optical properties of the metamaterials are given by their geometrical shape of the blocks and their used materials, often a combination of metals and dielectrics.

Metamaterial optical behavior can be described by their effective material parameters such as their electric permittivity and magnetic permeability. Metamaterials fall in the group III of materials in Figure 2.7.

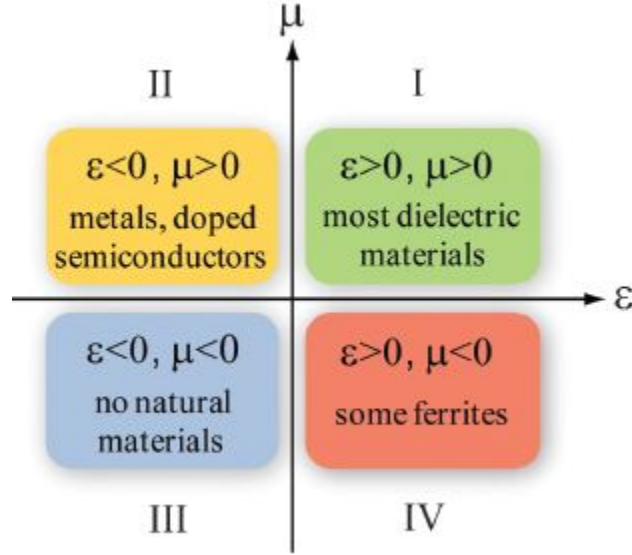


Figure 2.7: Material characterized by their electric permittivity ( $\epsilon$ ) and magnetic permeability ( $\mu$ ) parameters [36].

The word "Meta" is taken from Greek whose meaning is "beyond". By properly engineering the underlying building blocks, metamaterials are designed to have exotic optical properties beyond the naturally occurring materials such as prominent magnetic response, negative index of refraction, the giant chiral effect, and so on [37, 38].

These optical properties can be achieved by a single or multi-layered metallic nanostructure that is fabricated on the surface of a standard metal film [39, 40].

The high loss and strong dispersion associated with the resonant responses and the use of metallic structures, as well as the difficulty in fabricating the micro and nanoscale 3D structures, have hindered practical applications of metamaterials. This can mostly be attributed to absorptive losses inherent in plasmonic metals at optical frequencies, and to the challenges in fabricating complex 3D geometries at the nanoscale.

However, planar metamaterials with subwavelength thickness, known as metasurfaces, consisting of single-layer or few-layer stacks of planar structures, can be readily fabricated using lithography and nano-printing methods. Aperture-based metasurfaces due to their ability to remove heat from the surface and localize light within a subwavelength region are considered as good candidates for nonlinear generation.

Metasurfaces, the two-dimensional (2D) equivalent of bulk metamaterials, could be structured or non-structured with subwavelength patterns in planar dimensions [41]. They are the materials that extract their properties from their structure rather than the material of which they are composed of.

Metasurfaces are widely utilized to enhance the nonlinear optical response of a metal thin film. The metallic metasurfaces are used for applications including optical switching [42], wavelength conversion [43], near-field imaging [44], subwavelength lithography [45,46], spectroscopy [47,48], phase or polarization control [49–52], nonlinear harmonic generations [53, 54], changing angle, beam-steering or beam-shaping [55–57] and so on.

Figure 2.8 gives a simple concept of metamaterials and metasurfaces and some of their applications.

In the field of nanoplasmonics still there are limiting factors and challenges regarding the use of metasurface structures, such as material damage (for 100 nm gold on a fused silica substrate damage occurs at around  $10 \text{ mW}/\mu\text{m}^2$  and close to  $1 \text{ mW}/\mu\text{m}^2$  for nanostructures with tiny gaps) and also the saturation of the nonlinear response.

Among metallic metasurfaces, gold nanostructures have been used as promising metasurface structures due to their high plasmonic effects and optical advantages. Gold makes a suitable candidate for a nonlinear generation due to its relatively low loss along with its large nonlinear susceptibility. Engineering gold plasmonic structures allow the nonlinear responses to be significantly enhanced [58]. Throughout our

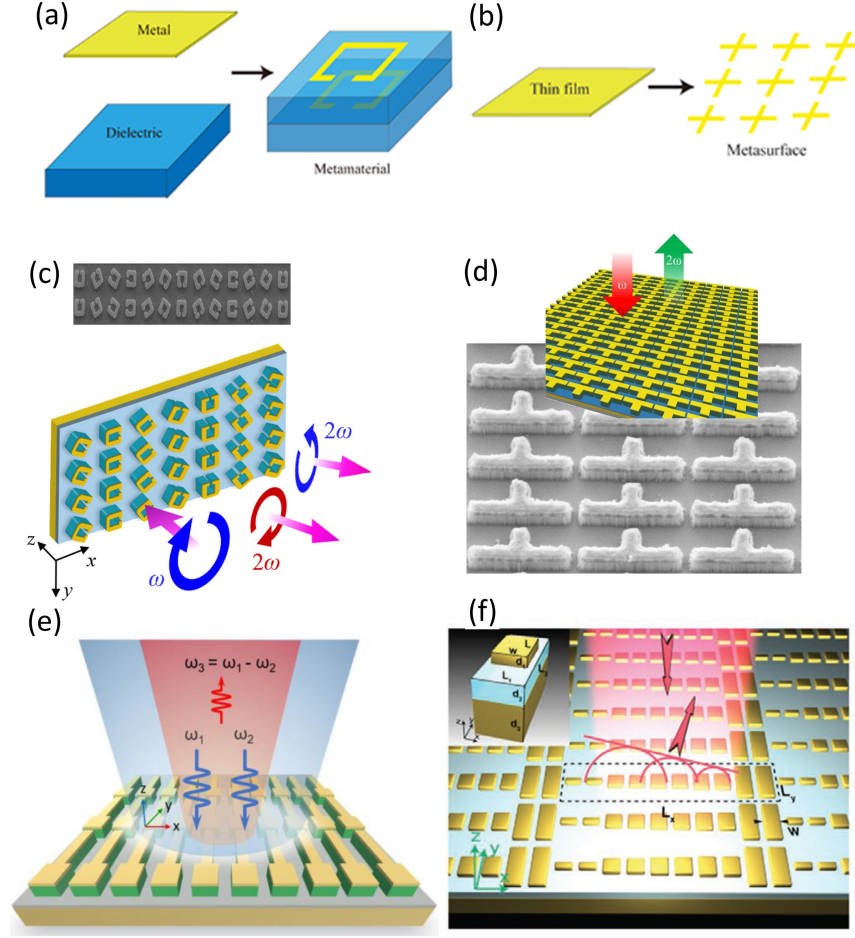


Figure 2.8: a) Simplified concept of metamaterials b) Metasurfaces are the 2D equivalent of bulk metamaterials. c-d) Various wavelength functionalities of metasurfaces.

research, we specifically have focused on gold nonlinear plasmonic metasurfaces.

## 2.7 Second Harmonic Generation

For an applied EM field at frequency  $\omega$ , second-order nonlinear polarization will lead to the generation of irradiation at the second harmonic frequency  $2\omega$ , known as second harmonic generation (SHG).

By definition, SHG is a second-order nonlinear optical process, where two incident photons are combined and converted into a single scattered photon with twice the

fundamental frequency.

The phenomenon of optical SHG was first observed in 1961 by Franken et al. when measuring the emergence of 347.1 *nm* laser light when a ruby laser of 694.2 *nm* was passed through a quartz crystal [5].

Crystal materials lacking inversion symmetry can exhibit  $\chi^{(2)}$  nonlinearity. The crystals upon the incident of a pump wave in the form of a laser beam can generate SHG in the form of a beam propagating in a similar direction. Some of the well-known crystal materials for SHG are : *b*- $BaB_2O_4$  (BBO), lithium niobate ( $LiNbO_3$ ), potassium titanyl phosphate (KTP =  $KTiOPO_4$ ), and lithium triborate (LBO =  $LiB_3O_5$ ).

SHG is a widely known nonlinear effect and is regularly used to upconvert infrared to visible and ultraviolet radiation. For instance, green light (wavelength 532 *nm*) can be generated by frequency-doubling the output of neodymium or ytterbium-based laser (1064 *nm*). Green laser pointers are also usually based on this approach.

Apart from lasers applications, harmonic generations like SHG are used in non-linear microscopy in biological and medical science, ultra-short pulse measurements, and are also widely used in bioimaging.

Third harmonic generation (THG) as another well-known nonlinear harmonic generation is analogous to SHG. In this process, three photons combine to produce one photon with triple of the initial frequency. THG is a much less efficient process compared to SHG and is typically observed in centrosymmetric systems where SHG is suppressed.

Another second-order process in which two photons annihilate simultaneously producing constant polarization is called optical rectification (OR). OR is widely used as a source of terahertz (THz) signal generations.

The physical mechanism behind the SHG frequency doubling process can be ex-

plained as like the fundamental incident wave  $\vec{E}_1$  at frequency  $\omega$  generates a nonlinear polarization wave  $\vec{P}_2$  due to the  $\chi^{(2)}$  nonlinearity. According to Maxwell's equations, this nonlinear polarization wave radiates an EM field  $\vec{E}_2$  at doubled frequency  $2\omega$ . The generated SH field propagates dominantly in the direction of the nonlinear polarization wave.

Since the input beam has a well-defined phase and amplitude at every point inside the crystal at a given time, the relative phase of the induced dipoles is fixed. To obtain a second harmonic output at the end of the crystal it is important that the induced dipoles radiate in phase. This process is referred to as phase-matching which ensures that the contributions from all positions in the crystal add up constructively.

In a similar way to crystals, in metallic media, when an electric field is applied to a metallic particle or structure, the conduction electrons are displaced from their equilibrium position with respect to the core ions, causing a polarization of the particle and a depolarizing field that acts as a restoring force (Figure 2.9). In other words, the fundamental (pump) wave generates a nonlinear polarization wave that oscillates with twice the fundamental frequency. Again, Maxwell's equations lead to a nonlinear polarization wave that radiates an electromagnetic field with doubled frequency.

The intensity of the produced second harmonic signal grows with the square of the pump intensity and also is proportional to the square of the second-order susceptibility;  $I(2\omega) = |\chi^{(2)}|^2 I^2(\omega)$ .

The signal obtained from SHG is extremely weak due to small values of nonlinear susceptibilities; therefore, to observe SHG, the incident light must be of very high intensity like the lights from ultra-short pulsed lasers. The limited signal strength could thus limit the applicability of these techniques to specialized situations only.

Enhancements of the signals, however, are possible through the excitation of SPs to yield surface-enhanced second harmonic generation. These enhancements make



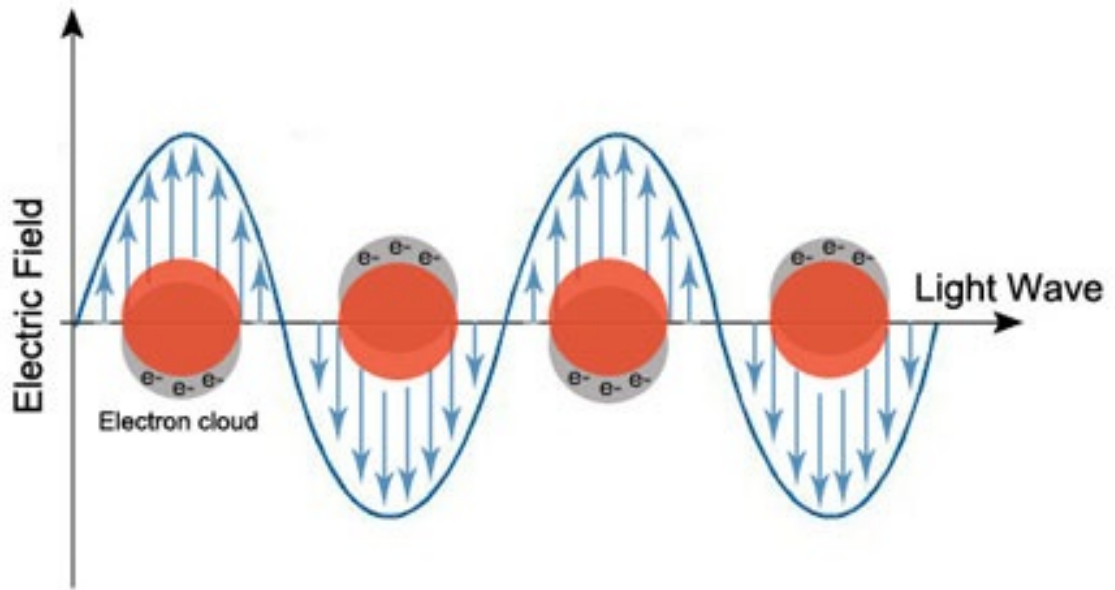


Figure 2.9: A concept of plasmonic nanoparticles irradiated via EM and displacement of their conduction electron cloud correspondingly [12]

new potential uses of these techniques possible.

### 2.7.1 SHG in Non-Centrosymmetric Media

Within the dipole approximation, SHG can only be seen in systems lacking inversion symmetry. Therefore SHG is forbidden in any bulk materials that exhibit inversion symmetry, such as any face-centered cubic (fcc) crystals.

For frequencies lower than the plasma frequency, the electromagnetic radiation can penetrate only for a small depth (skin depth) of the order of the wavelength in the non-structured metallic films. Due to the fcc crystal structure of the most metals, bulk metals lack dipole sources for second harmonic production. Within the skin depth of the incident electromagnetic field, there are, however, Lorentz forces on free (and to some degree also bound) electrons, as well as interband transitions. Both of which lead to nonlinear bulk magnetic dipole polarization sources.

Further, beyond the electric dipole approximation, the spatial variation of the electromagnetic field can break the centrosymmetry. This introduces strong surface currents within a few Fermi wavelengths of the surface which produce electric quadrupole bulk terms.

Obviously, the centrosymmetry is locally broken at the metal surface because of the finite dimension of the atomic lattice. The structure property of a metal nanostructures also is commonly altered to achieve broken symmetry for greater SHG [59]. This broken symmetry gives rise to a dipolar surface nonlinearity (surface SHG).

The bulk (volume) and surface contributions may be excited by different polarizations [60], but it was generally recognized that it may not be possible to fully decompose surface and volume terms due to the presence of “bulk-like” surface contributions induced by the fast field variation at the metal interface [61].

The experimental challenge of separation of bulk (magnetic dipole and electric quadrupole origin) and surface (electric dipole origin) contributions was tackled by the introduction of the two-beam SHG configuration [62].

In addition to the use of non-centrosymmetric structures in the generation of SHG, subwavelength structures can be used to induce nonlinear enhancement where symmetry breaking is obtained with centrosymmetric apertures under off-normal incidence illumination [22, 59, 63]. In a study, SHG from circular hole arrays were found to depend on the angle of incidence [23]. For a periodic array of circular holes, the measured SHG signal peaked at incidence angles corresponding to maximum transmission of the fundamental beam [23, 63]. The study showed for small incidence angles ( $< 15^\circ$ ) the second harmonic signal is weak due to the inversion symmetry of the aperture (Figure 2.10 (a)). The study also showed that even though periodic arrays could exhibit greater fundamental beam transmission (more than five times), disordered arrays showed greater SHG especially at large incidence angles, as shown

in Figure 2.10 (b). This was attributed to large microscopic symmetry breaking and local resonances due to the evanescent penetration through the holes without the actual surface plasmon enhancement [23].

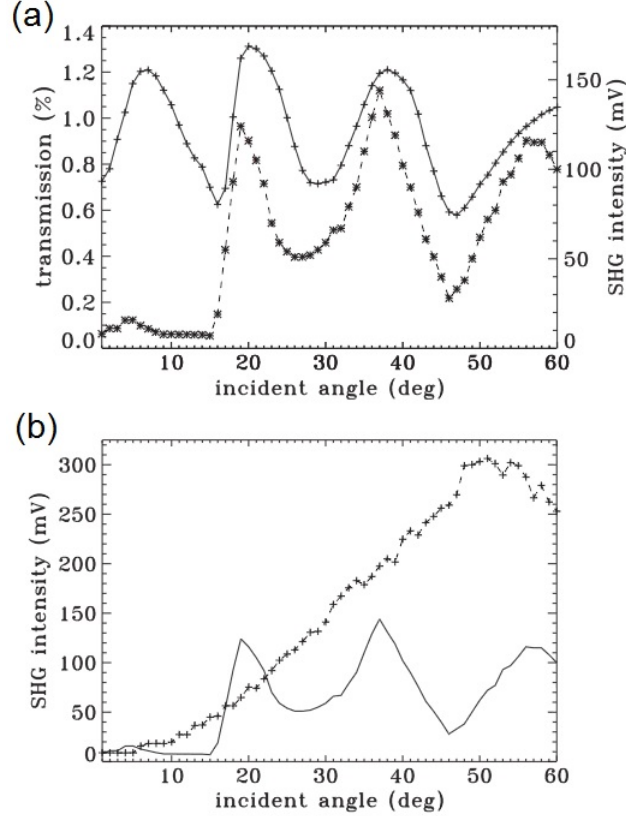


Figure 2.10: a) Comparison between fundamental transmission (+ markers) and produced SHG intensity (\* markers) through a periodic array of circular holes, b) Comparison of SHG output for the disordered (+ markers) and periodic arrays of circular holes (solid line) [23].

### 2.7.2 The Theory of Surface and Bulk Contributions to SHG

According to a model, studying the SHG in centrosymmetric media, developed by Heinz [64], the SHG nonlinear polarization consists of two components. First, a (local) dipole allowed surface nonlinear polarization,  $\vec{P}_s^{(2)}(2\omega, r)$ , defined within a surface layer several angstroms thin where the inversion symmetry property is broken.

Second, a (nonlocal) bulk nonlinear polarization,  $\vec{P}_b^{(2)}(2\omega, r)$ , which is generated inside the nonlinear optical medium by electric quadrupoles and magnetic dipoles.

The surface contribution to the nonlinear optical response of centrosymmetric media is described as [65]:

$$\vec{P}_s^{(2)}(2\omega, r) = \epsilon_0 \chi_s^{(2)} \vec{E}(\omega, r) \vec{E}(\omega, r) \delta(r - r_s) \quad (2.13)$$

where  $r_s$  defines the surface,  $\chi_s^{(2)}$  is the surface second-order susceptibility tensor, and the Dirac delta-function expresses the surface characteristic of the nonlinear polarization.

When the surface anisotropy is neglected, the second-order surface susceptibility  $\chi_s^{(2)}$  has only three nonvanishing and independent components,  $\chi_{\perp\perp\perp}^{(2)}$ ,  $\chi_{\perp\perp\parallel}^{(2)}$ , and  $\chi_{\parallel\parallel\perp}^{(2)} = \chi_{\parallel\perp\parallel}^{(2)}$ , where  $\perp$  and  $\parallel$  refer to the orthogonal and tangential components to the surface [66]. Therefore the surface nonlinear polarization can be cast as [65]:

$$\begin{aligned} \vec{P}_s^{(2)}(2\omega, r) = & \epsilon_0 [\chi_{\perp\perp\perp}^{(2)} \hat{n} \hat{n} \hat{n} + \chi_{\perp\parallel\parallel}^{(2)} (\hat{n} \hat{t}_1 \hat{t}_1 + \hat{n} \hat{t}_2 \hat{t}_2) + \\ & \chi_{\parallel\perp\parallel}^{(2)} (\hat{t}_1 \hat{n} \hat{t}_1 + \hat{t}_2 \hat{n} \hat{t}_2)] \vec{E}(\omega, r) \vec{E}(\omega, r) \end{aligned} \quad (2.14)$$

where  $\hat{n}$  is the outwardly pointing normal to the surface of the scatterer and  $\hat{t}_1$  and  $\hat{t}_2$  are the two orthonormal vectors defining the plane tangent to the surface.

Bulk contributions also can be expressed as [64]:

$$\begin{aligned} \vec{P}_b^{(2)}(2\omega, r) = & \gamma \nabla [\vec{E}(\omega, r) \cdot \vec{E}(\omega, r)] + \delta' [\vec{E}(\omega, r) \cdot \nabla] \vec{E}(\omega, r) + \\ & \beta [\nabla \cdot \vec{E}(\omega, r)] \vec{E}(\omega, r) + \zeta \vec{E}(\omega, r) \nabla \vec{E}(\omega, r) \end{aligned} \quad (2.15)$$

where  $\gamma, \delta', \beta$  and  $\zeta$  are material parameters due to electric quadrupoles and magnetic dipoles located in the bulk of the medium.

Most theoretical models predict that  $\chi_{\perp\perp\parallel}^{(2)} = 0$  [67, 68], this assumption is commonly made in studies of SHG from plasmonic structures. Although for plasmonic

metals, the  $\chi_{\perp\perp\perp}^{(2)}$  component is the largest component of the surface nonlinear susceptibility by at least one order of magnitude, which would be sufficient to describe most of the experimental results, both surface and bulk effects should be taken into account for an accurate description of the systems since both could be observed depending on the experimental conditions.

Previously, a study has enhanced the bulk effects by inhomogeneous local field in metal nanostructures, therefore the bulk SHG was used to model second harmonic generation from metamaterials [69]. In another study it was found that for plasmonic nanoparticles the surface contribution is always dominant, however, the bulk and surface SHG effects can become comparable for dielectric nanoparticles, and thus they both should be taken into account when analyzing nonlinear optical properties of all-dielectric nanostructures [70].

### 2.7.3 Interband Transitions

Besides bulk and surface contributions, there can be an interband contribution to the nonlinear response of gold that enhances this response [71]. Interband transitions is one of the mechanisms contributing to the nonlinear optical response of gold that involves the electronic transitions from the 5d band to the 6s-6p band [72, 73].

Others have investigated the wavelength dependence of the third harmonic generation for the gold plasmonic system to determine the role of the interband transitions in the nonlinear response of gold [74]. The THG was measured as a function of infrared (IR) fundamental wavelength for gold nanoparticles over a gold film. An order of magnitude enhancement in THG was found at  $\approx 2.5$  eV, which is away from plasmonic resonances, so it may be attributed directly to the ultrafast third-order susceptibility of gold enhanced by the interband transitions [74]. Other works also have surveyed the various responses of gold at different time scales [72].

Another work reported a strong wavelength dependence of the nonlinear response of gold for the fundamental wavelength at about 550 *nm*, attributed to the interband transitions between the 5d to 6s-6p bands [75].

Finally, a recent work investigate the nonlinearity of gold nanolayers and explores the their interband transition and hot electron contributions [76]. This can lead us to further investigation of the off-normal incident SHG and its contributions.

#### 2.7.4 SHG Relation to Two-Photon Absorption

Two-photon absorption (two-photon excited fluorescence) is where an atomic transition is made by the absorption of two-photons of frequencies  $\omega_1$  and  $\omega_2$ , the sum of which is resonant with the energy of the total atomic transition. This process is very similar to the generation of second harmonic light generation described here. When second harmonic light is generated, e.g. in a BBO crystal, two-photons at  $\omega$  are absorbed virtually, with the production of a photon at  $2\omega$ . The process is said to be parametric, as no net absorption of energy has taken place. The process of two-photon absorption in an atom is similar, except that one now replaces one or both of the virtual levels with real levels (energy eigenstates) of the atom. The process is then non-parametric. Figure 2.11 shows a schematic of comparing these two phenomenons.

## 2.8 Transmission of Light Through Sub-wavelength Apertures (Waveguide Modes)

An aperture in a subwavelength film is characterized by its depth and therefore has waveguide properties. The confined space of the aperture essentially modifies the dispersion relation of the transmitted electromagnetic field. The lateral dimensions

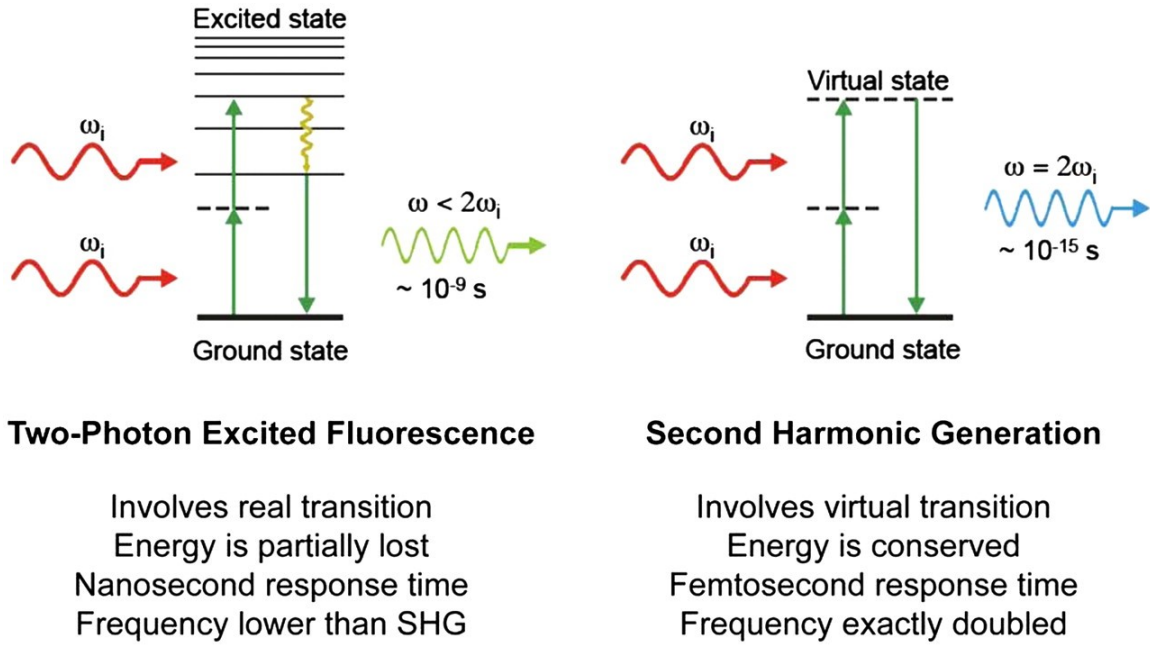


Figure 2.11: Comparing two frequency doubling phenomena: SHG and two-photon absorption (two-photon excited fluorescence). Upon radiation of intense light at the original frequency  $\omega_i$ , the polarization of the medium results in re-emitting light at the frequency  $2\omega_i$ . Unlike two-photon excited fluorescence, all of the incident radiation energy at frequency  $\omega_i$  is converted in the process of SHG to radiation at the SHG frequency  $2\omega_i$ . Whereas two-photon excited fluorescence involves real energy transition of electrons, SHG involves only virtual energy transition. Moreover, the response time of SHG is at the femtosecond level, about several orders of magnitude faster than the nanosecond response time of fluorescence [77].

of the waveguide define the wavelength at which light can no longer propagate through the aperture. This wavelength is known as the cutoff wavelength ( $\lambda_c$ ).

For an aperture the cut-off condition occurs when the wavelength of the light is more than twice the aperture length [78]. Below cut-off, when the incident wavelength  $\lambda_i > \lambda_c$ , Bethe showed that the transmission of light through an aperture rapidly decreases as the fourth power of the ratio of the aperture length to the optical wavelength [15]. This characterizes the non-propagating regime as shown in Figure 2.12.

There is a straightforward relationship between the cross-section of the waveguide

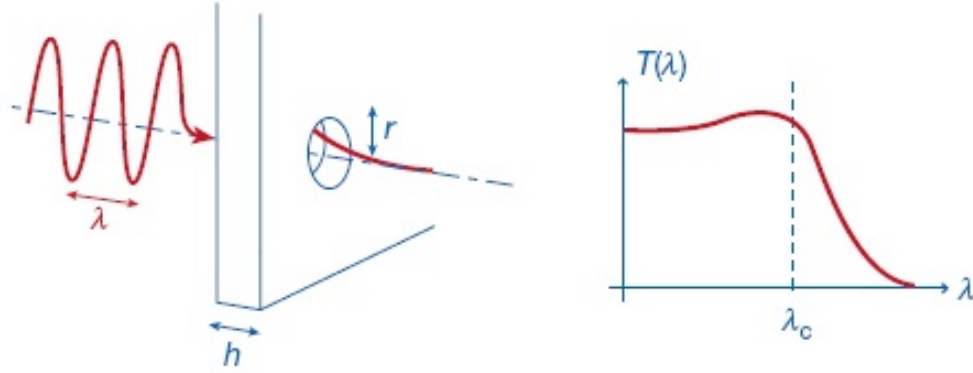


Figure 2.12: A cylindrical waveguide with a radius  $r$  much smaller than the wavelength  $\lambda_i$  of the incident electromagnetic field milled in a metal film of thickness  $h$ . The exponentially decreasing tail represents the attenuation of the subwavelength regime [17].

and  $\lambda_c$ . However, one should take into account that  $\lambda_c$  for an aperture in a real metal is increased by taking the skin-depth into account, reflecting the penetration of the electromagnetic field inside the walls of the metal waveguide.

It is possible to control and even to eliminate cutoff wavelengths even when the lateral dimensions are much smaller than  $\lambda_i$ , by playing with more complex geometries. While simple apertures are always characterized by the existence of cutoff wavelengths, an annular hole, for example, which resembles a coaxial cable, has no cutoff wavelength and is always propagating [17].

The polarization of the incident light is also an important parameter, and with non-cylindrical waveguides, the transmission can be made extremely polarization sensitive. In the case of a slit, for incident polarization parallel to the long axis, the transmission can be made subwavelength, as long as the short dimension of the rectangle is smaller than  $\lambda_i$ . However, for the perpendicular polarization, no matter how narrow the waveguide is, the light always propagates through it. This allows for many possibilities in the choice of geometry depending on the application.

In the case of a rectangular aperture, the TE and TM modes are considered



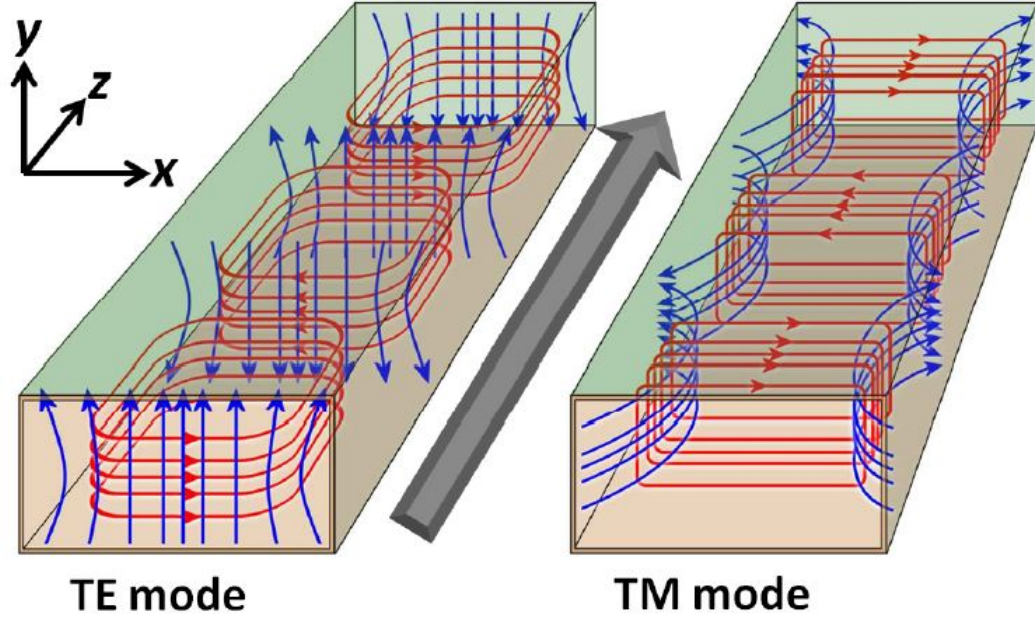


Figure 2.13: Two types of propagation modes in slab waveguides. The grey arrow indicates the direction of wave propagation. The blue lines and red lines represent the electric field and magnetic field respectively [14].

(Figure 2.13). Only the zero-order TE mode is required to estimate the resonance wavelength of the aperture. This resonance is close to the cut-off wavelength of the aperture [32, 79, 80].

Figure 2.14 shows a rectangular aperture of short edge  $w$  and long edge  $l$  in a metal, illuminated by a normally incident plane wave. The center of the hole is assumed to be air. The metal has relative permittivity  $\epsilon_m$ .

The propagation constant of the  $TE_{01}$  mode in a rectangular aperture perforated in PEC is represented by [32]:

$$k_{TE_{01}} = \pi \sqrt{\left(\frac{2}{\lambda}\right)^2 - \left(\frac{1}{l}\right)^2} \quad (2.16)$$

Therefore it can be conceded that the cut-off wavelength of PEC is [32]:

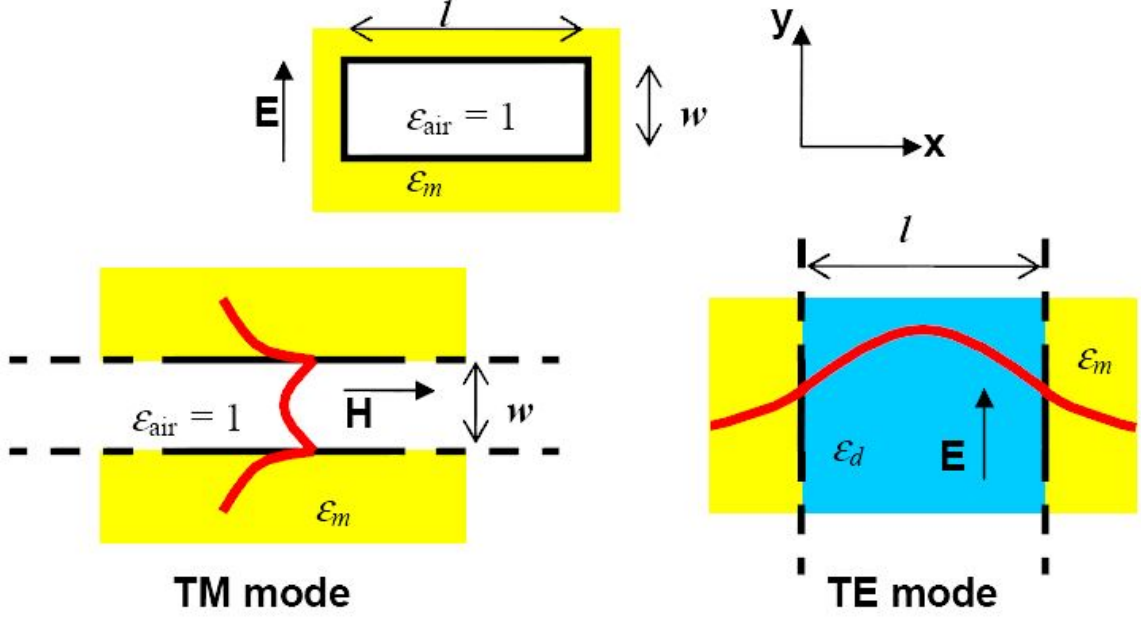


Figure 2.14: A schematic of the rectangular waveguide in a metal. The effective dielectric constant of the lowest TE mode is derived by considering the TM mode of the slab [32].

$$\lambda_c = 2l \quad (2.17)$$

In a previous work [32], the waveguide mode of a subwavelength rectangular hole in a real metal was analyzed by using the surface plasmon waveguide dispersion theory. For a single rectangular aperture, the resonance is influenced by both couplings between SP modes along the x-direction and penetration of the field into the metal along the y-direction (Figure 2.14).

To estimate the cut-off wavelength of the rectangular aperture in a real metal, Gordon et.al. calculated the TM mode between two parallel plates of a real metal propagating along the x-direction, derived from the TM mode characteristic equation breaking the 2D problem down into two 1D effective index problems [32]:

$$\tanh\left(\sqrt{k_{TM}^2 - k_o^2\epsilon_{air}}\frac{w}{2}\right) = \frac{-\epsilon_{air}}{\epsilon_m} \frac{\sqrt{k_{TM}^2 - k_o^2\epsilon_m}}{\sqrt{k_{TM}^2 - k_o^2\epsilon_{air}}} \quad (2.18)$$

where  $k_{TM}$  is the propagation constant of the TM mode of the aperture along the  $x$  direction.

This allows us to identify two separate contributions to the extended cut-off wavelength: penetration of the field into the metal along the  $x$ -direction, and coupling between SP modes along the  $y$ -direction.

The effective dielectric constant,  $\epsilon_d$  of the medium as the influence of the SP gap mode can also be presented as [32]:

$$\epsilon_d = \left(\frac{k_{TM}}{k_0}\right)^2 \quad (2.19)$$

where  $k_0 = \frac{2\pi}{\lambda}$  is the free-space wave-vector. The  $TE$  propagating mode, associated with the coupling of the SP waves on the opposite long edges of the aperture, is also represented by the TE mode characteristic equation [32]:

$$\tan\left(\sqrt{k_0^2\epsilon_d - k_{TE}^2}\frac{l}{2}\right) = \frac{\sqrt{k_{TE}^2 - k_0^2\epsilon_m}}{\sqrt{k_0^2 - k_{TE}^2}} \quad (2.20)$$

Where  $k_{TE}$  is the propagation constant of the TE mode of the aperture along the  $y$ -direction.

Consequently the cut-off wavelength of a real metal can be obtained as [32]:

$$\lambda_{\text{cut-off}} = \frac{\pi l \sqrt{\epsilon_d}}{\arctan\left(\sqrt{-\frac{\epsilon_m}{\epsilon_d}}\right)} \quad (2.21)$$

Figure 2.15 shows the calculated cutoff wavelength as a function of the short-edge width of the hole. When the size of the hole is decreased, the cutoff wavelength actually increases, which allows for longer wavelengths of light to propagate through

the hole.

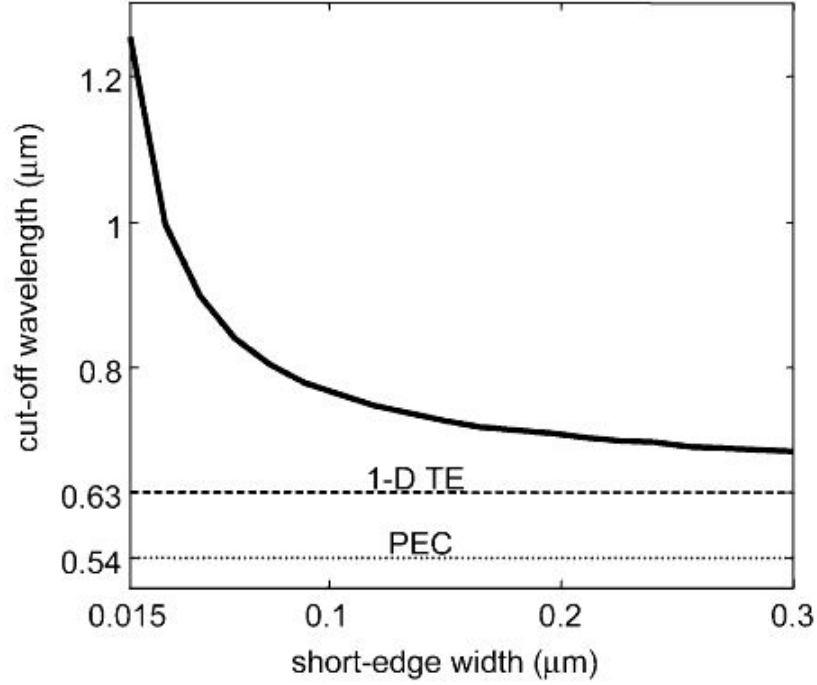


Figure 2.15: Calculated cutoff wavelength for modes in a rectangular hole with a long edge of  $270 \text{ nm}$  in silver. When the size of the hole is decreased, the cutoff wavelength increases. PEC cutoff wavelength of  $540 \text{ nm}$  and 1D (without SP-enhancement) cutoff wavelength of  $630 \text{ nm}$  are also shown for comparison [81].

The calculated cut-off wavelength of the  $TE$  mode of the rectangular aperture resulted from this approach, occurs at the wavelengths longer than  $2l$ . For a rectangular aperture in metal, it has also been shown that the field enhancement inside the aperture is associated with the maximum transmission through the aperture.

By setting the overall propagation constant,  $k_{TE}$ , to zero we can find the length of the aperture at resonance as [82]:

$$l = \frac{2}{k_0 \sqrt{\epsilon_d}} \text{arctan}\left(\sqrt{-\frac{\epsilon_m}{\epsilon_d}}\right) \quad (2.22)$$

It should be noted that the effective wavelength is twice the length of the aperture that gives the resonance. The reason for this convention is to show the wavelength

scaling with respect to the PEC case.

This result shows how the width of the rectangular nanohole and the wavelength of operation affect the resonant response.

## 2.9 Design Consideration

In order to achieve the optimal performance of plasmonic metasurfaces, some design factors should be considered. In this section, we discuss two of the most important factors: optimizing gap plasmons and thermal effect.

### 2.9.1 Optimizing Gap Plasmons

While plasmonic structures allow for the enhanced local field through the plasmonic resonance, an even greater local field can be achieved by having a gap between two metal surfaces. This is known as a gap plasmon [83,84].

Gap plasmons can enhance the fundamental beam power locally at the metal surface, which enhances the nonlinear optical response of the metasurfaces [85].

In 2005 a work showed that the field intensity enhancement in the gap region is inversely proportional to the gap size [84]. Although, for non-resonant structures, it was shown that as the gap size is decreased, the THG is enhanced [86]; for the resonant case, just decreasing gap size will not result in enhancement of nonlinear effects. So the optical resistive loss should be considered and an optimal gap size where the field intensity is maximized, is demanded.

The influence of gap size on THG was investigated based on various aperture arrays [86]. Figure 2.16 is the result of simulated scattering and the absorption cross-section spectra along with related THG for different gap sizes [86]. The result shows that maximum THG results from a gap of 4 nm (not the smallest size), where the

scattering and absorption cross-sections match each other.

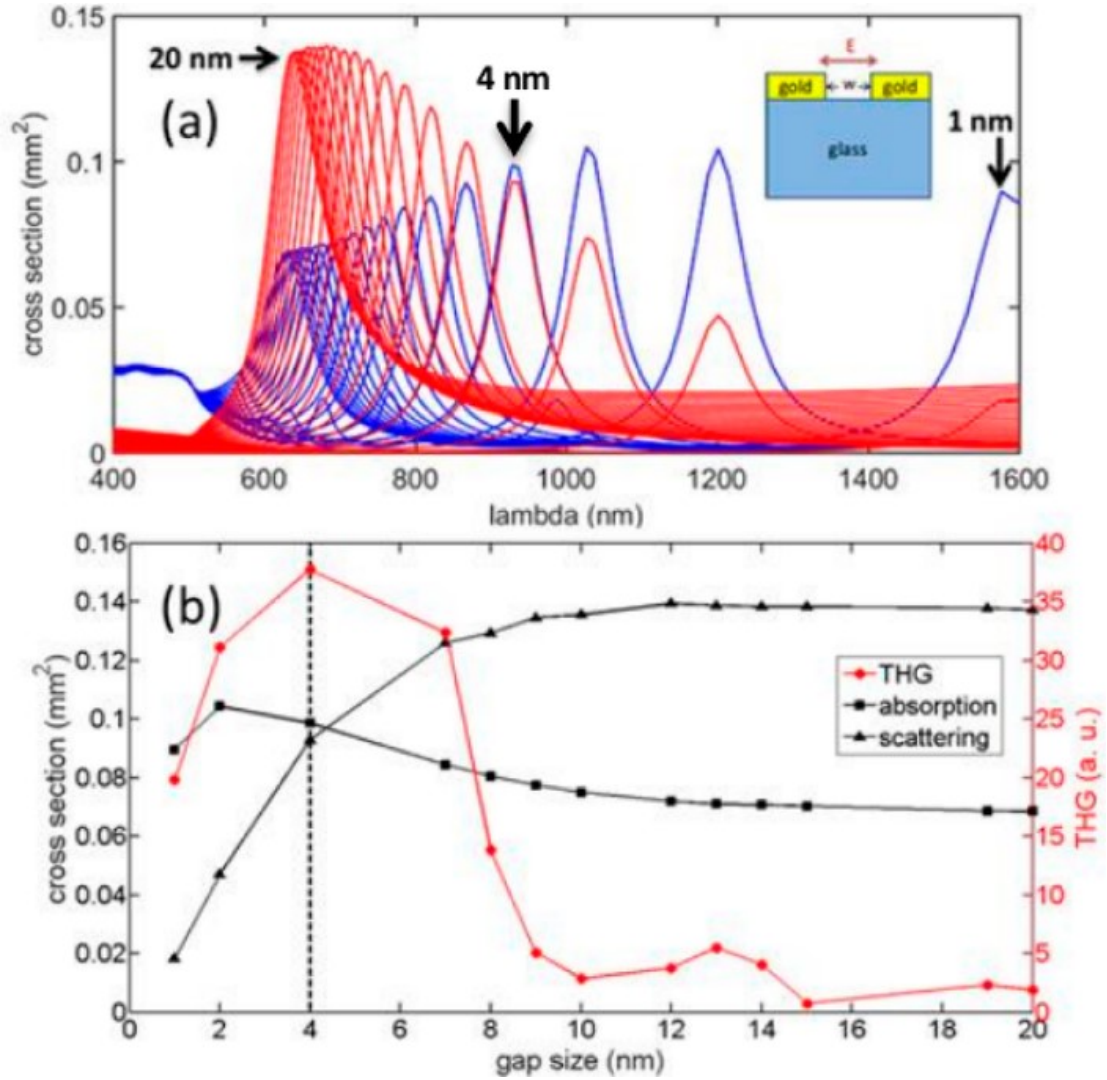


Figure 2.16: Absorption and scattering cross-section (black) and resonant THG prediction based on nonlinear scattering theory (red) for different gap sizes. Note that the optimal THG is predicted to occur when the absorption and scattering cross sections are equal [86].

While narrowing the gap in a metal nanostructure certainly leads to higher field concentration and a greater local density of optical states, it does not necessarily lead to the optimal third harmonic conversion. It has been shown previously for optical antennas that the optimal coupling to the antenna arises when the radiative and absorption rates are matched. It is noted that the wavelength shifts with changing

the gap size.

Within the context of a circuit description for metal nanostructures, the field enhancement in gaps may also be considered via capacitive variations. For a parallel plate capacitor, the charge stored on the plate (and hence the displacement vector in the gap) scales inversely as the gap distance for a given applied voltage [51]. Therefore, we expect similar scaling for the field enhancement in metal nanostructured gaps, considering also that the resonance frequency will be reduced as the capacitance increases.

There has been an interest in reducing gap sizes to obtain the highest possible field confinement [87]. The saturation of the plasmonic resonance shift was initially attributed to nonlocal effects from the Fermi-pressure. It has been shown that electron tunneling will shunt the gap and lead to reduced field enhancement [52, 60]. For example, a marked drop in the harmonic generation signal is observed when entering the tunneling regime [60]. Single atoms displaced in a gap can lead to sharp features that localize the electromagnetic field at the atomic scale [54]. Since this sharp feature is defined by a single atom, it may be considered the ultimate sharpness achievable in the plasmonic context.

On the other hand, the quantum mechanical effects dominate plasmon resonance for gaps smaller than 1 nm, therefore the limited the gap size is set to be larger than 1 nm [88].

### 2.9.2 Thermal Effects of the Incident Laser Beam on Nanostructures

Since the efficiency of the nonlinear harmonic generation is proportional to the fundamental beam  $\vec{E}_\omega$ , by increasing the incident beam power, several orders higher conversion efficiency can be achieved. But higher intensities may damage or even

melt the nanostructures. Therefore, the structures should be designed to minimize thermal damage by providing pathways for heat to escape. Figure 2.17 shows two samples of the damaged structures exposed by the same pulsed laser power [89]. In the coaxial structure, heat damage has happened, because the central islands are disconnected and so they melt under intense illumination. On the other hand, the H-structure does not show damage because it is in contact with the gold substrate, therefore heat can be removed effectively from the local hotspots.

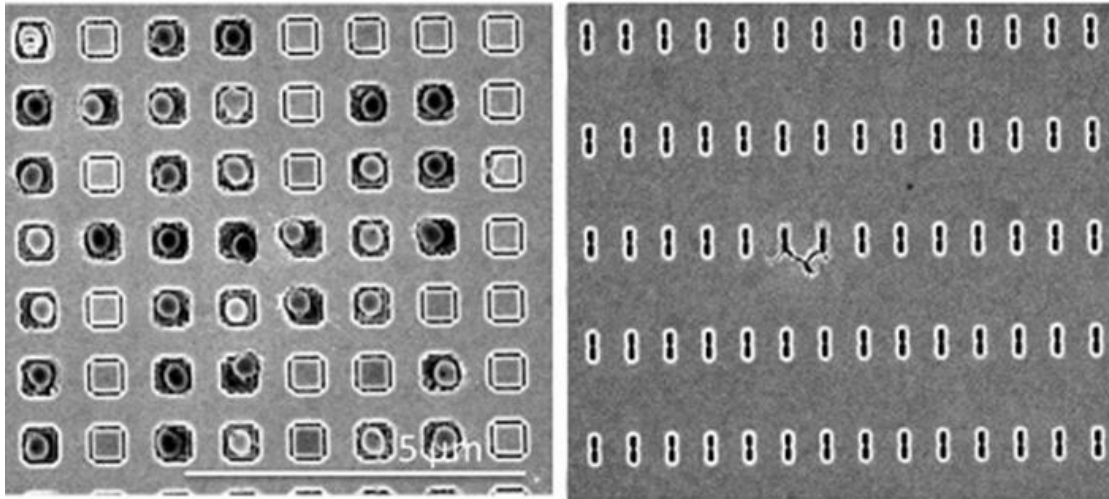


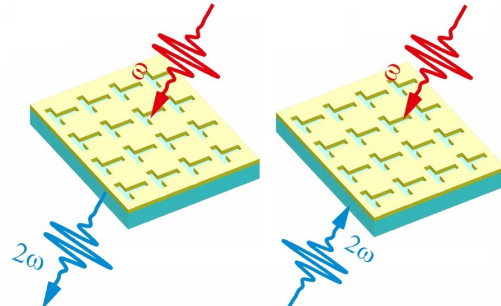
Figure 2.17: Examples of damaged structures caused by the high intense laser beam  
a) Closed loop (disconnected) apertures b) Connected structures [86]



## Chapter 3

# Theoretical Approach and Analytical Model

This chapter is dedicated to the theoretical models for describing metals at optical frequencies. For nonlinear generation, an approach to obtain an expression for the SHG power calculation is presented. This developed theoretical model can describe both the linear and nonlinear responses of structured metals. First, hydrodynamic theory and its perturbations and next, the nonlinear scattering theory as a complete electromagnetic response, gives the harmonic generation equations. The detailed discussions of the hydrodynamic model and its nonlocal and nonlinear properties taking place in this chapter lay the foundation of all the subsequent analytical and numerical studies performed throughout this thesis.



### 3.1 Nonlinear Optics

As it was briefly discussed in section 2.3, nonlinear optics deals with the phenomena that occur due to the modification of material properties in the presence of light of high intensity. The nonlinearity is associated with the fact that material response varies in a nonlinear manner with the applied optical field.

To study this effect, we consider the dependence of the electric dipole moment per unit volume, or material polarization  $\vec{P}$ , on the applied optical electric field,  $\vec{E}$ .

Considering the dipole approximation, an electric dipole is formed due to charge separation between the negatively charged electron cloud and the positively charged nucleus. In a linear regime, the induced dipole polarization can be expressed as [90]:

$$\vec{P} = \epsilon_0 \chi^{(1)} \vec{E} \quad (3.1)$$

where  $\epsilon_0$  is the permittivity of the free space and  $\chi^{(1)}$  is known as the linear susceptibility.

For larger applied EM fields and proportionately stronger oscillations, this approximation breaks down and nonlinear terms come into play which give rise to different frequency components in the oscillations [90]:

$$\vec{P} = \epsilon_0 [\chi^{(1)} \vec{E} + \chi^{(2)} \vec{E}^2 + \chi^{(3)} \vec{E}^3 + \dots] \quad (3.2a)$$

$$\vec{P} = \vec{P}_l + \vec{P}_{nl} \quad (3.2b)$$

where  $\chi^{(2)}$  and  $\chi^{(3)}$  are the second and third-order nonlinear optical susceptibilities respectively.

In general, the nonlinear susceptibilities depend on the frequency of the applied

EM field, but here for the sake of simplicity, the medium is assumed to be lossless and dispersion-less, as a result, the nonlinear susceptibilities are constant. If the vector nature of fields is also taken into account, then  $\chi^{(1)}$  is a tensor of rank 2,  $\chi^{(2)}$  a tensor of rank 3 and so on.

As equation 3.2 (b) shows, the polarization is composed of linear and nonlinear components. For incident light with low and moderate intensity, only the first term in equation 3.2 (equivalently equations 3.1) is important. It describes the linear optical responses, such as scattering and absorption. However, if the applied electric field is large enough (more than the atomic binding force  $\sim 10^{10}$  V/m), the higher-order terms in equation 3.2 need to be considered. In this case, the linearity condition would no longer be valid, and the polarization vector  $\vec{P}$  becomes nonlinear.

The interaction of metals with the electromagnetic field can be firmly understood in a classical framework based on Maxwell's equations. A time-varying nonlinear polarization is a source of nonlinear electromagnetic field components and hence is key to the description of nonlinear optical phenomena.

When an electric field is applied to a metallic particle the conduction electrons are displaced from their equilibrium position with respect to the core ions, causing a polarization of the particle and a depolarizing field that acts as a restoring force. Due to linear optics, the oscillating dipoles will radiate at the same frequency as the applied field in all directions. The response of an optical medium to the incident EM field is the induced dipole moment inside the medium. This is evident in the wave equation for nonlinear media [91]:

$$\nabla^2 \vec{E}_2 - \frac{n^2}{c^2} \frac{\partial^2 \vec{E}_2}{\partial t^2} = \frac{1}{\epsilon_0 c^2} \frac{\partial^2 \vec{P}_{nl}}{\partial t^2} \quad (3.3)$$

The nonlinear polarization  $\vec{P}_{nl}$  drives the electric field  $\vec{E}_2$  and the term  $\frac{\partial^2 \vec{P}_{nl}}{\partial t^2}$  represents the acceleration of charges in the medium. This is consistent with Larmor's

theorem that accelerating charges generate electromagnetic waves [92].

$\vec{P}_{nl}$  describes various nonlinear responses. Apart from harmonic generation, SHG, the nonlinearities resulting from second-order nonlinearity or a non-zero  $\chi^{(2)}$  include sum-frequency generation (SFG), difference frequency generation (DFG), and optical rectification (OR).

When a monochromatic laser beam of electric field strength represented by:

$$\vec{E}(t) = Ee^{-i\omega t} + c.c \quad (3.4)$$

is incident on a material with non-zero  $\chi^{(2)}$ , it induces a second-order polarization given as:

$$\vec{P}^{(2)}(t) = \epsilon_0 \chi^{(2)} (EE^* + E^2 e^{-2i\omega t}) + c.c \quad (3.5)$$

The second term oscillates with a frequency  $2\omega$  and is the second harmonic contribution to the polarization, while the constant first term represents a static electric polarization developed in the material (as vanishes) and represents OR. Also, it can be seen that the second-harmonic term scales quadratically with the incident electric field.

Upon irradiating the nonlinear material with two input pump beams with different frequencies ( $\omega_1$  and  $\omega_2$ ), the total electric field associated with the input waves is given by:

$$\vec{E}(t) = E_1 e^{-i\omega_1 t} + E_2 e^{-i\omega_2 t} + c.c \quad (3.6)$$

The second-order nonlinear polarization in this case is given as:

$$\begin{aligned} \vec{P}^{(2)}(t) = & \epsilon_0 \chi^{(2)} \left[ E_1^2 e^{-2i\omega_1 t} + E_2^2 e^{-2i\omega_2 t} + 2E_1 E_2 e^{-i(\omega_1 + \omega_2)t} + 2E_1 E_2^* e^{-i(\omega_1 - \omega_2)t} \right] \\ & + 2\epsilon_0 \chi^{(2)} [E_1 E_1^* + E_2 E_2^*] \end{aligned} \quad (3.7)$$

The different frequency components of  $\vec{P}^{(2)}$  can be expressed as:

$$\begin{aligned} \vec{P}(2\omega_1) &= \epsilon_0 \chi^{(2)} E_1^2; & (\text{SHG}) \\ \vec{P}(2\omega_2) &= \epsilon_0 \chi^{(2)} E_2^2; & (\text{SHG}) \\ \vec{P}(\omega_1 + \omega_2) &= 2\epsilon_0 \chi^{(2)} E_1 E_2; & (\text{SFG}) \\ \vec{P}(\omega_1 - \omega_2) &= 2\epsilon_0 \chi^{(2)} E_1 E_2^*; & (\text{DFG}) \\ \vec{P}(0) &= 2\epsilon_0 \chi^{(2)} (E_1 E_1^* + E_2 E_2^*); & (\text{OR}) \end{aligned} \quad (3.8)$$

It should be noted that in case of mixing between two pump beams, all the components in equation 3.8 are not present at the same time and it is mostly one component that is the dominant one, which is determined by the phase-matching condition.

Figure 3.1 shows an energy level diagram of the most common nonlinear processes.

## 3.2 Hydrodynamic Theory

Early work on the theoretical side of the plasmonic nonlinear response of metals was based on the free-electron model formulated by Jha [93]. Over a wide frequency range, the optical properties of metals were explained by a plasma model, where a gas of free non-interacting electrons of number density  $n$  moves against a fixed background of positive ion cores.

The majority of effects associated with the interaction with an electromagnetic field in metals are governed by this freely moving sea of conduction electrons.

In the presence of EM fields, electrons oscillate as a response to external EM fields,

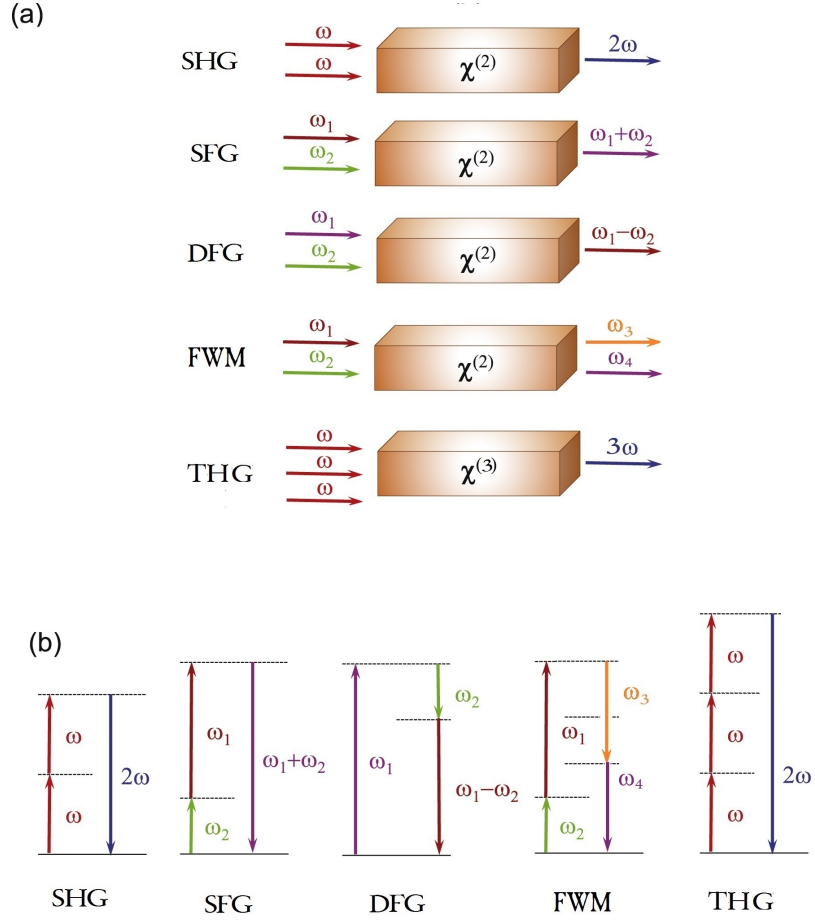


Figure 3.1: a) An illustration of the most common nonlinear processes. b) Nonlinear processes energy-level diagrams. The solid lines indicate the ground state while the dotted lines indicate virtual levels [65].

and the electron gas oscillations are damped via collisions occurring at the rate of the free electron relaxation time. The description of moving electrons in the presence of an applied electric field was introduced by Drude in his paper published in 1900 [94]. His model for the free electrons in metal was a simple, yet very successful model even at its time. The Drude model only takes conduction electrons into account which are subject to some damping, but within his model, he was able not only to explain the conduction of both electricity and heat but also the optical properties of metals.

Drude model speaks of a temporally varying electric force,  $\vec{F}$ , which is responsible

for displacing a charge carrier [94]:

$$m_e^* \frac{d^2 \vec{r}}{dt^2} = q \vec{F} - m_e^* \gamma \frac{d\vec{r}}{dt} \quad (3.9)$$

Here,  $m_e^*$  is the effective charge carrier,  $q$  is its charge, and  $\gamma$  describes friction or damping. The effective electron mass is used to account for some of the collective effects, such as the formation of a positive charge cloud in the vicinity of each electron. Employing such an effective mass, the electrons can be treated as free quasi-particles of mass  $m_e^*$ .

The effective mass  $m_e^*$  of the free electrons of a metal is in the simplified, one-dimensional case of the k-space given by [95]:

$$m_e^* = \frac{h^2}{\frac{\partial^2 E}{\partial k^2}} \quad (3.10)$$

where  $h$  is the reduced Planck's constant. This parameter in thin metal films (for example, Ag, Au, Cu) is usually evaluated from the measured transmission and reflection spectra in the range of the plasma reflection. Under the Drude model for electron gas in metals and the plasma frequency the plasma frequency, from the slope of the straight line when plotting the quantity of dielectric function against  $1/w^2$ , the effective can may be obtained [96]. This parameter is used in the following calculations.

The hydrodynamic Drude model, just like the Drude model, describes only the free electrons of a metal. The name hydrodynamic model comes from the fact that the electron gas (or electron liquid) is now described by hydrodynamic Euler type equations.

In the context of the hydrodynamic model, the first equation which governs a system of free electron gas is the continuity equation [91]:

$$\nabla \cdot \vec{J} + e \frac{\partial n}{\partial t} = 0 \quad (3.11)$$

where the particle current density is introduced as [91]:

$$\vec{J} = en\vec{v} \quad (3.12)$$

where  $\vec{v}$  considered as the velocity distribution, and  $\vec{J}$  as the current density of the free moving electron fluid.

The second fundamental equation is the Hydrodynamic Euler equation which was formulated by Sipe in 1980 [97]:

$$\frac{\partial \vec{v}}{\partial t} + (\vec{v} \cdot \nabla) \vec{v} + \gamma \vec{v} = \frac{e}{m_e^*} (\vec{E} + \vec{v} \times \vec{B}) - \frac{\beta^2}{n} \nabla n \quad (3.13)$$

where  $e$  is the electron charge,  $\gamma$  is the electron collision rate,  $\beta$  is a constant from Thomas-Fermi theory and  $\vec{E}$  is the external electric field.

In equation 3.13, the term  $(\vec{v} \cdot \nabla) \vec{v}$  as the convective acceleration term is the first term leading to the nonlinear polarizability. The damping force is described by a term proportional to the velocity ( $\gamma \vec{v}$ ). To describe the interaction of the liquid with an impinging electromagnetic field, the Lorentz-force, is described by  $\vec{E} + \vec{v} \times \vec{B}$ . The Lorentz-force term provides the coupling between the Hydrodynamic equations and Maxwell's equations (as does the current-density term in Maxwell's equations). The magnetic Lorentz part ( $\vec{v} \times \vec{B}$ ) is the second term responsible for the appearance of nonlocal nonlinearity effects. And the last term is due to the electron gas pressure, here described within the Thomas-Fermi model which accounts for the repulsion force between the electrons.

Giving rise to nonlocal effects, each of these terms lead to a nonlinear behavior due to a varying electron concentration and velocity under the stimulus of an



electromagnetic wave.

The prominent feature of the hydrodynamic model is that the equations are intrinsically nonlinear. The nonlinearity is a stronger deviation from the Drude model. SHG from metals can therefore readily be discussed within this model.

Combining two equations 3.13 and 3.11 and expanding all fields in a perturbative manner in the framework of the time-harmonic propagation ( $e^{-i\omega t}$ ), one finds that the free electron polarization  $\vec{P} = \vec{J}$  satisfies the following set of inhomogeneous equations [60, 98]:

$$\beta^2 \nabla(\nabla \cdot \vec{P}_1) + (\omega^2 + i\omega\gamma) \vec{P}_1 = \frac{ne^2}{m_e^*} \vec{E}_1 \quad (3.14a)$$

$$\beta^2 \nabla(\nabla \cdot \vec{P}_2) + (\omega^2 + i\omega\gamma) \vec{P}_2 = \frac{ne^2}{m_e^*} \vec{E}_2 + \vec{S}_{\text{NL}} \quad (3.14b)$$

where the nonlinear source,  $\vec{S}_{\text{NL}}$ , is given by:

$$\vec{S}_{\text{NL}} = \frac{e}{m_e^*} \vec{E}_1 (\nabla \cdot \vec{P}_1) + \frac{i\omega e}{m_e^*} (\vec{P}_1 \times \vec{B}_1) - \frac{\omega^2}{ne} \left[ (\nabla \cdot \vec{P}_1) \vec{P}_1 + (\vec{P}_1 \cdot \nabla) \vec{P}_1 \right] \quad (3.15)$$

The subscripts refer to the first and second-order fields.

Recalling the macroscopic Maxwell equations:

$$\nabla \cdot \vec{D} = \rho_{\text{ext}} \quad (3.16a)$$

$$\nabla \cdot \vec{B} = 0 \quad (3.16b)$$

$$\nabla \times \vec{E} = -\frac{\partial \vec{B}}{\partial t} \quad (3.16c)$$

$$\nabla \times \vec{H} = \vec{j}_{\text{ext}} + \frac{\partial \vec{D}}{\partial t} \quad (3.16d)$$

with the macroscopic fields  $\vec{D}$  (the dielectric displacement),  $\vec{H}$  (the magnetic field), the external charge density  $\rho_{ext}$  and the current density  $\vec{j}_{ext}$ .

Together with equations 3.14a and 3.14b under the assumption that the fundamental field remains undepleted, the fundamental and second order polarization vectors can be written as:

$$\vec{P}_1 = \frac{-1}{\omega + i\gamma} \frac{ne^2}{\omega m_e^*} \vec{E}_1 \quad (3.17a)$$

$$\vec{P}_2 = \frac{-1}{2\omega + i\gamma} \frac{ne^2}{2\omega m_e^*} \vec{E}_2 + \vec{P}_{NL} \quad (3.17b)$$

where the nonlinear  $\vec{P}_{NL}$ , is given by:

$$\begin{aligned} \vec{P}_{NL} = & \frac{e}{2\omega m_e^*(2\omega + i\gamma)} (\vec{E}_1 (\nabla \cdot \vec{P}_1)) + \frac{ie}{2m_e^*(2\omega + i\gamma)} (\vec{P}_1 \times \vec{B}_1) \\ & - \frac{\omega}{2ne(2\omega + i\gamma)} \left( (\nabla \cdot \vec{P}_1) \vec{P}_1 + (\vec{P}_1 \cdot \nabla) \vec{P}_1 \right) \end{aligned} \quad (3.18)$$

Expressing these in terms of current density,  $\vec{J}$ , gives:

$$\vec{J}_1 = \frac{i}{\omega + i\gamma} \frac{ne^2}{m_e^*} \vec{E}_1 \quad (3.19a)$$

$$\vec{J}_2 = \frac{i}{2\omega + i\gamma} \frac{ne^2}{m_e^*} \vec{E}_2 + \vec{J}_{NL} \quad (3.19b)$$

where:

$$\begin{aligned} \vec{J}_{NL} = & \frac{ine^3}{m_e^{2*}(2\omega + i\gamma)(\omega + i\gamma)} \times \\ & \left[ \frac{1}{\omega} \vec{E}_1 (\nabla \cdot \vec{E}_1) + i\mu \vec{E}_1 \times \vec{H}_1 + \frac{1}{(\omega + i\gamma)} \left( (\nabla \cdot \vec{E}_1) \vec{E}_1 + (\vec{E}_1 \cdot \nabla) \vec{E}_1 \right) \right] \end{aligned} \quad (3.20)$$

In Equation 3.19a, the first order term gives the usual linear Drude model for metals. Equation 3.19b with Equation 3.20 give the second-order response that is responsible for SHG and also OR.

The nonlinear source,  $\vec{J}_{\text{NL}}$ , given by equation 3.20 groups surface and bulk second harmonic contributions. The term containing  $\vec{E}_1(\nabla \cdot \vec{E}_1)$  gives the Coulomb interaction (referred to as a quadrupole-like term by virtue of its form),  $\vec{E}_1 \times \vec{H}_1$  gives the Lorentz magnetic force contribution, and the last two terms,  $(\nabla \cdot \vec{E}_1)\vec{E}_1 + (\vec{E}_1 \cdot \nabla)\vec{E}_1$ , are the contributions from convection.

The second-order optical response of the system (but also a rectification current for the case of THz generation) is due to both convection term and Lorentz magnetic term of Equation 3.20.

Besides all these contributions, there can be an interband contribution to the nonlinear response of gold that enhances this response, which is not considered within the scope of this report.

Combining these equations with Maxwell's equations, it is possible to calculate the linear and nonlinear response. Nonlinear scattering theory is one way to perform such calculations.

### 3.3 Nonlinear Scattering Theory

Nonlinear scattering (NLS) theory is a theoretical method for estimating the nonlinear response of metals by sequential linear electromagnetic calculations [69, 99, 100]. This approach is an extension of the Lorentz reciprocity theorem in a nonlinear media [99, 101, 102].

Here, employing the reciprocity theory, we discuss the excitation of a nonlinear field into a plane wave and the scattered plane wave field leaving a structure is modeled

by the equivalent but time-reversed field incident on the structure [103].

Reciprocity is an important concept in antennas because it produces implications when we reverse the role of transmitting antennas and receiving antennas. A formal derivation of the Lorentz reciprocity theorem begins by considering a volume containing two sets of current sources  $\vec{J}_1$  and  $\vec{J}_2$  and their corresponding emitted optical EM fields  $\vec{E}_1$  and  $\vec{E}_2$  in a reciprocal medium, as shown in Figure 3.2.

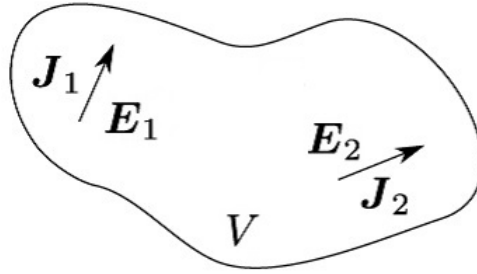


Figure 3.2: Volume containing two sets of electric sources and their corresponding EM fields

Lorentz reciprocity yields the following relation between the localized sources and the fields they emit over the volume of the excited nanostructure [104]:

$$\int \vec{J}_1 \cdot \vec{E}_2 dV = \int \vec{J}_2 \cdot \vec{E}_1 dV \quad (3.21)$$

where the integrals are taken over the volumes of the sources.

Looking at the nonlinear case, we select the current source  $\vec{J}_1$  as the stimulating factor of the nonlinear dipoles on the surface or in the volume of a nanostructure which are excited by the pump field. The current source and the polarization of the structures  $\vec{P}$ , are related as:

$$\vec{J}_1 = \frac{\partial \vec{P}}{\partial t} = i\omega \vec{P} \quad (3.22)$$

The dipoles emit unknown electric field  $\vec{E}_1$ . In the reciprocal condition (following

equation 3.21) the second source needs to be at the position of the detector. This is a current dipole source with a polarization axis of  $\hat{j}$  and a length of  $\Delta l$  that emits the electric field  $\vec{E}_2$ :

$$\vec{J}_2 = J_0 \delta(r - r_2) e^{i\omega t} \hat{j} \quad (3.23)$$

where  $(r - r_2)$  is the distance between the nanostructure and the detector. By substituting equations 3.22 and 3.23 into equation 3.21 we obtain an equation for estimating  $\vec{E}_2$ :

$$\int \vec{E}_1 \cdot J_0 \delta(r' - r_2) e^{i\omega t} \hat{j} dV = \int i\omega \vec{P} \cdot \vec{E}_2 dV \quad (3.24)$$

$$\vec{E}_1 \cdot \hat{j} = \frac{e^{-i\omega t}}{J_0 \Delta l} \int i\omega \vec{P} \cdot \vec{E}_2 dV \quad (3.25)$$

Figure 3.3 shows the illustration of the nonlinear scattering theory in the reciprocal configuration.

Equation 3.25 can be directly used to calculate the nonlinear emission; however, when using numerical solvers of Maxwell's equations, it is often inconvenient to calculate the field from a dipole placed at a detector far from the nanostructure because of the large range of lengths scales involved. Instead, a plane wave source with amplitude  $\vec{E}_{0,\text{plane}}$  is used.  $\vec{E}_{0,\text{plane}}$  can be calculated by solving for the Green's function for the Helmholtz equation as [99]:

$$\vec{E}_{0,\text{plane}} = \frac{i\mu\omega\Delta l J_0}{4\pi r} e^{-ikr + i\omega t} \hat{j} \quad (3.26)$$

Substituting in the magnitude of the field at the nanoparticle from the source at the detector, we obtain the nonlinear emission from the polarization  $\vec{P}$  in terms of an

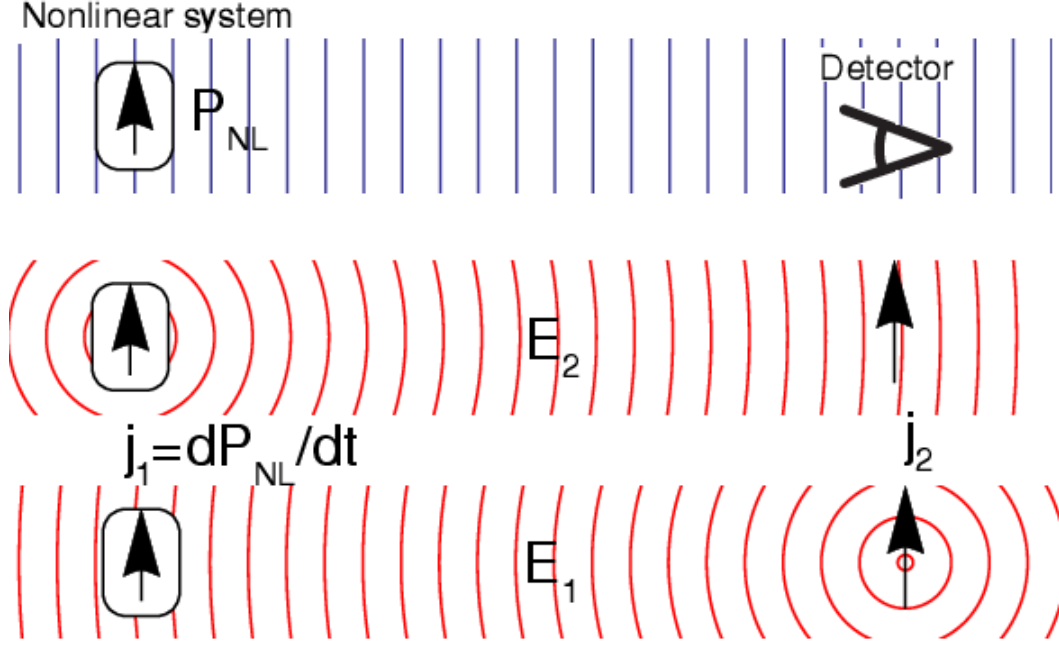


Figure 3.3: An illustration of nonlinear scattering theory. Depicted is a system of a nonlinear optical material and a detector. The source at the detector position radiates a field at the harmonic wavelength toward the structure [99].

overlap integral:

$$\vec{E}_{0,plane} \cdot \hat{j} = \frac{i\mu\omega^2 e^{-i\omega t}}{4\pi r} \int \vec{P} \cdot \frac{\vec{E}_2}{|\vec{E}_{0,plane}|} dV \quad (3.27)$$

where  $\vec{E}_2$  is obtained from the interaction of the plane wave of amplitude  $\vec{E}_{0,plane}$  with the nanostructure. This approach is computationally simple and accounts for the electrodynamic behavior of the structure including loss. This theory has been previously developed to estimate SHG in the reciprocal media [102].

Here, we use the above theory and equations to quantify the SHG in our aperture-based metasurface on a gold thin film.

Figure 3.4 shows the schematic of the SHG from an array of T-shaped apertures in transmission geometry. The emitted second harmonic signal can be measured by a detector (spectrometer or photodiode) on the other side of the sample.

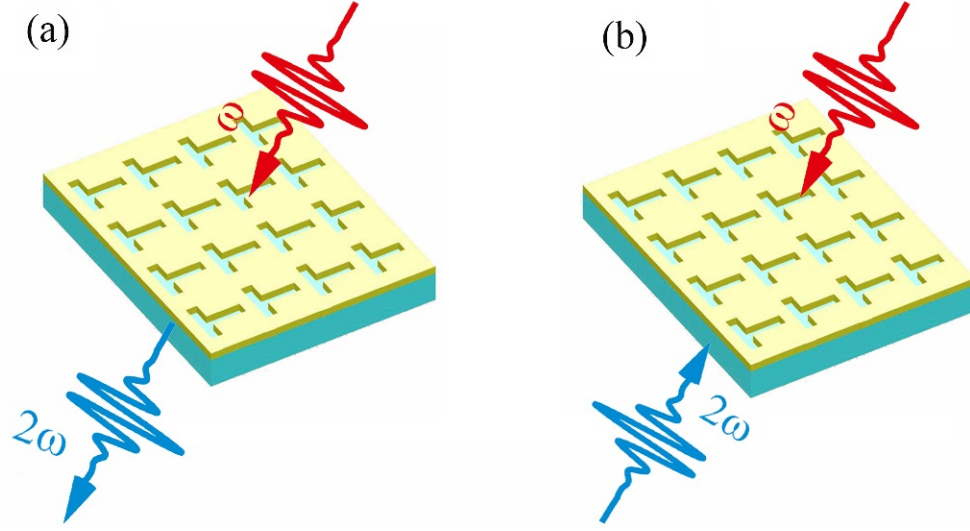


Figure 3.4: a) Schematic of SHG from a T-shaped aperture array. b) Simulated configuration for incident fundamental and second harmonic waves (the source at the detector position radiates a field at the harmonic wavelength toward the structure).

Of course, this same approach can be applied to THG. Using a local response model, the third harmonic may be considered to be instantaneously related to the local field intensity and may be expressed as  $\vec{J}_{NL}$  proportional to  $E_\omega^3$  [105]. In general, this will have a tensorial description. Others have shown how to calculate the third harmonic in this way [89, 105]:

$$P_{\text{THG}} = \int_{\text{Au}} \vec{J}_3 \cdot \vec{E}_{3\omega} dV \quad (3.28)$$

where  $P_{\text{THG}}$  is the THG power.

A surface-response based SHG can be calculated as [66]:

$$\vec{P}_2^{\text{surface}} = \chi_s^{(2)} E_n E_n \hat{n} \quad (3.29)$$

where  $\chi_s^{(2)}$  is the surface-normal second order susceptibility for gold, and  $E_n$  is the surface-normal component of the electric field.

### 3.4 Force on Magnetic Dipole from Electric Dipole

In the quasi-static regime, where the aperture size is very small compared to the wavelength ( $r \ll \lambda$ ), the field transmission through a subwavelength aperture can be approximated by the radiation from the magnetic dipole  $\vec{m}$  in the tangential direction and the electric dipole  $\vec{p}$  in the normal direction. It is interesting to consider the Lorentz magnetic contribution to the SHG as the cross product of these two dipoles.

In case of a plane wave incident at the angle  $\theta_i$  with respect to the normal plane on the aperture surface, the electric dipole moment is defined as [15, 106]:

$$\vec{p} = \frac{r^3}{3\pi} \epsilon_0 \vec{E} \sin \theta_i \quad (3.30)$$

similarly the magnetic dipole moment can be expressed as:

$$\vec{m} = -\frac{2r^3}{3\mu_0\pi} \vec{B} \quad (3.31)$$

where  $\epsilon_0$  and  $\mu_0$  are the free space permittivity and permeability,  $r$  is the aperture radius,  $\vec{E}$  and  $\vec{B}$  are the incident electric field and the magnetic flux density respectively.

In the case of normal incidence ( $\theta_i=0$ ), the radiation reduces to that of a single magnetic radiating dipole. For transverse magnetic angled incidence, the electric dipole plays a role as well.

The equivalent  $\vec{p}$  will serve as a local current and can also be expressed as:

$$\vec{p} = -i\omega \vec{J} \quad (3.32)$$

where  $\vec{J}$  is an infinitesimal current.

The lowest order force ( $\vec{F}$ ) on the localized current distribution in an external



magnetic field exposed by the magnetic dipole component part of the nanoaperture is calculated as [91]:

$$\vec{F} = \nabla(\vec{m} \cdot \vec{B}) \quad (3.33)$$

This also can be found to be written as [107]:

$$\vec{F} = (\vec{m} \cdot \nabla)\vec{B} + \vec{m} \times (\nabla \times \vec{B}) \quad (3.34)$$

The last term in Equation 3.34 contains the electric dipole contribution from the Ampere-Maxwell equation [91]:

$$\nabla \times \vec{B} = \mu_0(\vec{J} - i\omega\epsilon_0\vec{E}) \quad (3.35)$$

Substituting Equations 3.32 and 3.35 into Equation 3.34, yields:

$$\vec{F} = (\vec{m} \cdot \nabla)\vec{B} + \frac{\mu_0 i}{\omega}(\vec{m} \times \vec{p}) - i\omega\mu_0\epsilon_0(\vec{m} \times \vec{E}) \quad (3.36)$$

As Equation 3.36 shows, a component of the force is proportional to  $\vec{m} \times \vec{p}$ . It is natural to consider whether the response of an aperture follows the interaction between co-located effective electric and magnetic dipoles.

### 3.5 Angled Hydrodynamic SHG Theory

In order to calculate the SHG at the off-normal incident, here we develop our past hydrodynamic model, but include the incident angle in calculations.

Recalling equation 3.13, in case of incident EM field at an angle  $\theta$ , the Euler equation will be expressed as [97]:

$$\frac{\partial \vec{v}}{\partial t} + (\vec{v} \cdot \nabla) \vec{v} + \gamma \vec{v} = \frac{e}{m_e^*} (\vec{E}(\theta) + \vec{v} \times \vec{B}(\theta)) - \frac{\beta^2}{n} \nabla n \quad (3.37)$$

where  $\vec{E}(\theta)$  and  $\vec{B}(\theta)$  are the local electric field and magnetic flux density due to incident EM field at  $\theta$ .

Following previous development approach: expanding the fields, coupling with Maxwell equations along with the continuity equation, the fundamental and second harmonic terms in terms of current density  $\vec{J}$  can be obtained as [98]:

$$\vec{J}_1(\theta) = \frac{i}{(\omega + i\gamma)} \cdot \frac{ne^2}{m_e^*} \vec{E}_1(\theta) \quad (3.38a)$$

$$\vec{J}_2(\theta) = \frac{i}{(2\omega + i\gamma)} \cdot \frac{ne^2}{m_e^*} \vec{E}_2(\theta) + \vec{J}_{\text{NL}}(\theta) \quad (3.38b)$$

The nonlinear current source,  $\vec{J}_{\text{NL}}(\theta)$ , is given as:

$$\vec{J}_{\text{NL}}(\theta) = \frac{ine^3}{m_e^{*2}(2\omega + i\gamma)(\omega + i\gamma)} [\vec{J}_{\text{Lorentz}} + \vec{J}_{\text{Coulomb}} + \vec{J}_{\text{convective}}] \quad (3.39)$$

where

$$\left\{ \begin{array}{l} \vec{J}_{\text{Lorentz}} = -i \left( \vec{E}_1(\theta) \times \vec{B}_1(\theta) \right) \\ \vec{J}_{\text{Coulomb}} = \frac{1}{\omega} \vec{E}_1(\theta) \left( \nabla \cdot \vec{E}_1(\theta) \right) \\ \vec{J}_{\text{convective}} = \frac{1}{(\omega + i\gamma)} \left[ \left( \nabla \cdot \vec{E}_1(\theta) \right) \vec{E}_1(\theta) + \left( \vec{E}_1(\theta) \cdot \nabla \right) \vec{E}_1(\theta) \right] \end{array} \right.$$

Here we consider an extension of NSL theory to angled incidence. In this case, the incident source and the scattered plane wave contain the angular dependence. So  $\vec{J}_2(\theta)$  is calculated by excitation with  $\vec{E}_1(\theta)$  at an angle of incidence  $\theta_i$ . Then the second harmonic scattered, at angle  $\theta_s$ , is calculated by reciprocity using the time-reversal of a source incident at angle  $\theta_s$ .  $\theta_i$  and  $\theta_s$  are the incident and detection

angles respectively.

### 3.6 SHG Conversion Efficiency

If the beams are written in terms of beam intensities in power per unit area  $A$ , then it follows that the conversion efficiency for SHG is:

$$\eta_{\text{SHG}} = \frac{P_{\text{SHG}}}{P_{\text{F}}} \quad (3.40)$$

where  $P_{\text{F}}$  is the pump power at the fundamental frequency and  $P_{\text{SHG}}$  is the SHG power.

In the case of the normal incident plane wave as the pump source, let us recall equation 3.21. The first integral is the projection of  $\vec{E}_2$  onto the plane wave. Then  $\vec{J}_2$  are the sources that generate this field, and these are represented by Equation 3.19a, 3.19b and 3.20 along with Maxwell's equations. To calculate  $\vec{J}_2$ , we perform a calculation at the fundamental frequency for the field generated,  $\vec{E}_1$ . Then we calculate the current density  $\vec{J}_2$  from  $\vec{E}_1$  and dot product it with the field generated by  $\vec{J}_1$ . The power generated by  $\vec{J}_1$  is then calculated by a second calculation at the second harmonic frequency. Finally, for two current sources  $\vec{J}_1$  and  $\vec{J}_2$  and their corresponding emitted optical electric fields  $\vec{E}_1$  and  $\vec{E}_2$  in a reciprocal medium, Lorentz reciprocity theorem results in the following integral relation over the volume of the exciting nanostructure for SHG power:

$$P_{\text{SHG}} = \int_{\text{Au}} \vec{J}_2 \cdot \vec{E}_2 \, dV \quad (3.41)$$

where  $\vec{J}_2$  and  $\vec{E}_2$  are the current density and electric field respectively at the second harmonic frequency.

Equation 3.41 shows that for estimation of the SHG conversion efficiency, only

performing two linear calculations, one at  $\omega$  and the other at  $2\omega$  is sufficient.

In case of off-normal incident EM wave, the nonlinear SHG power, is then calculated as angular dependence of equation 3.41:

$$P_{\text{SHG}} = \int_{\text{Au}} \vec{J}_{\text{NL}}(\theta) \cdot \vec{E}_2(\theta) dV \quad (3.42)$$

Here substituting equations 3.38b and 3.39, the SHG power is then calculated as:

$$P_{\text{SHG}} = \frac{ine^3}{m_e^{*2}(2\omega + i\gamma)(\omega + i\gamma)} [P_{\text{Lorentz}} + P_{\text{Coulomb}} + P_{\text{convective}}] \quad (3.43)$$

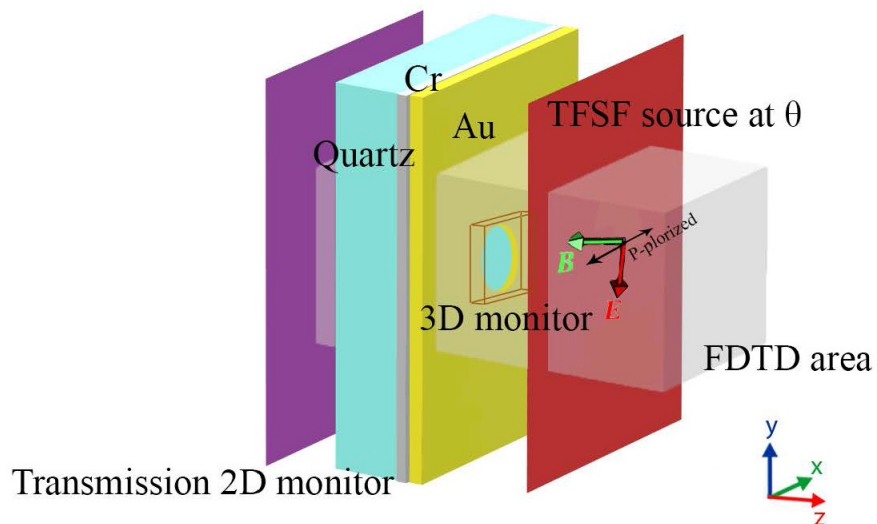
where

$$\left\{ \begin{array}{l} P_{\text{Lorentz}} = -i \int_{\text{Au}} (\vec{E}_1(\theta) \times \vec{B}_1(\theta)) \cdot \vec{E}_2(\theta) dV \\ P_{\text{Coulomb}} = \frac{1}{\omega} \int_{\text{Au}} \vec{E}_1(\theta) \left( \nabla \cdot \vec{E}_1(\theta) \right) \cdot \vec{E}_2(\theta) dV \\ P_{\text{convective}} = \frac{1}{(\omega + i\gamma)} \int_{\text{Au}} \left[ \left( \nabla \cdot \vec{E}_1(\theta) \right) \vec{E}_1(\theta) + \left( \vec{E}_1(\theta) \cdot \nabla \right) \vec{E}_1(\theta) \right] \cdot \vec{E}_2(\theta) dV \end{array} \right.$$

## Chapter 4

### Simulation Model

The Lumerical FDTD solutions version 8.15.736 was used to solve electric and magnetic fields of proposed structures within this dissertation. In this chapter, firstly an introduction to the finite difference time domain method then the Lumerical FDTD-solver software and some of the important simulation design features and parameters will be discussed. The next two sections provide more details on the projects and their corresponding simulations.



## 4.1 Finite Difference Time Domain Method

Finite difference time domain (FDTD) method known as the gold-standard for modeling nanophotonics devices, processes, and materials, is a numerical and vectorial method to solve two Maxwell's curl equations, Faraday's and Ampere's laws [103] in complex geometries:

$$\nabla \times \vec{E} = -\mu \frac{\partial \vec{H}}{\partial t} \quad (4.1a)$$

$$\nabla \times \vec{H} = \epsilon \frac{\partial \vec{E}}{\partial t} \quad (4.1b)$$

The FDTD method solves these equations on a discrete spatial and temporal grid [108–110]. FDTD solves equations in discretized computational space in a leapfrog algorithm using Yee's cell [111].

FDTD method is a time-domain method that allows for the determination of frequency response of the system by running just one simulation (impulse response). Yee's algorithm solves for both the electric and magnetic fields in time and space, using the coupled Maxwell's equations. Thus both the electric and magnetic material properties can be modeled within this method and set in the solver simulations software.

In three dimensions (3D), Maxwell equations have six electromagnetic field components:  $E_x$ ,  $E_y$ ,  $E_z$  and  $H_x$ ,  $H_y$  and  $H_z$ . As a schematic of a Yee's cell is Figure 4.1 shows, every  $\vec{H}$  component is surrounded by four circulating  $\vec{E}$  components and vice versa. At the beginning of each problem, the permittivity and permeability of the design material at each field component location is specified based on available models defined in the solver. The  $\vec{E}$  and  $\vec{H}$  components are updated using a leapfrog time-stepping algorithm [112]. This means every electric field for a specific time step

is calculated based on a previously calculated magnetic field. The same sequence is happening for the magnetic field calculations based on the previous electric field. This algorithm goes on until the end of the simulation for the proposed structure.

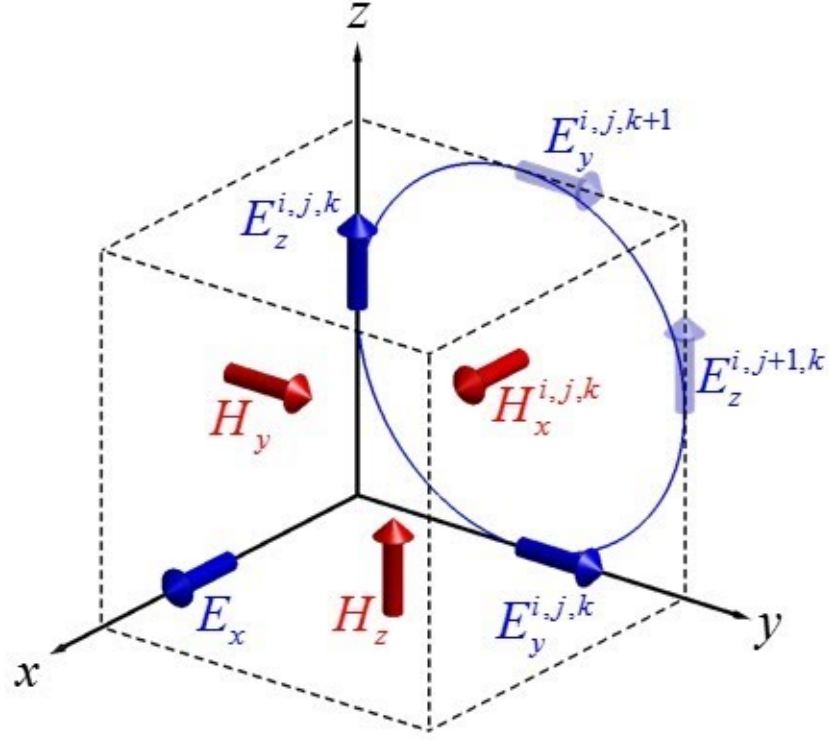


Figure 4.1: A schematic of Yee's unit cell

## 4.2 Convergence, Stability, and Accuracy of the FDTD

To approximate the solution of a partial differential EM equation via a finite difference scheme, one should analyze the problem by three important concepts: convergence, stability, and accuracy.

By definition, a finite difference scheme is convergent if the point-wise error tends

to zero as both the spatial and temporal step-sizes,  $\Delta x$  and  $\Delta t$ , tends to zero. In fact, the order of convergence gives a good indication of how well a solution of a finite difference scheme approximates the exact solution of a differential equation.

In an FDTD solver, upon excitation at each time-step the value of the waveform over that time period is added into the field value. The surrounding fields will propagate the introduced waveform throughout the FDTD grid appropriately, depending on the characteristics of each cell. The calculation must continue until a state of convergence has been reached. This typically means that all field values have decayed to essentially zero (at least 60dB down from the peak) or a steady-state condition has been reached. The use of high-performance computing systems allows us to use a very small mesh sizes in order to determine the convergence of the results and also evaluate the accuracy of the method. In this way, the convergence issues have already been addressed in the 2D [113, 114] and 3D cases for nanoplasmonics [115].

According to the Lax equivalence theorem, a solution based on finite difference scheme method is valid if and only if it is stable [116]. The 3D FDTD algorithm is stable according to the Courant-Fredrichs-Lewy stability condition in which the time-step is bounded by the limit [116]:

$$\Delta t \leq \frac{1}{c_0} \frac{1}{\sqrt{\frac{1}{(\Delta x)^2} + \frac{1}{(\Delta y)^2} + \frac{1}{(\Delta z)^2}}} \quad (4.2)$$

From Equation 4.2, it can be seen clearly that the choice of time step cannot be independent of the mesh sizes. As we increase the time step while keeping the mesh size fixed (or decrease the mesh size while keeping the time step fixed) the FDTD method eventually becomes unstable. As a result, a stability analysis must be performed in order to determine the Courant-Fredrichs-Lewy stability limit [117].



### 4.2.1 Sources of Error in an FDTD Simulation

Numerical simulation results will never give exactly the correct answer; there is always some numerical error. It is important to understand the sources of numerical errors and steps that can be taken to reduce the error to an acceptable level. Reducing the error often involves increased simulation time and memory and so it is important to consider what an acceptable level of error is, so that the simulations can be run as quickly as possible. Within the FDTD solvers there are possible methods for convergence testing of results, so the possible sources of error in a simulation and quantify the level of convergence can be determined.

It is often assumed in FDTD that the error in a simulation result always diminishes with decreasing grid size. In reality, there are more sources of error that need to be considered. One of which is the PML boundary condition.

The PML always has some reflection which can be theoretically calculated and changes with incident angle. Any reflection from the PML can re-interfere with the source, leading to incorrect power normalization, or simply re-interfere with the true scattered fields of the structure. Increasing the number of PML layers can reduce this reflection error.

FDTD grid dispersion also can be a source of error. When  $\Delta x$ ,  $\Delta y$ ,  $\Delta z$ , and  $\Delta t$  are finite, the dispersion relation on the FDTD mesh is not identical to free space. In principle, this source of error can be reduced indefinitely by reducing the spatial and temporal mesh to 0. However, there is always a limit to how far the mesh size can be reduced without introducing new sources of numerical error. Also one major drawback of FDTD is that the computation time scales as the fourth-order of the simulation domain size, and the memory requirements as the third order [108]. Therefore choosing the right mesh size in calculations plays an important role in terms of accuracy and calculation time.

The staircasing effect is another error source [118–120]. Staircasing is the name used to describe the representation of non-aligned or curved surfaces on an orthogonal grid. For finite values of  $\Delta x$ ,  $\Delta y$ , and  $\Delta z$ , it is not possible to resolve geometric features to arbitrary resolution. There will always be a geometric error for a finite-sized mesh. Staircasing error also can be reduced by making the mesh size smaller, but eventually, other numerical considerations due to the finite precision of the numbers used will limit how small  $\Delta x$ ,  $\Delta y$  and  $\Delta z$  can go. Staircasing can be one of the main sources of errors in FDTD. Advanced sub-cell techniques, like "conformal mesh" setting [121], to model curved surfaces in FDTD for dispersive and non-dispersive media are well known and used.

Furthermore, in the FDTD method, it is not possible to use the dispersive refractive index as a function of wavelength (or frequency) directly. Instead, FDTD solver software fits the dispersive material properties to models that can be solved efficiently in the time domain. The imperfection in the fitting function and models also can be considered as an error source.

Lastly, sources and monitors might cause a variety of small errors as well. For example, all sources will have a small reflection which gets worse further from the center frequency of the source. This problem is also reduced as the mesh size decreases. Monitors, also, by default will interpolate the fields to certain desired locations, leading to additional interpolation error.

### 4.3 Lumerical FDTD Software

Lumerical FDTD is a high-performance 3D FDTD-solver that is used to solve Maxwell equations for the design, analysis, and optimization of nanophotonic devices and materials. This software delivers reliable, powerful, and scalable solver performance

over a broad spectrum of applications; such as surface plasmons, metamaterials, solar cells, and integrated optical structures.

To implement an FDTD simulation, the user would need to define a computational space and the material model to use. The Lumerical FDTD simulation relies on the electromagnetic field and structural material in a time step that is related to the mesh size via the speed of light, to give a frequency domain and time domain results to the user. In addition, FDTD can obtain the frequency solution by exploiting Fourier transforms, thus a full range of useful quantities can be calculated, such as the complex Poynting vector and the transmission/reflection of light. Figures 4.2 and 4.3 depict the platform of the Lumerical computational space and a screenshot of the proposed design structure in the computational space.

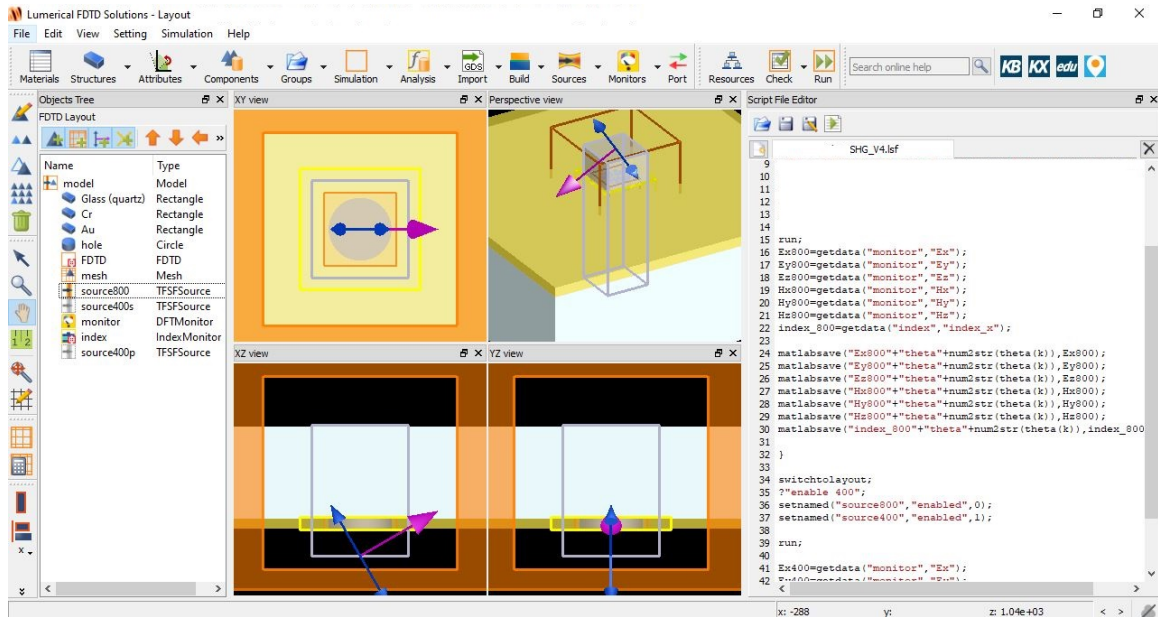


Figure 4.2: A screenshot of platform of the Lumerical computation space.

Before initiating the simulation in Lumerical FDTD some important parameters should be carefully taken into account. The proper implementation of the proposed structure and choosing the correct parameters within the software lead to reliable output results. Otherwise either the results are not trustworthy or the simulation

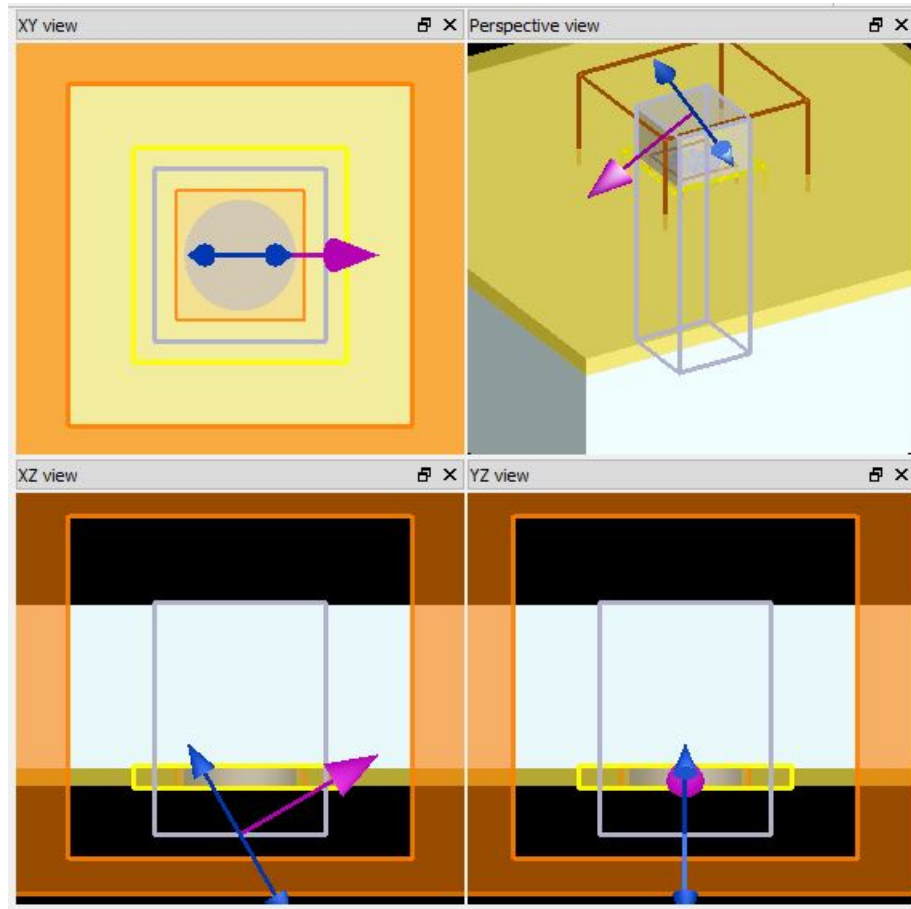


Figure 4.3: A screenshot of proposed designed structure in numerical computational space.

diverges. During the designing of the structures and running simulations in this report, some simulation design features and parameters have been chosen that the most important ones are discussed here.

### 4.3.1 Grid Size

While defining an FDTD model for a given problem, one has to carefully note the meshing and choose the proper grid size. FDTD uses a rectangular, Cartesian style mesh. It's important to understand that the fundamental simulation quantities (material properties and geometrical information, electric and magnetic fields) are calcu-

lated at each mesh point. Obviously, using a smaller mesh allows for a more accurate representation of the device, but at a substantial cost of time and memory. As the mesh size becomes smaller, the simulation time and memory requirements will increase. By default, the simulation mesh is automatically generated. To maintain accuracy, the meshing algorithm will create a smaller mesh in the high index (to maintain a constant number of mesh points per wavelength) and highly absorbing (resolve penetration depths) materials. In some cases, it is also necessary to manually add additional meshing constraints. Usually, this involves forcing the mesh to be smaller near complex structures (often metals) where the fields are changing very rapidly.

To set the grid size of the simulation, some rules should be taken into considerations. Firstly, the grid (mesh) size should be much smaller than the smallest wavelength in the simulation, especially for plasmonic studies (since propagation constant becomes very large and wavelength becomes very small). A rule-of-thumb is that the shortest wavelength must correspond to at least five unit cells. Another factor for choosing the grid size is the geometry of the structure. The grid size should be smaller than the smallest geometrical features of the structure. In this case, the smallest geometrical dimension should be divided into at least two or three cells. This mesh sizing obviously will result in a longer simulation time when dealing with rough surfaces or sharp edges.

### 4.3.2 Boundary Conditions

Boundary conditions are imposed to terminate the simulation domain and define the fields at the simulation boundaries. The FDTD solver supports a range of boundary conditions, such as perfect electric conductor (PEC), perfect magnetic conductor (PMC), Bloch, periodic boundary condition (PBC), and absorbing boundary condi-

tion or perfectly match layer (ABC/PML). PEC and PMC are used to represent ideal electric or magnetic conductors. When studying periodic systems, PBC allows you to calculate the response of the entire system by only simulating one unit cell. PBC is relatively straightforward to use by simply setting the simulation span to be one unit cell wide and selecting PBC for the boundaries. When the simulation runs, the PBC simply copies the EM fields that occur at one side of the simulation and inject them at the other side.

PML absorbing boundary conditions [122]](or ABC [123]) are used to absorb outgoing waves to minimize reflections from boundaries. They essentially model open or reflectionless boundaries. Therefore, PML is needed to simulate an infinite open space, to prevent outward going waves from reflecting back to the simulation domain. In a different perspective, PML boundaries are implemented as an absorbing material that is also impedance matched to the surrounding materials, to minimize reflections. An ideal PML boundary produces zero reflections. However, in practice, there will always be small reflections due to the discretization of the underlying PML equations.

In Lumerical FDTD, the user can directly specify all the parameters in simulation regions that control their absorption properties including the number of layers. To facilitate the selection of PML parameters, a number of profiles (or predefined sets of parameters) are available under the boundary conditions setting. In most simulation scenarios, the user only needs to choose one of the predefined profiles and fine tune the number of layers.

### 4.3.3 Sources

The Lumerical FDTD solver supports a number of different types of beam sources such as point dipoles, plane waves, total-field scattered-field (TFSF) source, a guided-mode source for integrated optical components, and an imported source to interface

with external photonic design software.

Although the point sources are sometimes useful in theoretical considerations, most practical problems involve more complicated source fields. One frequently used source model is a plane wave source.

Plane wave sources are used to inject laterally-uniform electromagnetic energy from one side of the source region. In the simplest case, a plane wave is produced by choosing field locations along a line parallel to a coordinate direction and applying the added source technique. It is also possible to inject a plane wave at an angle. The plane wave source is actually the same object as the Gaussian source, with the only difference being the source shape. For the T shaped aperture project in this report, this source mode was generally used, but for sources at an angle, TFSF source mode was used.

The TFSF source is an advanced version of the plane wave source designed primarily for particle scattering simulations, where the particle may be in a homogeneous medium or on a multi-layer substrate. The unique aspect of this source mode is that the source will "subtract" the same plane wave when it arrives at one of the boundaries of the source. The subtraction happens at the boundaries of the source and a reference one-dimensional line at the top right corner of the TFSF boundary is used to determine the indices profile of all the boundaries. The TFSF source separates the computation region into two distinct regions:

- Total field region includes the sum of the incident field wave plus the scattered field.
- Scattered field region, includes only the scattered field.

Some simulation objects such as frequency-domain field monitors which collect the field profile in the frequency domain from simulation results across some spatial

region and index monitors which record the  $n$  and  $k$  values as a function of frequency/wavelength in a simulation are usually used along with the sources within the simulation in the FDTD solvers.

## 4.4 Simulation Model

The proposed structures in this project were modeled in Lumerical FDTD software. The simulation bulk model was composed of three layers of materials with different refractive index stacked up together. A metallic thin film consists of a 100 nm with 5 nm titanium as an adhesive layer on glass substrate. The metal thin film was placed in the simulation area where its surface is positioned perpendicular to the  $z$ -axis.

Following the Lorentz reciprocity, two separate simulations were performed in this study. One at the fundamental wavelength which results in the electric field and magnetic flux density,  $\vec{E}_1$  and  $\vec{B}_1$ ; and one at the second harmonic wavelength resulting in electric field and magnetic flux density,  $\vec{E}_2$  and  $\vec{B}_2$ .

A MATLAB ©(Mathworks MATLAB ver. *R2018b*) script was written to calculate each SHG hydrodynamic contribution term (See Appendix B). The total SHG was then calculated as the sum of all three contributions.

Since we had open boundaries in real experiments, the boundary condition was set as PML. PML minimizes reflection at the boundaries.

The complex permittivities of gold, chromium, and titanium were modeled using the experimental data of Johnson and Christy [124], CRC [125] and Palik [126] respectively. For the glass layer a refractive index of 1.52 was used and for the background space, 1.

The simulation model itself consists of a single T-shaped structure. Two 3D monitors at the fundamental wavelength and second harmonic wavelength around the



aperture region were used to collect the induced fundamental and second harmonic beams in the gold and dielectric region. Another 3D index monitor was used in the  $xy$  plane to collect the refractive index of the material. Using this technique, dielectric and metal regions could be distinguished.

Frequency/power domain monitors were defined to extract fundamental and second harmonic electric fields for dielectric and gold regions. A mesh override region with the same dimensions as the 3D monitors was used. We used 2.5  $nm$  mesh size in all directions. The conformal mesh 1 refinement technology that is reliable in metal-dielectric structures was utilized.

To avoid possible numerical artifacts due to the field localization near metal corners, we considered rounded corners with a radius curvature of 5  $nm$ .

Source waves propagating along the  $z$ -axis are generated by the TFSF technique for off-normal incidents and plane wave for normal incident simulations. TFSF sources were used to prevent aperturing of the source for subwavelength simulations and to reduce interactions with the boundaries of the simulation.

Stabilized PML absorbing boundary conditions were employed at all boundaries, making sure that the simulations had no reflection at the boundaries.

Only one circular aperture (unit cell) was needed in the computational area. A 1000 femtosecond simulation time had been set long enough to calculate all the existing field responses in the simulation area.

A schematic of the simulated structure for off-normal incidence along with the simulation elements is shown in Figure 4.4.

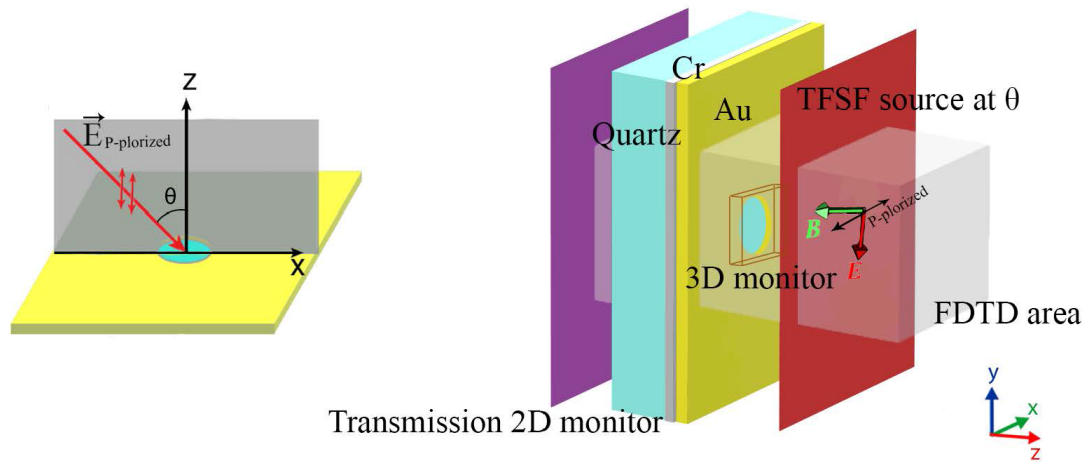
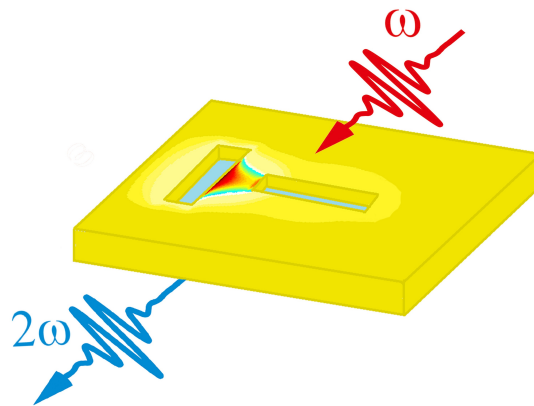


Figure 4.4: A schematic of the simulated structure for off-normal incident along with the simulation elements. Shining the P-polarized electromagnetic field at angle  $\theta$  on the structure.

## Chapter 5

# Nanofabrication and Experimental Details

This chapter presents a description of the fabrication method of the T-shaped array structures in gold films using a focused ion beam milling method. Later on, it is shown how the scanning electron microscopy can be used as an efficient tool for imaging and characterization of the fabricated structures. Lastly, the details of the optical setup are discussed.



## 5.1 Nanofabrication

Focused ion beam (FIB) milling refers to a technique or instrument that utilizes accelerated ions of moderately heavy atoms, such as gallium or helium, for either analysis or milling of a material. Apart from being popular among material scientists, biologists, and semiconductor engineers, FIB is one of the main tools deployed in the nano-science and semiconductor industry for fabricating features in nanometer fabrication accuracy.

Sub-wavelength apertures on gold films proposed in this project were planar in design, involving metallic films with surface features fabricated using FIB.

The basics of the FIB system consists of a vacuum system and chamber, liquid metal ion source, sample stage, detectors, and a computer to run and control the system. The operation principle of FIB resembles a scanning electron microscope (SEM), but it uses a highly focused beam of positive ions instead of negative electrons. A stream of high velocity ions bombards the surface of the sample, resulting in controllable material removal. Beam steering, alignment, and astigmatism correction are performed with a set of condenser, octopole, and objective magnetic lenses. A detector is usually positioned beside the sample to collect the reflected ions for creating real-time images.

The Hitachi FB-2100 at the advanced microscopy facility (AMF) at the University of Victoria was used for the fabrication of apertures in this report (Figure 5.1). A commercially available slide from EMF Corp. (EMF-corp TA134), with a 100 *nm* gold layer, evaporated on a glass substrate through a 5 *nm* titanium adhesion layer, was used for milling these structures.

Hitachi FB2100 FIB software is capable of milling patterns, represented by an image file, onto the target sample. The milling patterns, then, are input into the FIB controlling computer in the format of a bitmap figure. The bitmap figure was designed

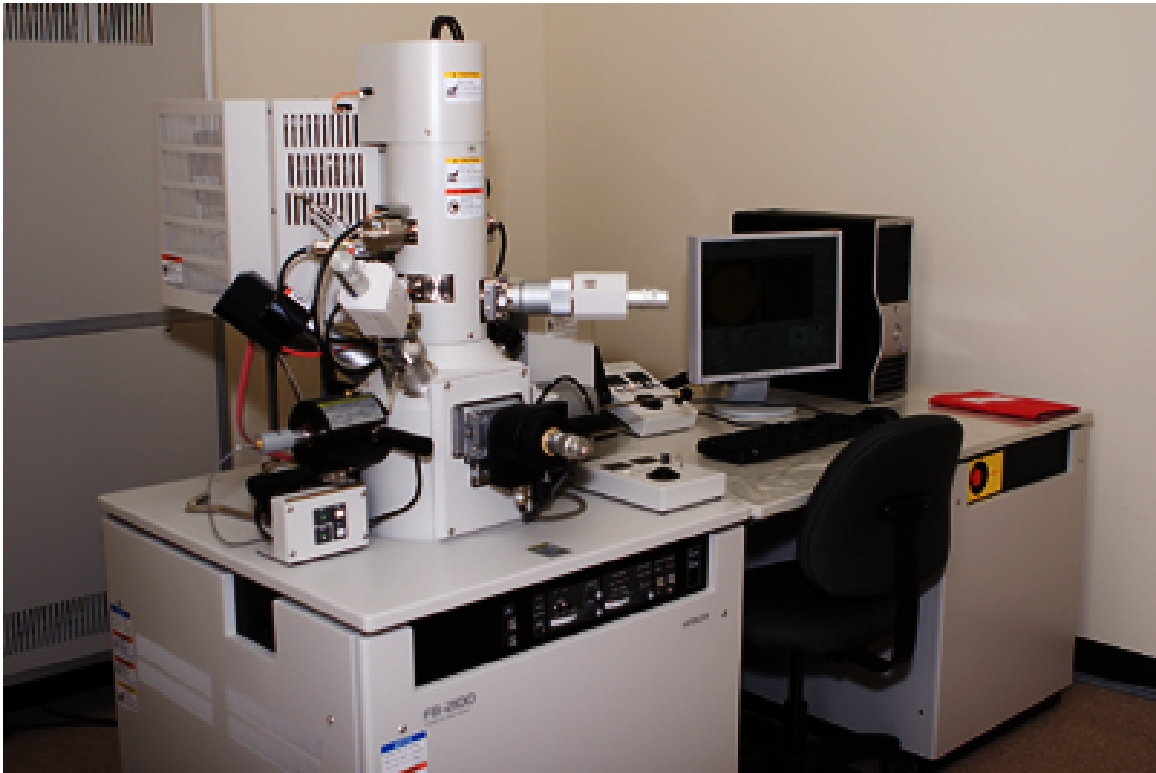


Figure 5.1: Hitachi FB2100 FIB machine at the University of Victoria.

in Adobe Photoshop © by creating an image of the desired structures in black and white (for black pixels which get exposed and white pixels do not get exposed). The image could then be exported as a bitmap figure. The bitmap has a resolution of  $2000 \times 2000$  pixels, corresponding to a real area of  $400 \times 400 \mu\text{m}^2$ .

Various parameters in fabrication such as dwelling time, ion beam current, degree of ion beam defocusing, and relative interaction diameter can affect the spot size of the ion beam on the target surface, hence improving or degrading the resolution and accuracy.

In our setting for FIB milling the  $\text{Ga}^+$  beam sweeps the bitmap pattern with parameters listed in table 5.1.

Usually, multiple beam configurations are available with this FIB machine. The beam 40-1-5 as the main milling beam, 40-0-30 as the align viewing beam, and 40-

Table 5.1: FIB fabrication parameters.

Parameter	value
dwelling time	3 $\mu s$
beam current	30 $pA$
acceleration voltage	40 $kV$
magnification	22 $k\times$

1-300 for rough cutting and rough thinning were used. The first two digits of the beam label show the acceleration voltage in kV, the middle digit represents whether the condenser lens is on or off and the last digit is the beam intensity ( $Ga^+$  aperture size). The condenser lens provides better accuracy and increases the beam power. The aperture size controls the number of ions that fall on the surface.

The number of sweep iterations depends on the gold thickness and it is about 55 times for a 100  $nm$  gold film using a 40-1-5 beam at the magnification of 22  $k\times$ . Reducing the number of iterations and increasing the dwell time may have the same result, however, larger dwell time increases the heat and deforms the edges of the gold during the milling process. In our project, the apertures were fabricated with lengths varying from 200  $nm$  to 280  $nm$  and rotated along the  $x$  axis from  $0^\circ$  to  $90^\circ$  in steps of  $15^\circ$ .

## 5.2 Scanning Electron Microscopy

The resolution in optical microscopy depends on the wavelength  $\lambda$ , and suffers from the diffraction limit (recall equation 2.1). With UV as the light source, the smallest possible spot size is a few hundreds of nanometers.

Electron microscopes are, consequently used to resolve objects normally smaller than  $1\mu m$  with resolutions on the nanometer scale that optical microscopes fail to resolve. In particular, scanning electron microscopy (SEM) is used to observe the

structure of the surface of a specimen. Due to greater focal depth comparing to optical microscopes, stereoscopic imaging is also possible with electron microscopy. Many SEMs have an x-ray analyzer for compositional analysis of the desired region.

In this research, SEM was used extensively to characterize the fabricated structures. SEM model Hitachi S-4800 FESEM at the AMF at the University of Victoria has been used widely throughout this research report (Figure 5.2).



Figure 5.2: Hitachi S-4800 FESEM machine at the University of Victoria.

As a result of the incident electron beam's interaction with the surface of the specimen, secondary electrons, backscattered electrons, characteristic x-rays, and other signals are generated. To form an image, SEMs use the secondary electrons and backscattered electrons. The fine topographical image of the sample results from secondary electrons which are generated near the surface of the sample. The backscattered electrons are those electrons that are reflected upon striking the atoms of the

sample under observation. Therefore detecting these electrons along with an x-ray analyzer leads to a compositional analysis of the specimen. This way the type and percentage of the elements included in the sample can be observed.

The main parts of the SEM device are an electron gun, condenser lens, deflection coil, objective lens, secondary electron detector, display, and vacuum pump.

In this thesis, there are examples of SEM images from our works that are mainly used to evaluate the quality of fabricated structures.

A sample SEM image of the fabricated structures is shown in Figure 5.3

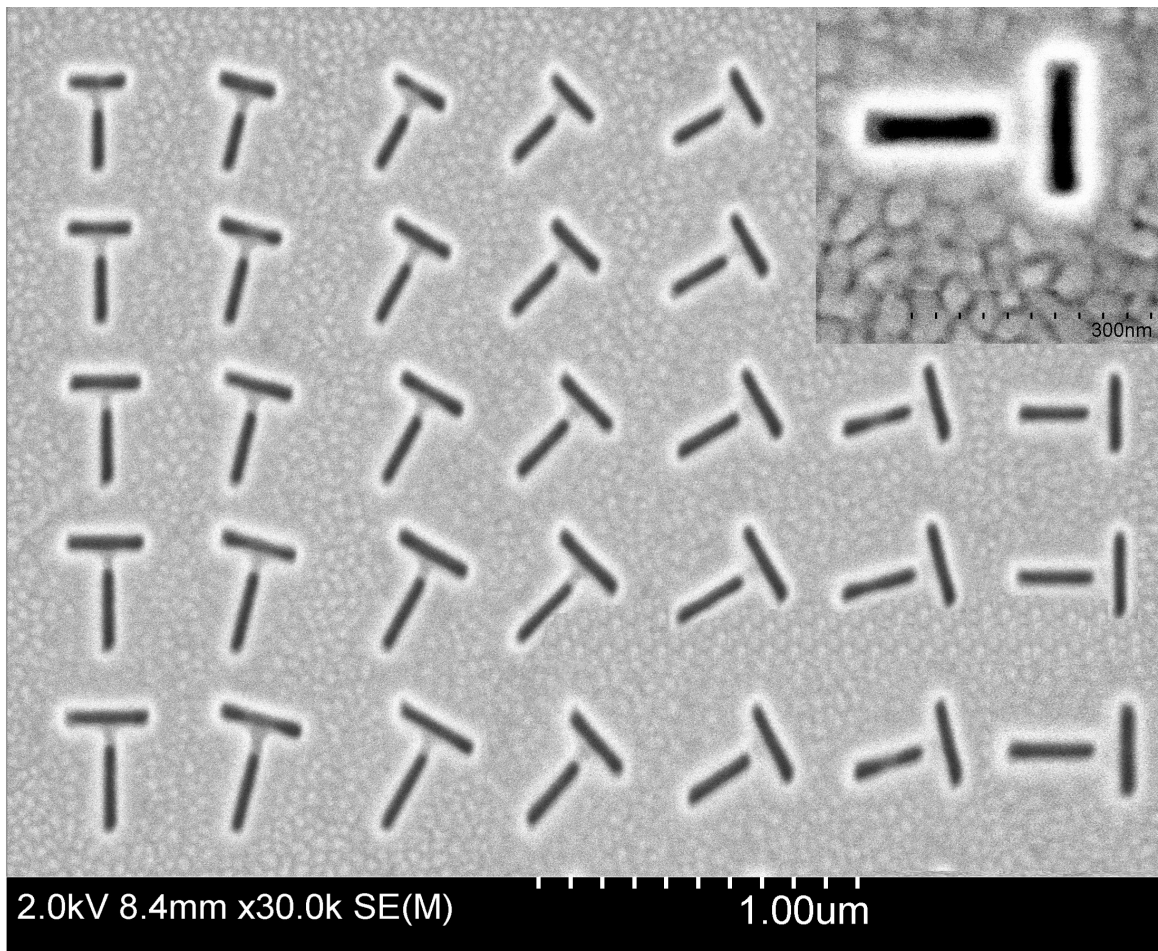


Figure 5.3: A sample SEM image of the fabricated structures.



### 5.3 Optical Transmission Setup

Throughout this project, characterization techniques were deployed to determine the optical response of the fabricated devices. The spectral measurement setup was mainly based on the standard inverted laser scanning microscopes (LSM). Here the confocal laser scanning microscope (LSM 880 Zeiss) machine was used as the base of our measurement tool (Figure 5.4). Polarization measurements required a slight modification to this configuration, where an analyzer was added to the existing setup.

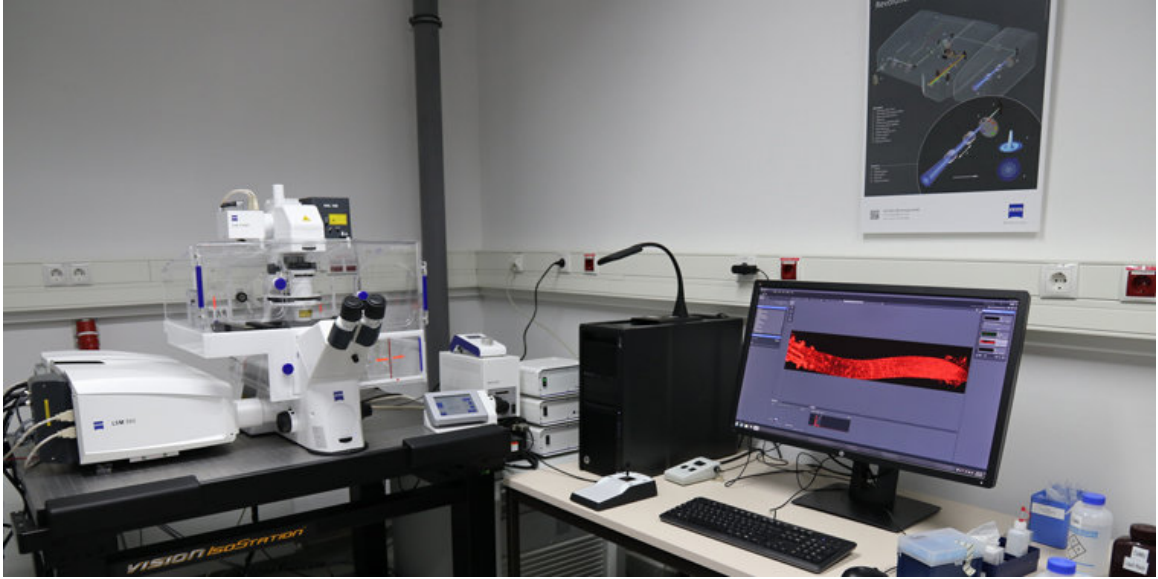


Figure 5.4: LSM 880 Zeiss machine used for optical measurements

The main part of the experimental setups is a pulsed laser that delivers a high amount of energy to the sample in a small fraction of the time. A  $140\text{ fs}$  pulse laser at  $850\text{ nm}$  at a repetition rate of  $80\text{ MHz}$  was used as the fundamental light source. This intense source stimulates the nonlinear processes that were measured by a fast response spectrometer.

The maximum applied power was limited to  $40\text{ mW}$ , low enough to avoid any thermal damage or melting of the examined structures while the peak power is high enough to generate nonlinear signals. The pump light was filtered by a  $690\text{ nm}$

dichroic mirror to remove the laser incident light at its harmonic frequencies prior to the sample. The incident light was focused onto the sample using a  $50\times$  microscope objective lens with  $\text{NA}=0.7$ . The emission beam on the other side of the sample, containing the SHG and the scattered fundamental beam, was collected with another microscope objective lens, passing through a band-pass blue filter to remove the fundamental beam before the analyzer. The color filter has about 30% transmission in the range of second harmonic and has less than 1% transmission for fundamental wave. The blue filter spectrum is shown in Figure 5.5 (b).

Figure 5.5 (a) shows an illustration of the basic parts of the SHG detection setup.

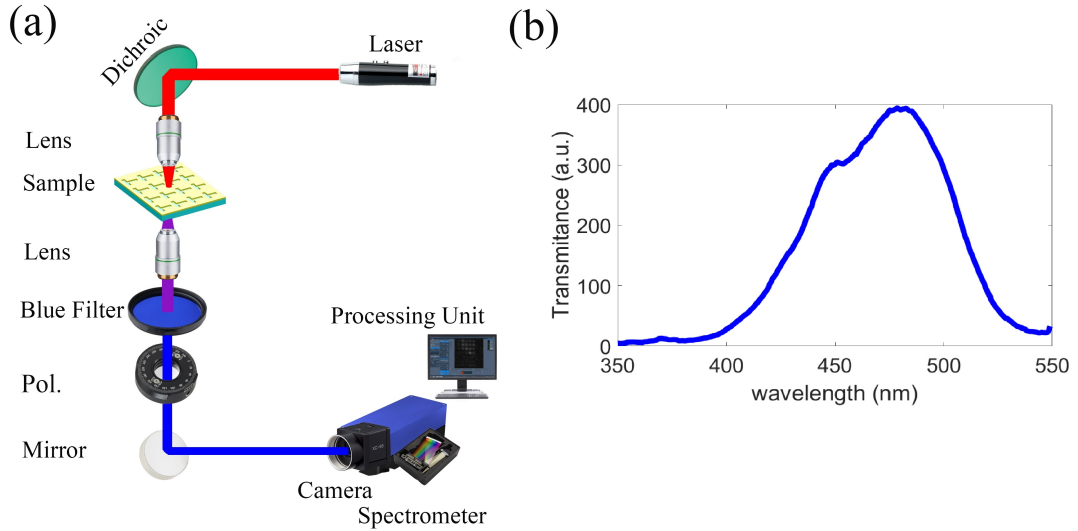


Figure 5.5: a) Simplified schematic of experimental setup. b) Blue filter spectrum

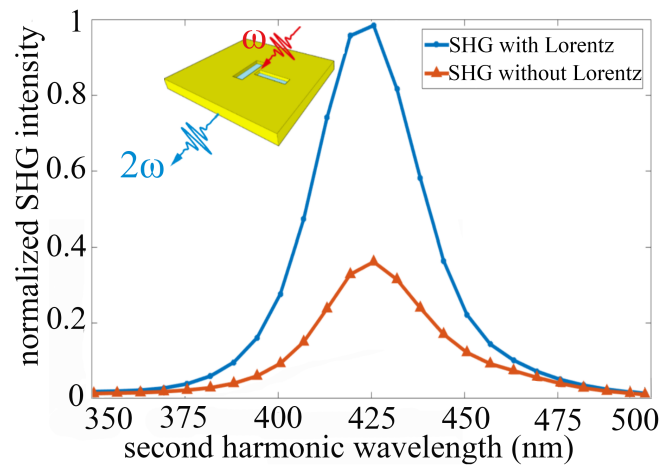
Throughout the experiment, the laser beam is scanning the whole set of T-shaped structures one by one. The beam is focused to a beam waist of  $\sim 400\text{ nm}$ , just big enough to cover one T-shaped structure and small enough to avoid interference with the neighboring structures. The TM polarization of the incident beam was fixed, however, the polarization of detected SHG signal could be ensured by using an analyzer before the spectrometer. By means of this configuration, we were able

to filter out and measure the emission SHG signal at different polarizations. This is important since Lorentz and the two other Hydrodynamic contributions occur at different polarizations. Lastly, the signal was steered toward the spectrometer and CCD camera to be analyzed by the in-site computer.

## Chapter 6

# Results Evaluation, Analysis and Comparison

This chapter presents the results of the published works listed in appendix A. The topics covered include simulation and experimental results of proposed T-shaped aperture, aiming towards maximizing the Lorentz magnetic force term in hydrodynamic theory and also off-normal Lorentz term in circular nanoapertures.



## 6.1 Magnetic Lorentz for Nonlinear Generation

As it was discussed in detail in chapter 3 of this report, the classical theory presents three main bulk contributions to second-order optical nonlinearities in metals: Coulomb, convection, and the Lorentz magnetic force [97]. The investigation of SHG in nanoscale split-ring resonators (SRRs) showed a negligible contribution from the Lorentz magnetic force [98]. This is surprising because these SRRs are well-known for their magnetic response [127, 128]. Here we are investigating whether the Lorentz magnetic force is always weak in metal nanostructures and therefore may be safely neglected.

It is well-known that metal structures typically provide weak magnetic resonances at high frequencies, as described by the Landau-Lifshitz argument but this can be overcome under certain conditions [129]. By analogy, it is worth considering whether the Lorentz force can play a non-negligible (or even dominant) role in SHG.

There is a basic reason why the Lorentz magnetic force is generally weak. It depends on the cross product of the electric and magnetic fields ( $\vec{E} \times \vec{H}$ ). Usually the magnetic and electric fields do not have their maxima in the same spatial location in resonant structures. The simplest example is for cavities formed either by PEC or by PMC mirrors. For the PEC cavity, the transverse magnetic field is maximum at the conductor and the transverse electric field is zero there (Figure 6.1 (a)). For a PMC cavity the situation is reversed (Figure 6.1 (b)). So it appears that the magnetic field and electric field will not be maximized in the same spatial location and so the Lorentz force is usually doomed to be small.

As an example of the calculation of the SHG, based on our developed hydrothermal model and nonlinear scattering theory (details in the chapter 3), let us show the calculation for an SRR, reproducing the parameters from an earlier work [98]. Figure 6.2 (a) shows the SRR under consideration and its dimensions. Figure 6.2 (b) shows the second harmonic conversion efficiency, calculated as a function of the

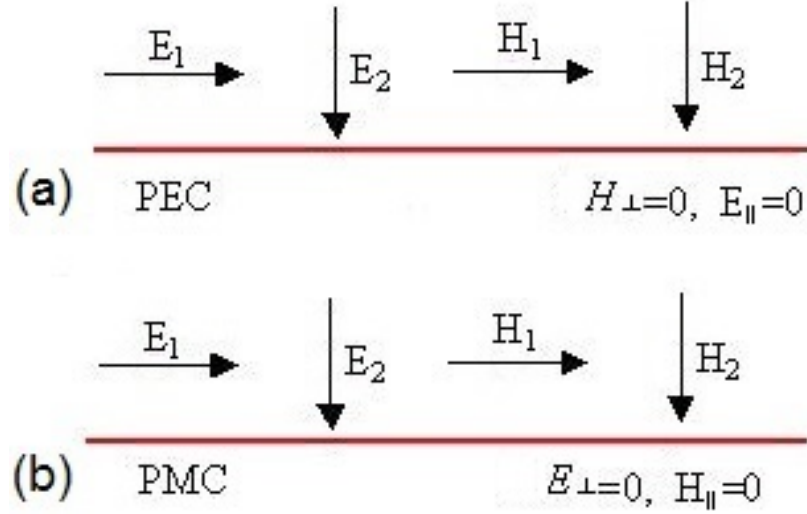


Figure 6.1: Field and boundary conditions in a) PEC and b) PMC.  $\perp$  and  $\parallel$  are denoting the vertical and parallel components of the fields in the wall.

fundamental wavelength,  $\lambda_F$ , with and without the Lorentz force contribution.

As it was mentioned above, that work concluded that the Lorentz force plays a very small (negligible) role in the total SHG. This is also seen in Figure 6.2 (b). For comparison, Figure 6.3 shows the past work results for SHG calculation of the SRR showing that the Lorentz force contribution to the generated SHG field is only marginal ( $\approx 5.5\%$ ). Quantitative agreement is seen between our calculation and the past work [98].

Contrary to the past results, here we demonstrate the design approach to maximize the Lorentz contribution. We also demonstrate in theory and experiment that it surpasses the other contributions. We do this by creating structures that show both magnetic and electric field enhancements in the same spatial location.

As one may expect, these structures are more complicated and they have to be engineered to generate such overlapping fields. In some ways, this is analogous to superscattering of metal nanostructures above the fundamental single-channel limit,

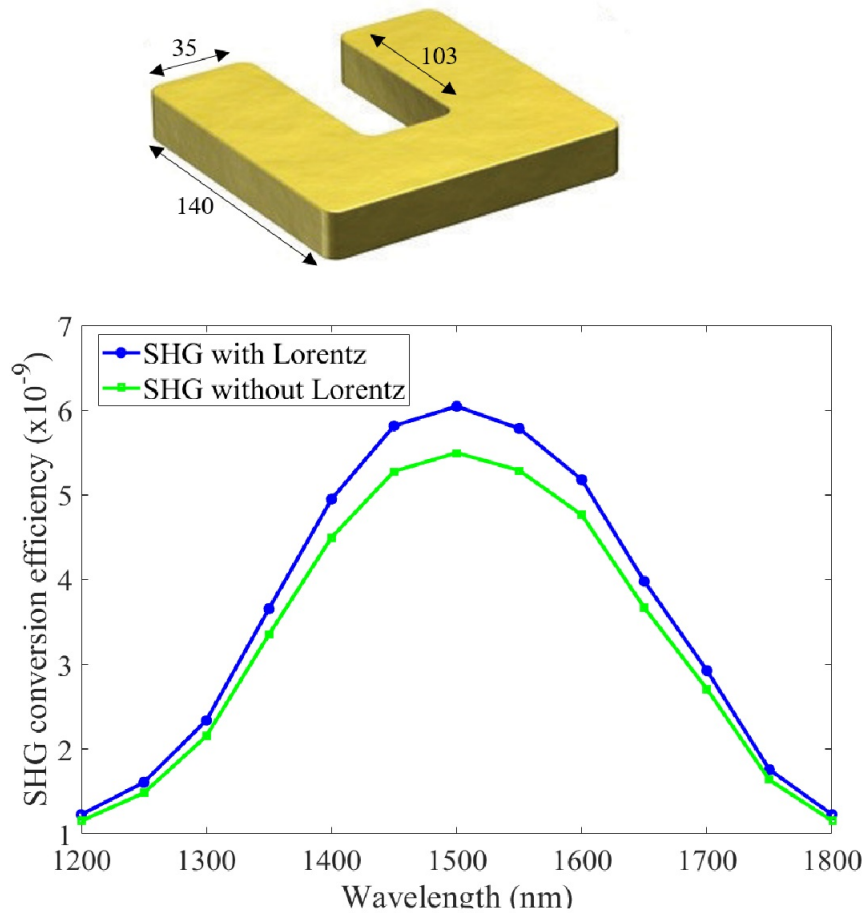


Figure 6.2: Comparison of the second harmonic conversion efficiency with and without Lorentz force contributions for the U-shaped SRR. Schematic of the SRR configuration is depicted with its dimensions based on Ref. [98].

where careful engineering is required to produce overlapping resonances in the same regime of the optical spectrum [130, 131].

Figure 6.4 shows a schematic of the structure under consideration: a T-shaped nanostructure of two non-overlapping rectangular apertures in a 100 *nm* thick gold film on glass.

As it was discussed in chapter 2, by matching the plasmon resonance of metal nanostructures at our wavelength of interest (here: 850 *nm*), it is possible to boost the nonlinear response of the nanostructure. After optimization, the dimensions of

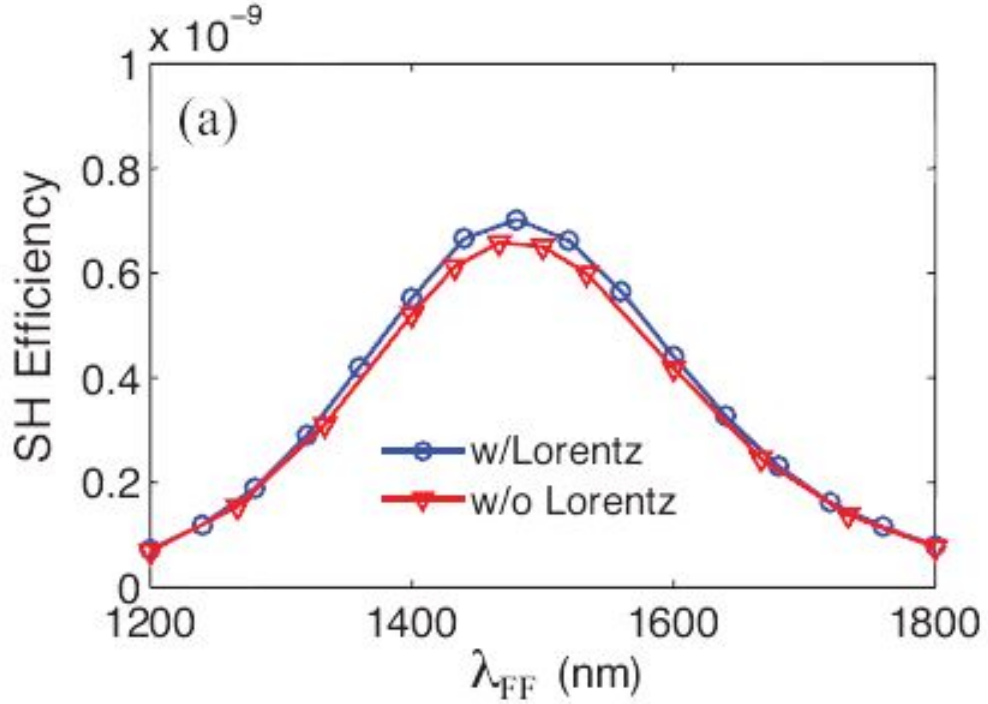


Figure 6.3: The past work results for comparison of the second harmonic conversion efficiency with and without Lorentz force contributions for the U-shaped SRR [98].

the horizontal and vertical rectangle are set at  $L=240 \text{ nm}$ ,  $W=50 \text{ nm}$ . They are separated by the gap of  $G=50 \text{ nm}$ . This geometry is designed to give a plasmonic resonance at  $850 \text{ nm}$ . The linear response of this structure is shown in Figure 6.5.

The two apertures are chosen as a rudimentary basis where one aperture will provide a maximum electric field, and the other aperture will provide a maximum magnetic field in the gold region between the apertures. In this way, both the magnetic and electric fields are maximized in the same spatial location and at the same resonance frequency.

The FDTD simulations were used to calculate the field distributions in the apertures. Figure 6.6 (a) shows a schematic top view of the T-shaped structure and Figure 6.6 (b-e) show the electric and the magnetic field distributions of the sample



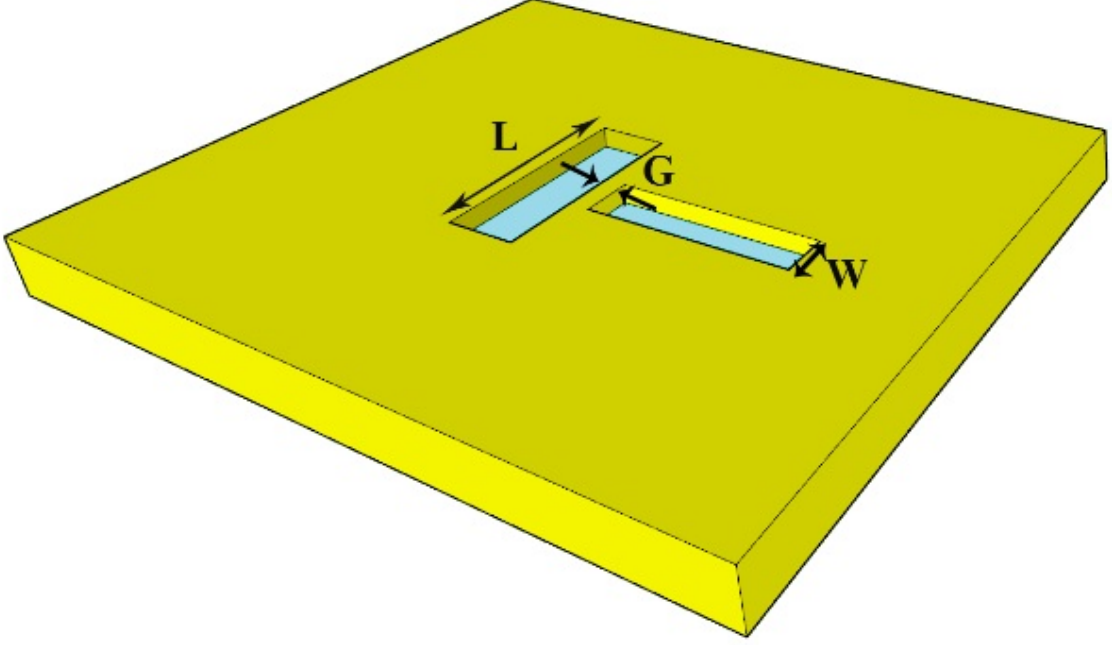


Figure 6.4: Schematic of the proposed T-shaped structure and its dimensions.  $L$  shows the length of apertures,  $W$  width and  $G$ , the separation gap between two horizontal and vertical apertures.

structure. Each rectangle has maximum electric fields along its long edge and maximum magnetic fields at the sides. For  $45^\circ$  excitation then, it is possible to excite both apertures and create maximum  $\vec{E} \times \vec{H}$  in the gold film, as shown in Figure 6.6 (f). There are also hydrodynamic components that are not shown here. The details of the simulation are found in the Simulation Details Chapter.

The FDTD method was used to solve field distributions at the fundamental and harmonic wavelengths. SHG was then calculated using Equation 3.41. Several aperture dimensions were simulated to optimize the SHG intensity.

Figure 6.7 shows the NLS theory calculation of the SHG for the proposed T-shaped structure above.

From Figure 6.7 it is clear that the Lorentz contribution dominates the overall SHG, being 65% larger than the sum of the other two contributing terms.

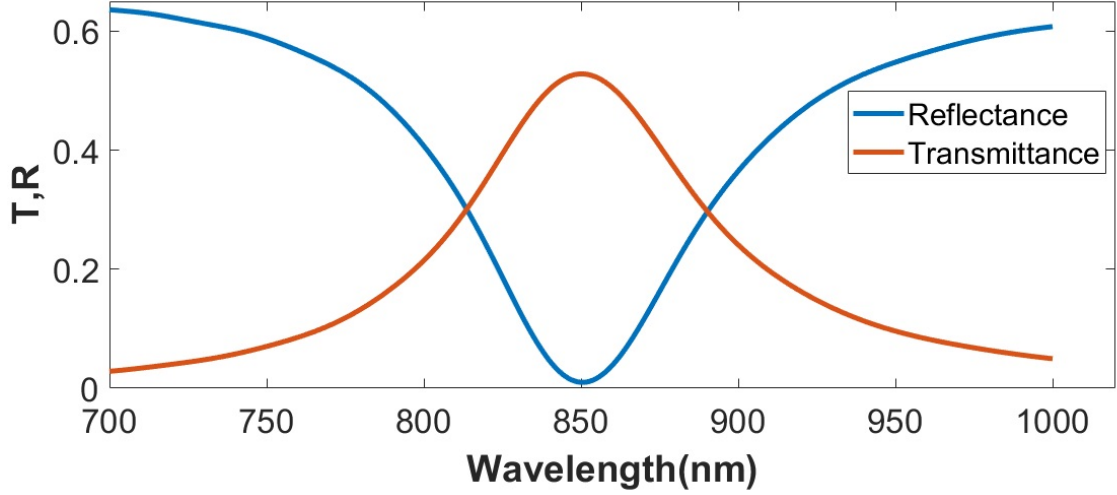


Figure 6.5: Transmittance and reflectance spectrum of the designed structure showing resonance at  $850\text{ nm}$  ( $L=240\text{ nm}$ ,  $W=50\text{ nm}$  and  $G=50\text{ nm}$ )

Another signature of this dominant Lorentz response is found by varying the incident polarization. While the Lorentz response is maximized for  $45^\circ$  excitation, the convection contributions are maximized for either  $0^\circ$  or  $90^\circ$  (See Figure 6.8). We investigate a range of incident polarization angles and dimensions in Figures 6.9 (a) and (b). The SHG is presented in normalized units.

Although in nanostructures below  $100\text{ nm}$ , as considered here, the bulk response has been suggested to dominate [132], the surface response has also shown to have effects on SHG for flat films [66] and large nanoparticles [71]. We have calculated this response and performed the FDTD simulations considering just the surface effect based on equation 3.29. Figure 6.10 shows the simulated SHG response due to surface effects. As it can be seen, the SHG surface contribution is maximized for  $0^\circ$  incident polarization.

As a result of Figure 6.10, one can conclude that the off-axis polarization maximum found in the theory (later also seen in the experiments) does not coincide with a surface response. We have shown that the normal surface contribution does not

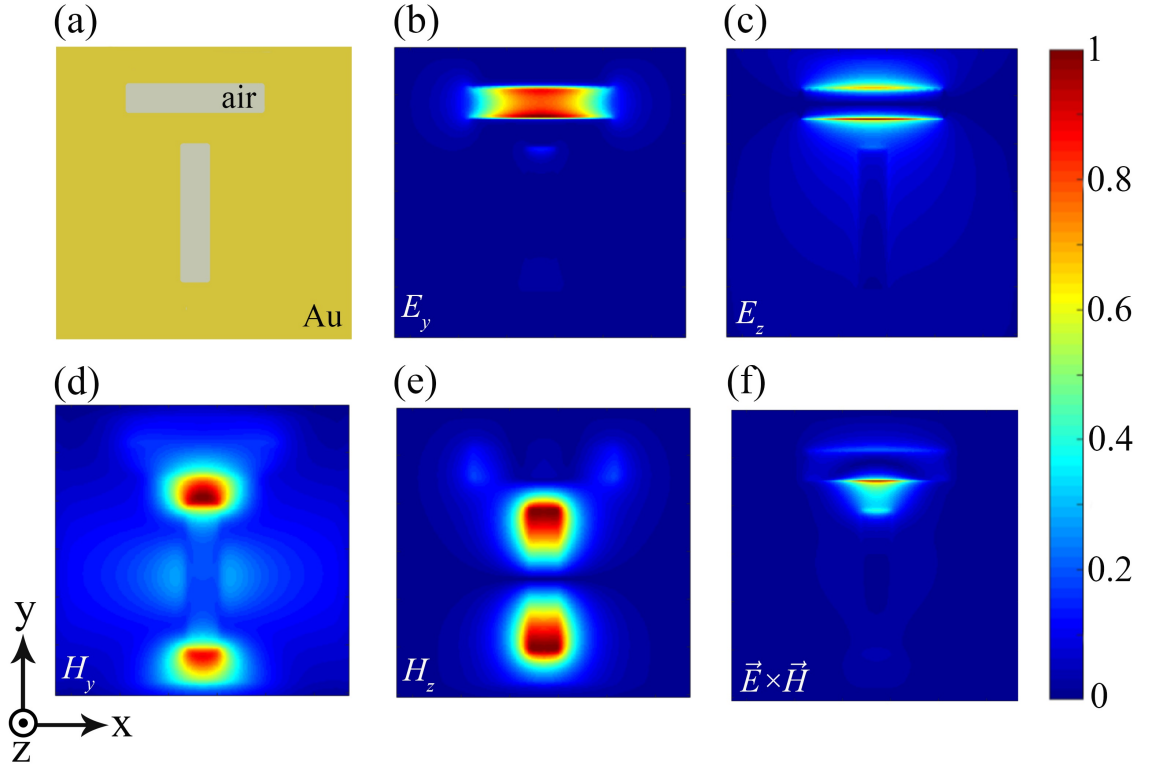


Figure 6.6: a) Top view schematic of T-shaped structure (gold on glass). Simulated field intensity for b) the  $y$  component of  $\vec{E}$ , c) the  $z$  component of  $\vec{E}$ , d) the  $y$  component of  $\vec{H}$  and e) the  $z$  component of  $\vec{H}$ . f) The Lorentz magnetic force contribution to the nonlinear source current proportional to  $\vec{E} \times \vec{H}$ .

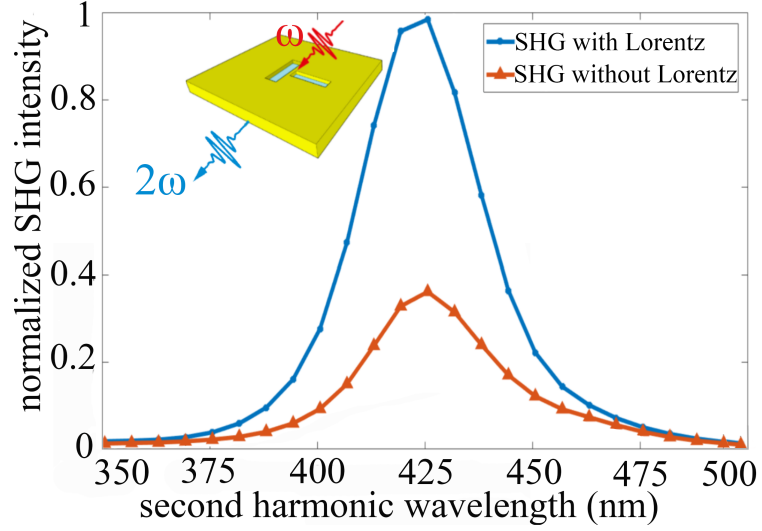


Figure 6.7: Lorentz magnetic force dominates SHG at the resonance of T-shaped aperture (same dimensions as described previously).

contribute a  $45^\circ$  response (by symmetry and calculations). The tangential components of the effective nonlinear surface response result from the bulk only, and these are represented by the hydrodynamic model presented before.

However, it is interesting to note that past works have looked at the similarities of bulk and surface responses in media with inversion symmetry [133], and suggested that in nanostructures with multiple beams distinguishability may be found once again [66]. This points to an interesting area for further investigation where the distinguishability of different components in nanostructures made from materials with inversion symmetry.

It is also worth noting that for a centrosymmetric material, the tangential contributions to the nonlinear surface response vanish, and therefore only the normal surface contribution is retained.

Finally Figure 6.11 shows the DC current density map for  $45^\circ$  and  $135^\circ$  incident beam polarization. At  $45^\circ$  the surface currents components are directed towards a negative  $x$  axis, however, at  $135^\circ$  the direction is reversed. As a result, by exciting

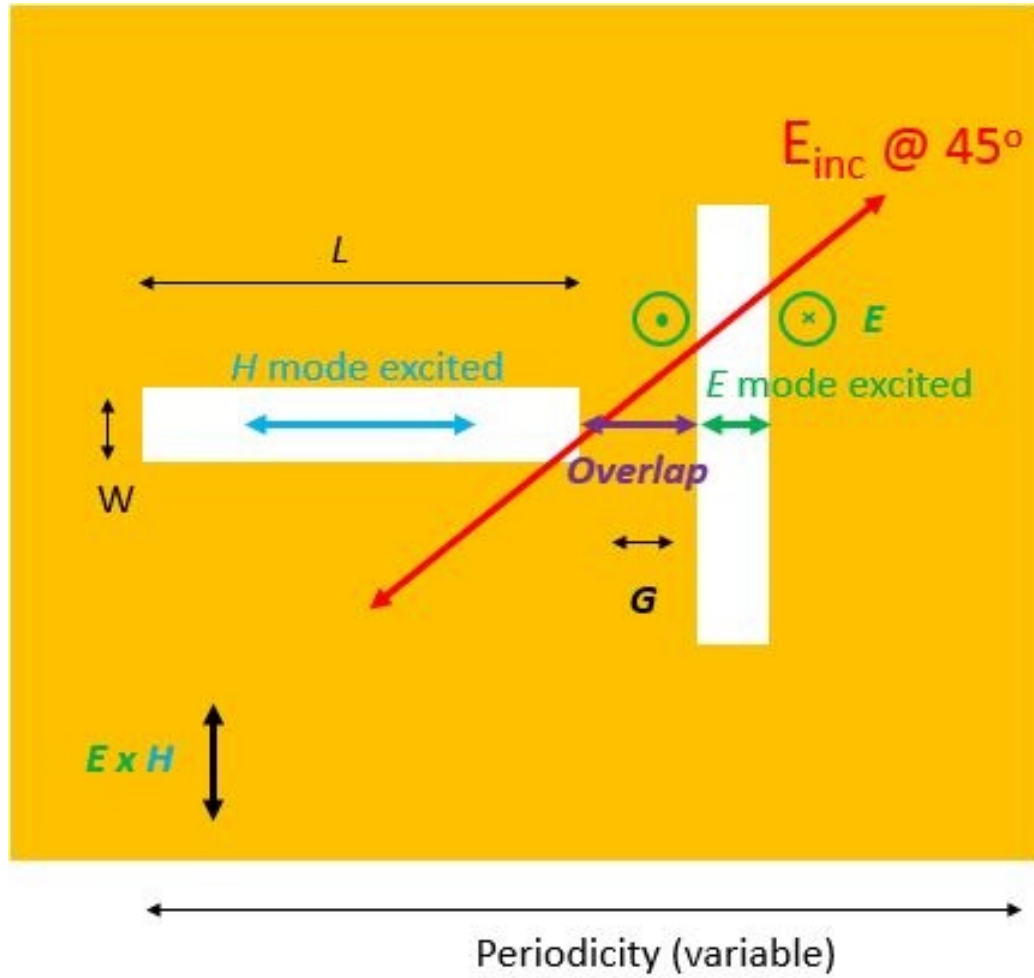


Figure 6.8: Incident EM field at  $45^\circ$  polarization results in horizontal polarized generated Lorentz magnetic force field.

the T-shaped structure with two incident beams with a  $90^\circ$  difference in polarization angle, the DC current can be accessed. This DC current can be used for ultrafast (THz) current generation.

### 6.1.1 SHG Experimental Results of T-shaped Apertures

Figure 6.12 (a) shows the schematic of the fabricated structures. They were fabricated with varying dimensions and orientation to probe the resonance and different polarizations of excitation light. Figure 6.12 (b) shows a scanning electron microscope

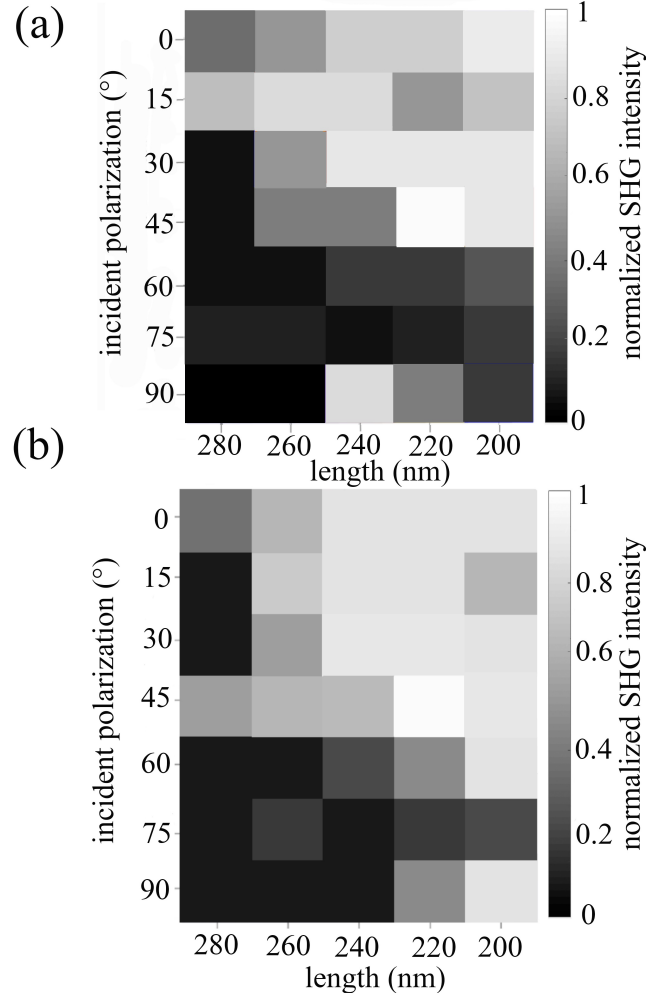


Figure 6.9: Color map of calculated SHG intensity for different aperture length and incident polarizations, for a) total SHG, results from equation 3.19b, and b) considering only the Lorentz magnetic contribution to the SHG.

image of the fabricated structure.

The experimental results of measured SHG are presented in Figure 6.12 (c) and (d). The incident polarization is kept fixed, horizontal (along the  $x$  axis), so rotating the structure is equivalent to rotating the incident polarization.

Figure 6.12 (c) shows total SHG in transmission mode. Figure 6.12 (d), shows the polarization dependence characterization of the sample array. we have added a polarizer after the sample array and before the detector to isolate the  $45^\circ$  SHG

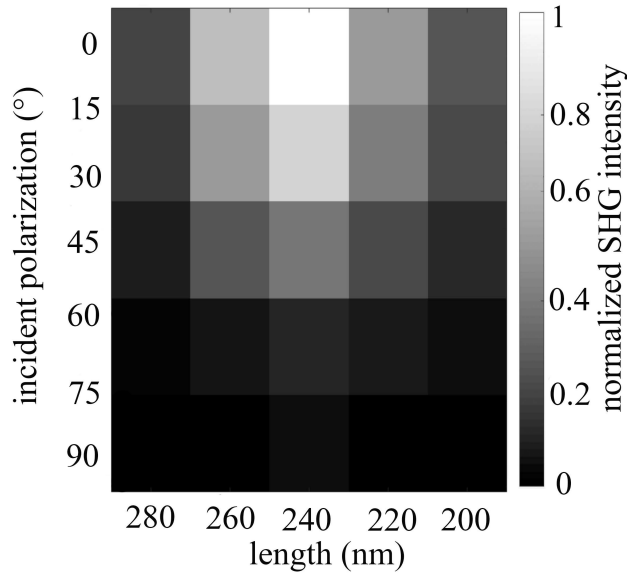


Figure 6.10: Simulation of the SHG signal expected from the surface contribution.

corresponding to the Lorentz magnetic contribution.

The maximum SHG is measured for  $45^\circ$  (or equivalently  $45^\circ$  incident light polarization) rotation and  $L=220 \text{ nm}$ .

In a different experimental setup constructed to examine the polarization from the Lorentz magnetic force contribution in comparison to the two other hydrodynamic ones in terms of generation polarization, the polarization analyzer after the sample was set at 5 different polarization angles. The results in Figure 6.13 again prove that the highest SHG intensity occurs at  $45^\circ$  which corresponds to the maximum for the Lorentz force contribution.

Figure 6.14 (a) illustrates the captured SHG images of the fabricated structures at different detection wavelengths varied from  $400 \text{ nm}$  to  $450 \text{ nm}$ . By comparison, the image captured at the second harmonic wavelength ( $\sim 425 \text{ nm}$ ). The data shows a significantly higher intensity, due to a maximum in the SHG signal here. Figure 6.14 (b) is the spectrum of detected signals for the same wavelength range.

Comparing Figures 6.9 (b) and (c) with Figures 6.12 (c) and (d), good agreement

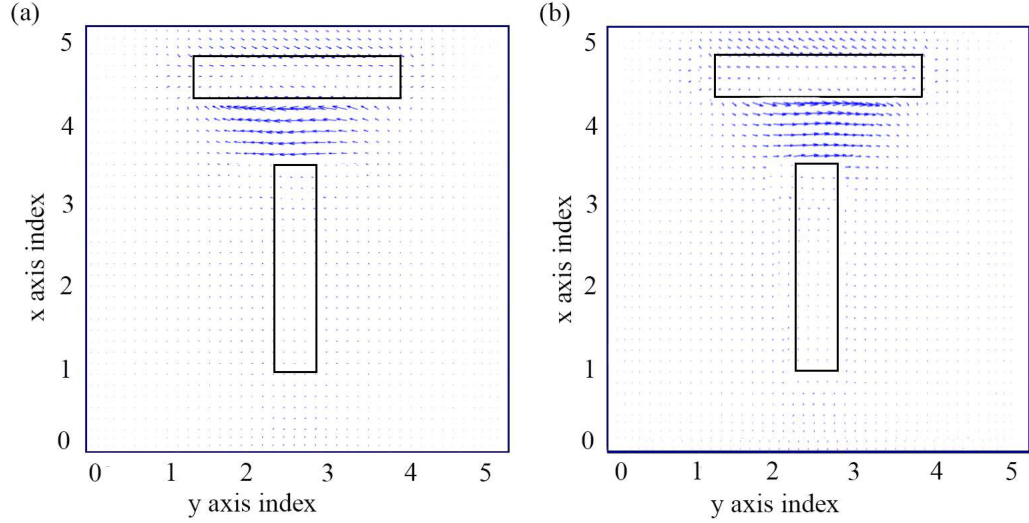


Figure 6.11: DC current density map for a) 45° and b) 135° incident beam polarization.

between the theory and experiment is achieved. The experimental maximum SHG was for 240 *nm* length and 30° polarization, close to the theoretical maximum of 220 *nm* and 45° polarization. Discrepancies between the results can be attributed to fabrication tolerances (around 10 *nm* tolerance on the focused ion beam milling, with tapering, as well as alignment of the sample within the microscope).

We measured the output SHG with a power meter placed in front of the detector. For 20 *mW* average incident power, the output power is 146  $\mu W$ , which gives a detected conversion efficiency of 0.73%. Considering the material damage for the proposed structure (as it was mentioned in section 2.3: 10 *mW*/ $\mu m^2$  for 100 *nm* gold thin layer) and the laser beam waist of 400 *nm*, the highest expected SHG efficiency can be achieved at 1.1%.

Even though we are still far away from 10% conversion efficiency which is our ultimate goal for real applications, there are still some ideas that could get us closer to achieving this goal. Using apertures prevents the sample from overheating by having a good conducting layer [134, 135]. Therefore, we could benefit from a higher power



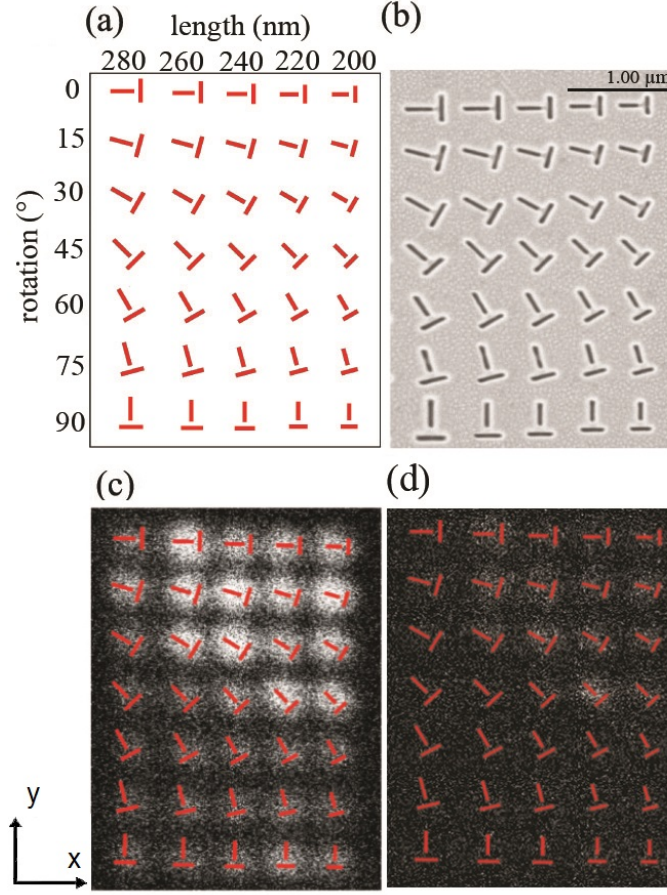


Figure 6.12: a) T-shaped apertures of different sizes and orientations. b) Scanning electron image of fabricated apertures on a gold film. c) SHG measured in transmission mode shows the highest response for  $45^\circ$  aperture, indicating that the Lorentz force is the prominent contribution. d) A  $45^\circ$  analyzer further confirms the dominant role of the Lorentz force in SHG.

pulsed laser to boost conversion efficiency without suffering from melting. Moreover, confining light in a very small gap can increase the power further and contribute to increasing SHG. By using new fabrication techniques such as He beam milling [136], atomic layer deposition [137], shadow mask lithography [138], and template stripping [139], a gap size below  $10\text{ nm}$  should be achievable.

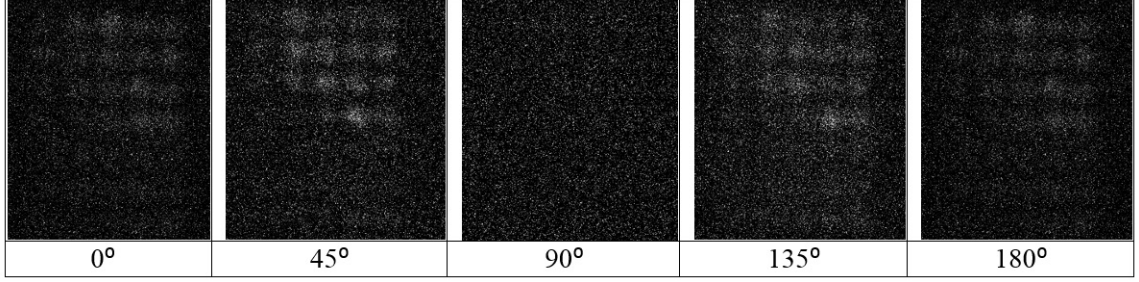


Figure 6.13: Captured images of the fabricated structures at different polarizations showing detected SHG signal as white spots.

## 6.2 Angled Lorentz Contribution

The relative importance of various hydrodynamic contributions to SHG has been a topic of investigation for at least four decades [97]. There is some debate about how to disentangle various contributions in practice [66, 97],

Besides our proposed T-shaped aperture, aiming towards a dominate Lorentz contribution, it is interesting to consider if there are more natural ways to achieve an enhanced Lorentz contribution.

It was shown in chapter 2 based on Bethe’s law that subwavelength apertures in thin metal films can be treated as magnetic dipoles [15], and hence the transmission scales as the fourth power of the aperture dimension. In addition, there is an electric dipole component that arises when an out-of-plane electric field is presented at the aperture [15]. This only occurs for angled incidence and so it is less commonly considered. Nevertheless, this normal contribution is important because it allows for simultaneous electric and magnetic dipoles in the same spatial location. Here, the cross product of these two effective dipoles is considered as a Lorentz contribution to SHG.

Among a considerable number of works on SHG from apertures [20–23, 60, 63, 99, 140–154], there are works that are looking at angled contributions in ordered and disordered apertures [23, 63]. For the disordered case, it is anticipated that there

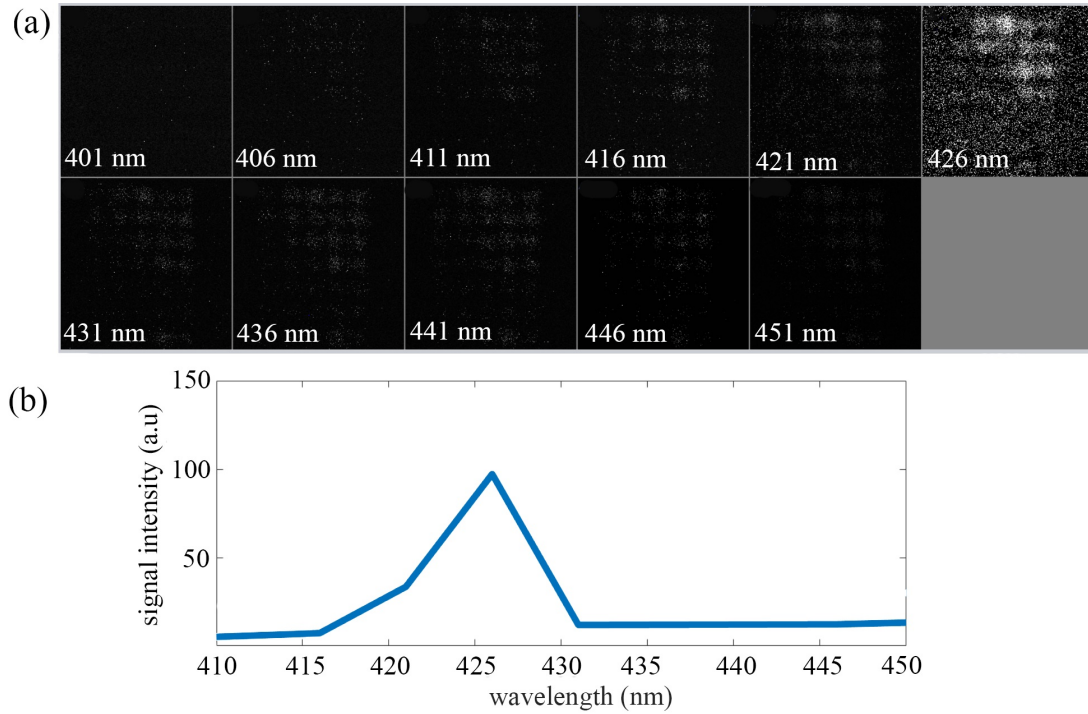


Figure 6.14: a) Captured images of the fabricated structures at different detection wavelengths varied from 400  $nm$  to 450  $nm$  representing detected SHG signal as white spots. Showing a significant high intensity at second harmonic wavelength ( $\sim 425$   $nm$ ). b) The spectrum of detected signal for the same wavelength range.

is negligible contribution coming from aperture interactions and so the response is similar to a single aperture [155]. The quantitative finding of past works was that the SHG was enhanced for an angle of  $50^\circ$  [63]. Figure 6.15 shows the past work SHG results along with an SEM of their investigated apertures.

As their field simulation results in Figure 6.16 shows, the field is highest at one edge where there was the largest enhancement to the SHG.

While this is a reasonable explanation, the relative physical origin of this SHG from the various hydrodynamic effects (separate from surface contributions) deserves further consideration.

Here, we analyze the properties of a circular nanoaperture in a thin gold film metasurface and investigate the origin of the generated second harmonic light. The

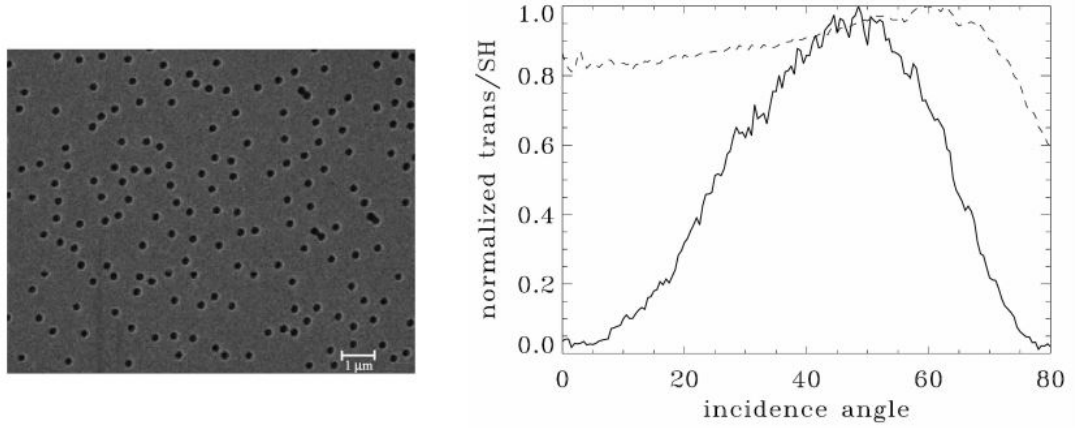


Figure 6.15: SEM image of disordered array of circular apertures along with a plot of fundamental transmission (dashed linestyle) and SH signal (solid linestyle) as a function of incidence angle of the past work. The apertures are roughly  $235\text{ nm}$  by  $241\text{ nm}$  in size. Both curves are normalized to their maximum values [63].

investigated nanoaperture is identical to the past experiments [63], a  $260\text{ nm}$  diameter aperture in a  $100\text{ nm}$  thick gold film on a quartz substrate with a  $5\text{ nm}$  Chromium adhesion layer in between.

FDTD was used to calculate the linear solutions to Maxwell's equations required for the theory of section 3.5.

The TFSF sources propagating along the  $z$ -axis illuminate the structure at varying incident angles to their normal axis with the P-polarized input field.

First, the transmission of fundamental light at different incident angles on the metal film was simulated. Figure 6.17 shows the simulation result along with a digitized depiction of the experimental result presented in Figure 6.15 from Ref. [63] for comparison. A  $\cos\theta$  factor is required to account for the reduced subtended area at angled detection. The FDTD simulation curve is normalized to unity power.

Second, each SHG hydrodynamic contribution term as a function of the incident angle was calculated. The total SHG was then calculated as the sum of all three contributions. Figure 6.18 shows the result of SHG calculations along with the SHG

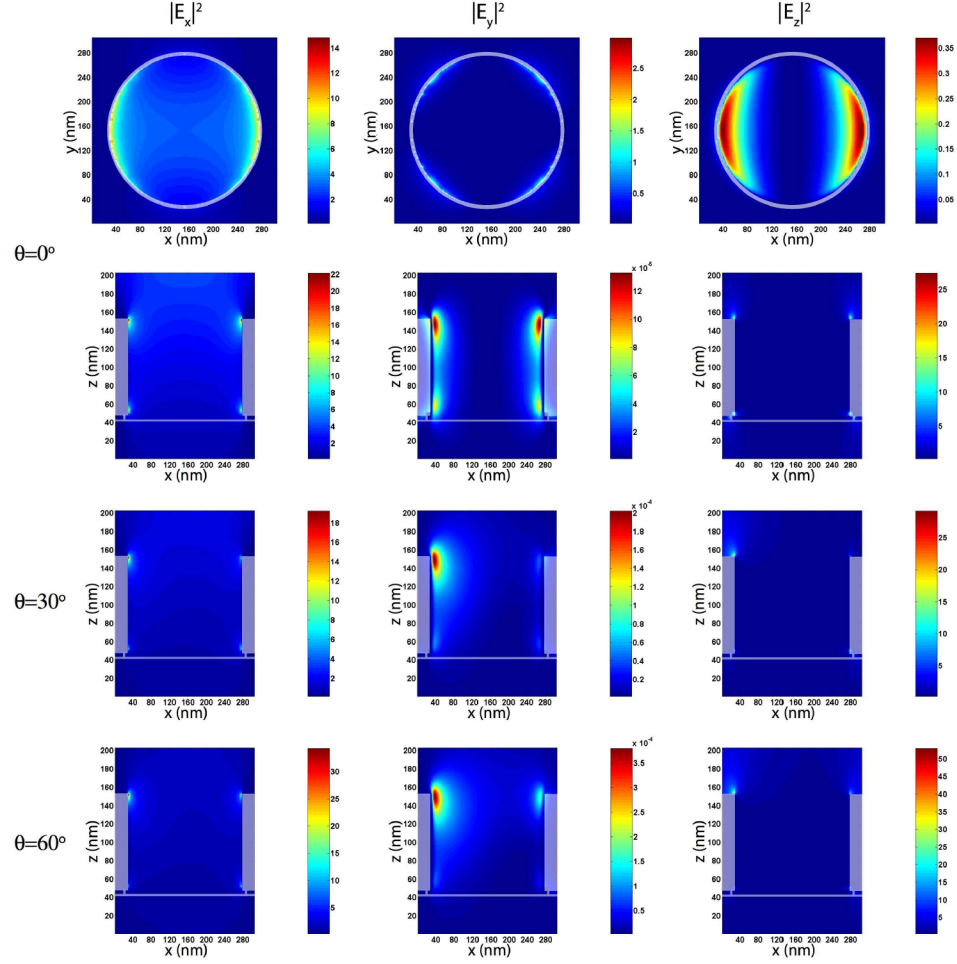


Figure 6.16: Calculated field intensity distribution of the 260 *nm* diameter aperture in 100 *nm* thick gold film under normal and two different angles of incident illumination, at 800 *nm* of the past work [63].

experimental result of the past work [63].

The simulated linear transmission and NLS theory results match well with the past experiment [63].

For normal incidence, the harmonic generation has no Lorentz contribution. This is expected from Bethe's aperture theory since there is no electric dipole for normal incidence. As the incidence angle is increased, however, the Lorentz contribution becomes the dominant term and indeed the maximum of the Lorentz SHG coincides with the experimentally determined value. The Lorentz contribution is an order of

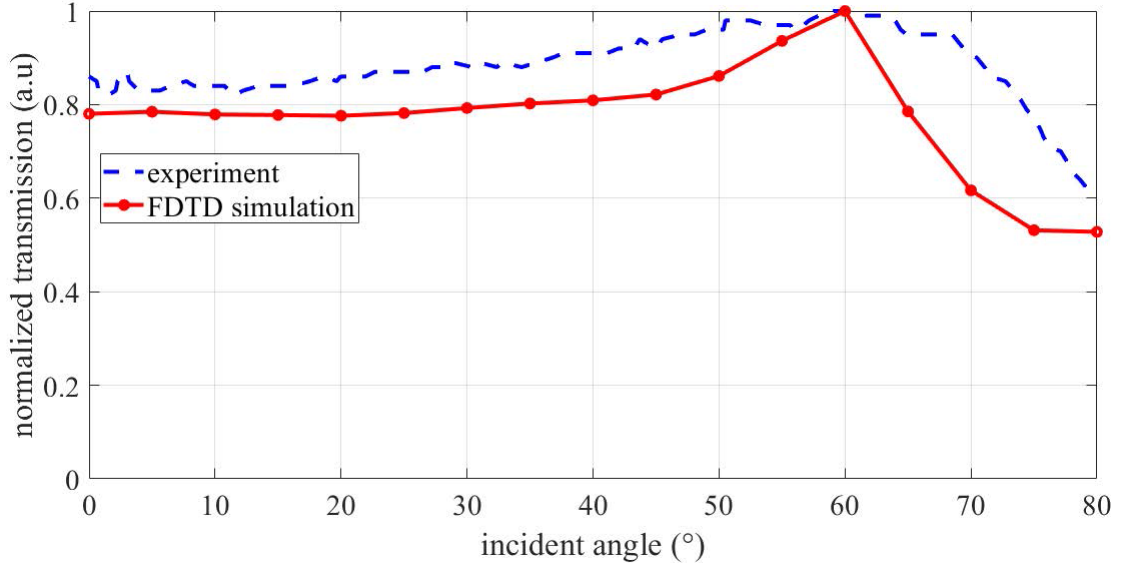


Figure 6.17: The FDTD simulation of the transmittance spectrum of the fundamental beam through the circular unit cell as a function of incidence angle, along with a digitized plot of the past experimental result of the same structure in Ref. [63]. Both curves are normalized to their maximum values.

magnitude larger than the other contributions at the angle of its maximum.

The angular dependence of the Lorentz contribution follows the force on a magnetic dipole from the electric dipole, considering the effective dipoles of the aperture. In particular, the magnetic dipole has no angular dependence, whereas electric dipole has a  $\sin(\theta)$  dependence. The detected field should also account for Lambert's cosine law to account for the reduced subtended area with an increasing angle.

So overall, the cross product of these two fields will produce a detected intensity which goes as  $\sin^2(\theta) \cos^2(\theta)$ . This dependence is also plotted in Figure 6.18. It is clear that this simple theoretical model agrees well with the experimental and comprehensive NLS theory results.

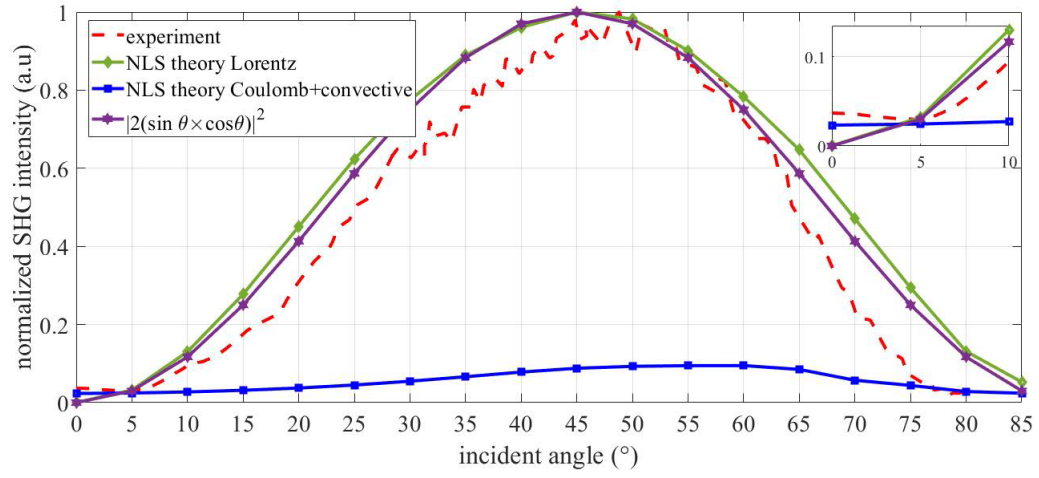
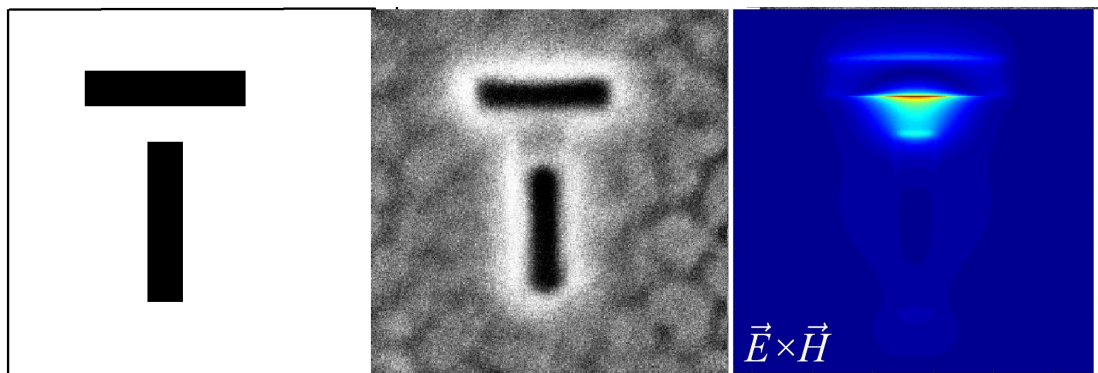


Figure 6.18: SHG calculation based on NLS theory as a function of incident angle for Lorentz, the sum of two Coulomb and convective terms, and  $|\sin \theta \times \cos \theta|^2$ ; along with the digitized plot of the corresponding experimental SHG results in Ref [63]. The inset shows the curves plotted for small angles. The curves are normalized to their maximum value of total SHG.

## Chapter 7

# Conclusion and Outlook

This chapter summarizes the findings from the research detailed in the thesis and provides an outlook on the future of nonlinear plasmonic metasurface research.





The SHG from a non-centrosymmetric nanostructure in gold film was studied comprehensively in this thesis. As a result of the work carried out, structures with dominant Lorentz magnetic contribution to the SHG were designed and validated. The primary design principle focused on maximizing the electric and magnetic field components at the same spatial location. A revised theoretical model was developed based on the hydrodynamic Drude model and nonlinear scattering theory. A good agreement with experimental measurements, confirming the role of the Lorentz magnetic response in the SHG, was observed.

Past work on SRRs has shown a Lorentz contribution of 5.5% to the overall second harmonic generation [98]. The results in this thesis show that through the design of T-shaped apertures, a dominant Lorentz contribution of 65% can be achieved. The dominant Lorentz contribution is also found by varying the incident polarization. While the convection contributions are maximized for either  $0^\circ$  or  $90^\circ$ , the Lorentz response is maximized for  $45^\circ$  excitation.

Careful design of the nanostructured metasurfaces shows a dramatic change in the optical properties. High efficiency of wavelength conversion is achieved from a single ultrathin layer (0.75%). The proposed structure in the thesis uses a connected metal film that can quickly dissipate heat from the hot-spot regions and is able to overcome the fundamental melting limit to nonlinear conversion. The structures can withstand significantly larger incident powers than isolated nanoparticles. Since the conversion efficiency scales linearly with the incident field, higher conversion efficiencies are possible with the described approach. Additionally, sharp features more prone to melting and smoothing (reflow) upon strong excitation are omitted in the proposed design.

Saturation of the nonlinear response and higher-order nonlinear processes limits the efficiency of SHG conversion. The Lorentz magnetic contribution to SHG results from a small region of the entire structure. This is the metal interconnect separating

the horizontal and vertical apertures and acts as the overlapping region for the electric and magnetic fields generated upon excitation. In the proposed structure, it is the 50 nm gold bridge between the two rectangles. Therefore, it is envisioned that greater Lorentz enhancement can be achieved by designing structures with larger overlapping regions or even multiple overlapping regions.

Another prominent result in the thesis focuses on the dominant Lorentz contribution for the SHG from a circular aperture in a metal film at angled incidence. As per Bethe's aperture theory, the observed behavior was resolved into the electric and magnetic field components. Considering the force on a magnetic dipole from an electric dipole, it was shown that the Lorentz contribution in this case arises from the cross product of the two dipoles. The FDTD simulation results show that the Lorentz contribution of the circular structure is 12 times larger than the combined convective and Coulomb contributions.

Future continuing research could evaluate the enhancement in SHG from nanostructured metal films by combining angular enhancements with the design of the aperture to achieve higher power or conversion efficiencies using promising noble metals. Melentiev et al. [134] have shown that a single nanoslit in aluminum displays a higher conversion efficiency, three orders of magnitude greater than gold. In addition, consideration should be made for Lorentz, Coulomb, and convective contributions to interfere constructively for optimal conversion efficiency. Ideally, maximizing all contributions, conversion efficiencies of nonlinear plasmonic metasurfaces will be able to exceed 10%.

A future application of the nonlinear plasmonic metasurface discussed in this thesis can be extended to THz current generation. The Lorentz magnetic response enables both second harmonic (sum frequency) and DC (difference frequency) currents to be generated. Therefore, a modified version of the proposed structure may be used to

generate THz current that can then be coupled to an antenna for transmission. Other works have noted the potential of THz generation from the Lorentz response [156,157]. However, the work in this thesis demonstrates a structure that can maximize both the magnetic and electric field in the same spatial location, thereby maximizing the Lorentz magnetic contribution to the driving current.

The potential for the applications of the nonlinear plasmonic metasurfaces discussed in this thesis are immense and the field of research is expected to become increasingly critical to development of the future nanophotonic devices [158].

# Appendix A

## Publications

1. Rahimi, Esmaeil, and Reuven Gordon. Nonlinear plasmonic metasurfaces. *Advanced Optical Materials* 6, no. 18 (2018): 1800274.
2. Rahimi, Esmaeil, Haitian Xu, Byoung-Chul Choi, and Reuven Gordon. Lorentz nanoplasmonics for nonlinear generation. *Nano letters* 18, no. 12 (2018): 8030-8034.
3. Rahimi, Esmaeil, and Reuven Gordon. A new angle on second harmonic generation. *Plasmonics*, 2020 (submitted).
4. Rahimi, Esmaeil J., Haitian Xu, Byoung-Chul Choi, and Reuven Gordon. Nonlinear plasmonic metasurfaces: focusing on the Lorentz contribution (Conference Presentation). In *Metamaterials, Metadevices, and Metasystems 2018*, vol. 10719, p. 107191L. International Society for Optics and Photonics, 2018.
5. Rahimi, Esmaeil, Reuven Gordon, Haitian Xu, and Byoung-Chul Choi. Lorentz Based Metamaterials for Nonlinear Generation. In *2018 IEEE 13th Nanotechnology Materials and Devices Conference (NMDC)*, pp. 1-4. IEEE, 2018.

6. Xiang, Dao, Ghazal Hajisalem, Esmaeil Rahimi, and Reuven Gordon. Functional Quantum-Plasmonic Metamaterials/Metasurfaces and Maximizing the Lorentz Nonlinearity. In CLEO: QELS Fundamental Science, pp. FTu4E-3. Optical Society of America, 2018

## Appendix B

### Matlab Script

---

```

% SHG calculation script
%%-----

    %Constants define
clc
clear all
close all
format shortE
load("Ex850theta0.mat");
[dx,dy,dz]=size(Ex850)
clear Ex850;

load("x.mat")
load("y.mat")
load("z.mat")

    %based on mesh size;
deltax=5e-9;
deltay=5e-9;
deltaz=5e-9;

    %SI parameters
c0=3e8;           %m/s
gama=1.07e14;     %1/s
q=-1.6e-19;       %q=-e=-1.6e-19
mio=1.256e-6;     %Tm/A
Ne=5.7e22;        %m^-3 smith mentioned Ne=5.9e28
m=9.11e-31;       %Kg

wl=850e-9;
w=(2*pi*c0)/(wl);
R=(1i*Ne*(q^3))/((m^2)*(w+1i*gama)*(2*w+1i*gama));

theta=[0,10,20,30,40,50,60,70,80];
%%

for i=1:length(theta)
    disp("theta"+num2str(theta(i)))
    load("Ex850theta"+num2str(theta(i))+".mat");
    load("Ey850theta"+num2str(theta(i))+".mat");

```

---

```

load("Ez850theta"+num2str(theta(i))+".mat");
load("Hx850theta"+num2str(theta(i))+".mat");
load("Hy850theta"+num2str(theta(i))+".mat");
load("Hz850theta"+num2str(theta(i))+".mat");
load("Ex425.mat","Ex425")
load("Ey425.mat","Ey425")
load("Ez425.mat","Ez425")
load("index_850theta"+num2str(theta(i))+".mat");

uni=unique(index_850);

    %Based on Lumerical library fof used materials
nx=uni(3);

    %Integral initial values
LI=0;
KI=0;
CI=0;

    %differential calculation definitions
Exx=diff(Ex850,1,1)/deltax;
Eyx=diff(Ey850,1,1)/deltax;
Ezx=diff(Ez850,1,1)/deltax;
Exy=diff(Ex850,1,2)/deltay;
Eyy=diff(Ey850,1,2)/deltay;
Ezy=diff(Ez850,1,2)/deltay;
Exz=diff(Ex850,1,3)/deltaz;
Eyz=diff(Ey850,1,3)/deltaz;
Ezz=diff(Ez850,1,3)/deltaz;

    % show size
sizeExx=size(Exx)
sizeExy=size(Exy)
sizeExz=size(Exz)
sizeEyx=size(Eyx)
sizeEyy=size(Eyy)
sizeEyz=size(Eyz)
sizeEzx=size(Ezx)
sizeEzy=size(Ezy)
sizeEzz=size(Ezz)

```



---

```

SizeEx850=size(Ex850)
SizeEy850=size(Ey850);
SizeEz850=size(Ez850);
SizeHx850=size(Hx850);
SizeHy850=size(Hy850);
SizeHz850=size(Hz850);
SizeEx425=size(Ex425);
SizeEy425=size(Ey425);
SizeEz425=size(Ez425);
Sizeindex=size(index_850)

if (Sizeindex==SizeEx850)&(SizeEy850==SizeEy850)&(SizeEz850==SizeHx850)&
    (SizeHy850==SizeHz850)&(SizeEx425==SizeEy425)
    disp("OK")
else
    disp("Error")
end
disp("_____")

Exz=Exz(1:dx-1,1:dy-1,:);
Eyz=Eyz(1:dx-1,1:dy-1,:);
Exx=Exx(:,1:dy-1,1:dz-1);
Eyx=Eyx(:,1:dy-1,1:dz-1);
Ezx=Ezx(:,1:dy-1,1:dz-1);
Exy=Exy(1:dx-1,:,1:dz-1);
Eyy=Eyy(1:dx-1,:,1:dz-1);
Ezy=Ezy(1:dx-1,:,1:dz-1);
Ezz=Ezz(1:dx-1,1:dy-1,:);
Ex850=Ex850(1:dx-1,1:dy-1,1:dz-1);
Ey850=Ey850(1:dx-1,1:dy-1,1:dz-1);
Ez850=Ez850(1:dx-1,1:dy-1,1:dz-1);
Ex425=Ex425(1:dx-1,1:dy-1,1:dz-1);
Ey425=Ey425(1:dx-1,1:dy-1,1:dz-1);
Ez425=Ez425(1:dx-1,1:dy-1,1:dz-1);
Hx850=Hx850(1:dx-1,1:dy-1,1:dz-1);
Hy850=Hy850(1:dx-1,1:dy-1,1:dz-1);
Hz850=Hz850(1:dx-1,1:dy-1,1:dz-1);
index_850=index_850(1:dx-1,1:dy-1,1:dz-1);

    %Defining parameters inside each integral terms; K stands ✓
for
```

---

```

        %coulomb and C stands for convective terms
KEx850=Ex850.*(Exx+Eyy+Ezz);
KEy850=Ey850.*(Exx+Eyy+Ezz);
KEz850=Ez850.*(Exx+Eyy+Ezz);
CEx850=(Ex850.*Exx)+(Ey850.*Exy)+(Ez850.*Exz)+(Exx+Eyy+Ezz).*Ex850;
CEy850=(Ex850.*Eyx)+(Ey850.*Eyy)+(Ez850.*Eyz)+(Exx+Eyy+Ezz).*Ey850;
CEz850=(Ex850.*Ezx)+(Ey850.*Ezy)+(Ez850.*Ezz)+(Exx+Eyy+Ezz).*Ez850;

%Lorentz term
for n=1:dx-1
    for l=1:dy-1
        for k=1:dz-1
            if abs(nx-index_850(n,l,k)) < 0.001
                LEw=[Ex850(n,l,k),Ey850(n,l,k),Ez850(n,l,k)];
                LHw=[Hx850(n,l,k),Hy850(n,l,k),Hz850(n,l,k)];
                LE2w=[Ex425(n,l,k),Ey425(n,l,k),Ez425(n,l,k)];
                LI=LI+dot(cross(LEw,LHw),LE2w)*(deltax*deltay*deltaz);
            end
        end
    end
end
LII(i)=LI;

%columb term
for n=1:dx-1
    for l=1:dy-1
        for k=1:dz-1
            if abs(nx-index_850(n,l,k)) < 0.001
                KEw=[KEx850(n,l,k),KEy850(n,l,k),KEz850(n,l,k)];
                KE2w=[Ex425(n,l,k),Ey425(n,l,k),-Ez425(n,l,k)];
                KI=KI+dot(KEw,KE2w)*(deltax*deltay*deltaz);
            end
        end
    end
end
KII(i)=KI;

%convective term
for n=1:dx-1
    for l=1:dy-1

```

---

```

        for k=1:dz-1
            if abs(nx-index_850(n,l,k))<0.001
                CEw=[CEx850(n,l,k),CEy850(n,l,k),CEz850(n,l,k)];
                CE2w=[Ex425(n,l,k),Ey425(n,l,k),-Ez425(n,l,k)];
                CI=CI+dot(CEw,CE2w)*(deltax*deltay*deltaz);
            end
        end
    end
end
CII(i)=CI;

    %Each and total SHG terms
LSHG(i)=(1)*R*li*mio*LI;
KSHG(i)=(R*KI)/w;
CSHG(i)=(R*CI)/(w+li*gama);
TSHG(i)=(LSHG(i)+KSHG(i)+CSHG(i));

disp('*****')
pause;
end
%%
    %Output graphs

figure
subplot(4,3,1)
plot(theta,real(LSHG),'*-');
title('|Real Lorentz|')
set(gca,'FontSize',9)
grid on

subplot(4,3,2)
plot(theta,imag(LSHG),'*-');
title('|Imag Lorentz|')
set(gca,'FontSize',9)
grid on

subplot(4,3,3)
plot(theta,abs(LSHG).^2,'*-');
title('|Lorentz|^2')
set(gca,'FontSize',9)
grid on

```

---

```
subplot(4,3,4)
plot(theta,real(CSHG),'*-');
title('|Real Convection|')
set(gca,'FontSize',9)
grid on

subplot(4,3,5)
plot(theta,imag(CSHG),'*-');
title('|Imag Convection|')
set(gca,'FontSize',9)
grid on

subplot(4,3,6)
plot(theta,abs(CSHG).^2,'*-');
title('|Convection|^2')
set(gca,'FontSize',9)
grid on

subplot(4,3,7)
plot(theta,real(KSHG),'*-');
title('|Real Columb|')
set(gca,'FontSize',9)
grid on

subplot(4,3,8)
plot(theta,imag(KSHG),'*-');
title('|Imag Columb|')
set(gca,'FontSize',9)
grid on

subplot(4,3,9)
plot(theta,abs(KSHG).^2,'*-');
title('|Columb|^2')
set(gca,'FontSize',9)
grid on

subplot(4,3,10)
plot(theta,real(TSHG),'*-');
title('|Real Total|')
set(gca,'FontSize',9)
```

```
grid on
```

```
subplot(4,3,11)
plot(theta,imag(TSHG),'*-');
title('|Imag Total|')
set(gca,'FontSize',9)
grid on
```

```
subplot(4,3,12)
plot(theta,abs(TSHG).^2,'*-');
title('|Total|^2')
set(gca,'FontSize',9)
grid on
```

# Bibliography

- [1] Christopher J Orendorff, Anand Gole, Tapan K Sau, and Catherine J Murphy. Surface-enhanced raman spectroscopy of self-assembled monolayers: sandwich architecture and nanoparticle shape dependence. *Analytical chemistry*, 77(10):3261–3266, 2005.
- [2] Fei Le, Daniel W Brandl, Yaroslav A Urzhumov, Hui Wang, Janardan Kundu, Naomi J Halas, Javier Aizpurua, and Peter Nordlander. Metallic nanoparticle arrays: a common substrate for both surface-enhanced raman scattering and surface-enhanced infrared absorption. *ACS nano*, 2(4):707–718, 2008.
- [3] Jesse Theiss, Prathamesh Pavaskar, Pierre M Echternach, Richard E Muller, and Stephen B Cronin. Plasmonic nanoparticle arrays with nanometer separation for high-performance sers substrates. *Nano letters*, 10(8):2749–2754, 2010.
- [4] SG Lipson, H Lipson, and DS Tannhauser. Optical physics. *OptPN*, 7(2):59, 1996.
- [5] EGPA Franken, Alan E Hill, CW Peters, and G Weinreich. Generation of optical harmonics. *Physical Review Letters*, 7(4):118, 1961.
- [6] Feng Wang and Y Ron Shen. General properties of local plasmons in metal nanostructures. *Physical review letters*, 97(20):206806, 2006.

- [7] Jon A Schuller, Edward S Barnard, Wenshan Cai, Young Chul Jun, Justin S White, and Mark L Brongersma. Plasmonics for extreme light concentration and manipulation. *Nature Materials*, 9(3):193, 2010.
- [8] PJ Schuck, DP Fromm, A Sundaramurthy, GS Kino, and WE Moerner. Improving the mismatch between light and nanoscale objects with gold bowtie nanoantennas. *Physical review letters*, 94(1):017402, 2005.
- [9] Peter Muehlschlegel, H-J Eisler, Olivier JF Martin, B Hecht, and DW Pohl. Resonant optical antennas. *science*, 308(5728):1607–1609, 2005.
- [10] Mark I Stockman. Nanofocusing of optical energy in tapered plasmonic waveguides. *Physical review letters*, 93(13):137404, 2004.
- [11] Ewold Verhagen, Marko Spasenović, Albert Polman, and L Kobus Kuipers. Nanowire plasmon excitation by adiabatic mode transformation. *Physical review letters*, 102(20):203904, 2009.
- [12] Younan Xia and Naomi J Halas. Shape-controlled synthesis and surface plasmonic properties of metallic nanostructures. *MRS bulletin*, 30(5):338–348, 2005.
- [13] Stefan Alexander Maier. *Plasmonics: fundamentals and applications*. Springer Science & Business Media, 2007.
- [14] Quanbo Jiang. *Realization and optimization of plasmonic structures for directional control of light*. PhD thesis, 2016.
- [15] H. A. Bethe. Theory of diffraction by small holes. *Physical Review*, 66:163–182, Oct 1944.
- [16] Reuven Gordon. Bethe’s aperture theory for arrays. *Physical Review A*, 76(5):053806, 2007.

- [17] Cyriaque Genet and Thomas W Ebbesen. Light in tiny holes. In *Nanoscience And Technology: A Collection of Reviews from Nature Journals*, pages 205–212. World Scientific, 2010.
- [18] David M Pozar. *Microwave engineering*. John wiley & sons, 2009.
- [19] Thomas W Ebbesen, H J Lezec, HF Ghaemi, Tineke Thio, and PA Wolff. Extraordinary optical transmission through sub-wavelength hole arrays. *Nature*, 391(6668):667, 1998.
- [20] A Lesuffleur, LKS Kumar, and R Gordon. Apex-enhanced second-harmonic generation by using double-hole arrays in a gold film. *Physical Review B*, 75(4):045423, 2007.
- [21] Antoine Lesuffleur, L Kiran Swaroop Kumar, and Reuven Gordon. Enhanced second harmonic generation from nanoscale double-hole arrays in a gold film. *Applied Physics Letters*, 88(26):261104, 2006.
- [22] Fatemeh Eftekhari and Reuven Gordon. Enhanced second harmonic generation from noncentrosymmetric nanohole arrays in a gold film. *IEEE Journal of Selected Topics in Quantum Electronics*, 14(6):1552–1558, 2008.
- [23] Marc Airola, Yongdong Liu, and Steve Blair. Second-harmonic generation from an array of sub-wavelength metal apertures. *Journal of Optics A: Pure and Applied Optics*, 7(2):S118, 2005.
- [24] Tingjun Xu, Xiaojin Jiao, and Steve Blair. Third-harmonic generation from arrays of sub-wavelength metal apertures. *Optics Express*, 17(26):23582–23588, 2009.



- [25] Alexandre G Brolo, Erin Arctander, Reuven Gordon, Brian Leathem, and Karen L Kavanagh. Nanohole-enhanced raman scattering. *Nano Letters*, 4(10):2015–2018, 2004.
- [26] Jason R Anema, Alexandre G Brolo, Pramodha Marthandam, and Reuven Gordon. Enhanced raman scattering from nanoholes in a copper film. *The Journal of Physical Chemistry C*, 112(44):17051–17055, 2008.
- [27] Thomas H Reilly, Shih-Hui Chang, Jordan D Corbman, George C Schatz, and Kathy L Rowlen. Quantitative evaluation of plasmon enhanced raman scattering from nanoaperture arrays. *The Journal of Physical Chemistry C*, 111(4):1689–1694, 2007.
- [28] Mohamed S Fouad, Mohamed Nady, AbdelHamid AbdelMonem Shaalan, et al. Extraordinary optical transmission through single sub-wavelength slot nano antennas. *Optics and Photonics Journal*, 9(07):112, 2019.
- [29] Cheng-ping Huang, Qian-jin Wang, and Yong-yuan Zhu. Dual effect of surface plasmons in light transmission through perforated metal films. *Physical Review B*, 75(24):245421, 2007.
- [30] Hanwei Gao, Joel Henzie, and Teri W Odom. Direct evidence for surface plasmon-mediated enhanced light transmission through metallic nanohole arrays. *Nano letters*, 6(9):2104–2108, 2006.
- [31] A Degiron, HJ Lezec, N Yamamoto, and TW Ebbesen. Optical transmission properties of a single subwavelength aperture in a real metal. *Optics Communications*, 239(1-3):61–66, 2004.
- [32] Reuven Gordon and Alexandre G Brolo. Increased cut-off wavelength for a subwavelength hole in a real metal. *Optics Express*, 13(6):1933–1938, 2005.

- [33] R Gordon, AG Brolo, A McKinnon, A Rajora, B Leathem, and KL Kavanagh. Strong polarization in the optical transmission through elliptical nanohole arrays. *Physical review letters*, 92(3):037401, 2004.
- [34] KJ Klein Koerkamp, Stefan Enoch, Franciscus B Segerink, NF Van Hulst, and L Kuipers. Strong influence of hole shape on extraordinary transmission through periodic arrays of subwavelength holes. *Physical review letters*, 92(18):183901, 2004.
- [35] David R Smith, Willie J Padilla, DC Vier, Syrus C Nemat-Nasser, and Seldon Schultz. Composite medium with simultaneously negative permeability and permittivity. *Physical review letters*, 84(18):4184, 2000.
- [36] Yongmin Liu and Xiang Zhang. Metamaterials: a new frontier of science and technology. *Chemical Society Reviews*, 40(5):2494–2507, 2011.
- [37] Rodger M Walser. Electromagnetic metamaterials. In *Complex Mediums II: Beyond Linear Isotropic Dielectrics*, volume 4467, pages 1–16. International Society for Optics and Photonics, 2001.
- [38] David R Smith. What are electromagnetic metamaterials? *Novel Electromagnetic Materials*, 2009.
- [39] Benny Walther, Christian Helgert, Carsten Rockstuhl, Frank Setzpfandt, Falk Eilenberger, Ernst-Bernhard Kley, Falk Lederer, Andreas Tünnermann, and Thomas Pertsch. Photonics: Spatial and spectral light shaping with metamaterials (adv. mater. 47/2012). *Advanced Materials*, 24(47):6251–6251, 2012.
- [40] Jianxiong Li, Shuqi Chen, Haifang Yang, Junjie Li, Ping Yu, Hua Cheng, Changzhi Gu, Hou-Tong Chen, and Jianguo Tian. Metasurfaces: Simultaneous

- control of light polarization and phase distributions using plasmonic metasurfaces (adv. funct. mater. 5/2015). *Advanced Functional Materials*, 25(5):824–824, 2015.
- [41] Nanfang Yu and Federico Capasso. Flat optics with designer metasurfaces. *Nature Materials*, 13(2):139, 2014.
- [42] Maxim R Shcherbakov, Polina P Vabishchevich, Alexander S Shorokhov, Katie E Chong, Duk-Yong Choi, Isabelle Staude, Andrey E Miroshnichenko, Dragomir N Neshev, Andrey A Fedyanin, and Yuri S Kivshar. Ultrafast all-optical switching with magnetic resonances in nonlinear dielectric nanostructures. *Nano Letters*, 15(10):6985–6990, 2015.
- [43] Sheng Liu, Michael B Sinclair, Sina Saravi, Gordon A Keeler, Yuanmu Yang, John Reno, Gregory M Peake, Frank Setzpfandt, Isabelle Staude, Thomas Pertsch, et al. Resonantly enhanced second-harmonic generation using iii–v semiconductor all-dielectric metasurfaces. *Nano Letters*, 16(9):5426–5432, 2016.
- [44] Kanghee Lee, Hyun Joo Choi, Jaehyeon Son, Hyun-Sung Park, Jaewook Ahn, and Bumki Min. Thz near-field spectral encoding imaging using a rainbow metasurface. *Scientific Reports*, 5:14403, 2015.
- [45] Xiangang Luo and Teruya Ishihara. Subwavelength photolithography based on surface-plasmon polariton resonance. *Optics Express*, 12(14):3055–3065, 2004.
- [46] Changtao Wang, Wei Zhang, Zeyu Zhao, Yanqin Wang, Ping Gao, Yunfei Luo, and Xiangang Luo. Plasmonic structures, materials and lenses for optical lithography beyond the diffraction limit: a review. *Micromachines*, 7(7):118, 2016.
- [47] Dongxing Wang, Wenqi Zhu, Michael D Best, Jon P Camden, and Kenneth B Crozier. Wafer-scale metasurface for total power absorption, local field en-

- hancement and single molecule raman spectroscopy. *Scientific Reports*, 3:2867, 2013.
- [48] Bongseok Choi, Masanobu Iwanaga, Yoshimasa Sugimoto, Kazuaki Sakoda, and Hideki T Miyazaki. Selective plasmonic enhancement of electric-and magnetic-dipole radiations of er ions. *Nano letters*, 16(8):5191–5196, 2016.
- [49] Francesco Monticone, Nasim Mohammadi Estakhri, and Andrea Alù. Full control of nanoscale optical transmission with a composite metascreen. *Physical Review Letters*, 110(20):203903, 2013.
- [50] HL Zhu, SW Cheung, Kwok Lun Chung, and Tong I Yuk. Linear-to-circular polarization conversion using metasurface. *IEEE Transactions on Antennas and Propagation*, 61(9):4615–4623, 2013.
- [51] JP Balthasar Mueller, Noah A Rubin, Robert C Devlin, Benedikt Groever, and Federico Capasso. Metasurface polarization optics: independent phase control of arbitrary orthogonal states of polarization. *Physical Review Letters*, 118(11):113901, 2017.
- [52] Euclides Almeida, Guy Shalem, and Yehiam Prior. Subwavelength nonlinear phase control and anomalous phase matching in plasmonic metasurfaces. *Nature Communications*, 7:10367, 2016.
- [53] Omri Wolf, Salvatore Campione, Alexander Benz, Arvind P Ravikumar, Sheng Liu, Ting S Luk, Emil A Kadlec, Eric A Shaner, John F Klem, Michael B Sinclair, et al. Phased-array sources based on nonlinear metamaterial nanocavities. *Nature communications*, 6:7667, 2015.
- [54] Nishant Nookala, Jongwon Lee, Mykhailo Tymchenko, J Sebastian Gomez-Diaz, Frederic Demmerle, Gerhard Boehm, Kueifu Lai, Gennady Shvets, Markus-

- Christian Amann, Andrea Alu, et al. Ultrathin gradient nonlinear metasurface with a giant nonlinear response. *Optica*, 3(3):283–288, 2016.
- [55] Daniela Wolf, Thorsten Schumacher, and Markus Lippitz. Shaping the nonlinear near field. *Nature communications*, 7:10361, 2016.
- [56] Shay Keren-Zur, Ori Avayu, Lior Michaeli, and Tal Ellenbogen. Nonlinear beam shaping with plasmonic metasurfaces. *ACS Photonics*, 3(1):117–123, 2015.
- [57] Wei-Lun Hsu, Pin Chieh Wu, Jia-Wern Chen, Ting-Yu Chen, Bo Han Cheng, Wei Ting Chen, Yao-Wei Huang, Chun Yen Liao, Greg Sun, and Din Ping Tsai. Vertical split-ring resonator based anomalous beam steering with high extinction ratio. *Scientific Reports*, 5:11226, 2015.
- [58] Heykel Aouani, Mohsen Rahmani, Miguel Navarro-Cía, and Stefan A Maier. Third-harmonic-upconversion enhancement from a single semiconductor nanoparticle coupled to a plasmonic antenna. *Nature nanotechnology*, 9(4):290, 2014.
- [59] Brian K Canfield, Hannu Husu, Janne Laukkanen, Benfeng Bai, Markku Kuitinen, Jari Turunen, and Martti Kauranen. Local field asymmetry drives second-harmonic generation in noncentrosymmetric nanodimers. *Nano Letters*, 7(5):1251–1255, 2007.
- [60] M Scalora, MA Vincenti, D De Ceglia, V Roppo, M Centini, N Akozbek, and MJ Bloemer. Second-and third-harmonic generation in metal-based structures. *Physical Review A*, 82(4):043828, 2010.
- [61] P Guyot-Sionnest and YR Shen. Local and nonlocal surface nonlinearities for surface optical second-harmonic generation. *Physical Review B*, 35(9):4420, 1987.

- [62] Stefano Cattaneo and Martti Kauranen. Determination of second-order susceptibility components of thin films by two-beam second-harmonic generation. *Optics letters*, 28(16):1445–1447, 2003.
- [63] T Xu, X Jiao, GP Zhang, and S Blair. Second-harmonic emission from sub-wavelength apertures: Effects of aperture symmetry and lattice arrangement. *Optics express*, 15(21):13894–13906, 2007.
- [64] TF Heinz. Nonlinear surface electromagnetic phenomena. *by H.-E. Ponath and GI Stegeman (Elsevier Science Publishers BV, Amsterdam, 1991)* p, 353, 1991.
- [65] NC Panoiu, WEI Sha, DY Lei, and GC Li. Nonlinear optics in plasmonic nanostructures. *Journal of Optics*, 20(8):083001, 2018.
- [66] Fu Xiang Wang, Francisco J Rodríguez, Willem M Albers, Risto Ahorinta, JE Sipe, and Martti Kauranen. Surface and bulk contributions to the second-order nonlinear optical response of a gold film. *Physical Review B*, 80(23):233402, 2009.
- [67] P Guyot-Sionnest, W Chen, and YR Shen. General considerations on optical second-harmonic generation from surfaces and interfaces. *Physical Review B*, 33(12):8254, 1986.
- [68] M Corvi and WL Schaich. Hydrodynamic-model calculation of second-harmonic generation at a metal surface. *Physical Review B*, 33(6):3688, 1986.
- [69] Yong Zeng, Walter Hoyer, Jinjie Liu, Stephan W Koch, and Jerome V Moloney. Classical theory for second-harmonic generation from metallic nanoparticles. *Physical Review B*, 79(23):235109, 2009.

- [70] Daniel Timbrell, Jian Wei You, Yuri S Kivshar, and Nicolae C Panoiu. A comparative analysis of surface and bulk contributions to second-harmonic generation in centrosymmetric nanoparticles. *Scientific reports*, 8(1):1–9, 2018.
- [71] Guillaume Bachelier, J  r  my Butet, Isabelle Russier-Antoine, Christian Jonin, Emmanuel Benichou, and P-F Brevet. Origin of optical second-harmonic generation in spherical gold nanoparticles: Local surface and nonlocal bulk contributions. *Physical Review B*, 82(23):235403, 2010.
- [72] Robert W Boyd, Zhimin Shi, and Israel De Leon. The third-order nonlinear optical susceptibility of gold. *Optics Communications*, 326:74–79, 2014.
- [73] F. Hache, D Ricard, Ch Flytzanis, and U Kreibig. The optical kerr effect in small metal particles and metal colloids: the case of gold. *Applied Physics A*, 47(4):347–357, 1988.
- [74] Ghazal Hajisalem, Dennis K Hore, and Reuven Gordon. Interband transition enhanced third harmonic generation from nanoplasmonic gold. *Optical Materials Express*, 5(10):2217–2224, 2015.
- [75] Markus Lippitz, Meindert A van Dijk, and Michel Orrit. Third-harmonic generation from single gold nanoparticles. *Nano letters*, 5(4):799–802, 2005.
- [76] L Rodr  guez-Sun  , J Trull, C Cojocaru, N Akozbek, D de Ceglia, MA Vincenti, and M Scalora. Harmonic generation from gold nanolayers: an old problem under a new light. *arXiv preprint arXiv:2008.06712*, 2020.
- [77] Periklis Pantazis, James Maloney, David Wu, and Scott E Fraser. Second harmonic generating (shg) nanoprobe for in vivo imaging. *Proceedings of the National Academy of Sciences*, 107(33):14535–14540, 2010.

- [78] Lord Rayleigh. Xviii. on the passage of electric waves through tubes, or the vibrations of dielectric cylinders. *The London, Edinburgh, and Dublin Philosophical Magazine and Journal of Science*, 43(261):125–132, 1897.
- [79] FJ Garcia-Vidal, Esteban Moreno, JA Porto, and L Martin-Moreno. Transmission of light through a single rectangular hole. *Physical review letters*, 95(10):103901, 2005.
- [80] FJ García-Vidal, Luis Martín-Moreno, Esteban Moreno, LKS Kumar, and R Gordon. Transmission of light through a single rectangular hole in a real metal. *Physical Review B*, 74(15):153411, 2006.
- [81] R Gordon, L Kiran Swaroop Kumar, and Alexandre G Brolo. Resonant light transmission through a nanohole in a metal film. *IEEE Transactions on Nanotechnology*, 5(3):291–294, 2006.
- [82] Yuanyuan Chen, Li Yu, Jiasen Zhang, and Reuven Gordon. Effective wavelength scaling of rectangular aperture antennas. *Optics Express*, 23(8):10385–10395, 2015.
- [83] C Ciraci, RT Hill, JJ Mock, Y Urzhumov, AI Fernández-Domínguez, SA Maier, JB Pendry, A Chilkoti, and DR Smith. Probing the ultimate limits of plasmonic enhancement. *Science*, 337(6098):1072–1074, 2012.
- [84] Arvind Sundaramurthy, KB Crozier, GS Kino, DP Fromm, PJ Schuck, and WE Moerner. Field enhancement and gap-dependent resonance in a system of two opposing tip-to-tip au nanotriangles. *Physical Review B*, 72(16):165409, 2005.



- [85] Rucha Deshpande, Anders Pors, and Sergey I Bozhevolnyi. Third-order gap plasmon based metasurfaces for visible light. *Optics Express*, 25(11):12508–12517, 2017.
- [86] Mohammadreza S Nezami, Daehan Yoo, Ghazal Hajisalem, Sang-Hyun Oh, and Reuven Gordon. Gap plasmon enhanced metasurface third-harmonic generation in transmission geometry. *ACS Photonics*, 3(8):1461–1467, 2016.
- [87] Masanobu Iwanaga, Bongseok Choi, Hideki T Miyazaki, and Yoshimasa Sugimoto. The artificial control of enhanced optical processes in fluorescent molecules on high-emittance metasurfaces. *Nanoscale*, 8(21):11099–11107, 2016.
- [88] Alexander Krasnok, Mykhailo Tymchenko, and Andrea Alù. Nonlinear metasurfaces: a paradigm shift in nonlinear optics. *Materials Today*, 21(1):8–21, 2018.
- [89] Mohammadreza Sanadgol Nezami. *Plasmonic Metasurfaces for Enhanced Third Harmonic Generation*. PhD thesis, University of Victoria, 2016.
- [90] RW Boyd. Nonlinear optics 3rd edn (new york: Academic). 2008.
- [91] John David Jackson. *Classical electrodynamics*. John Wiley & Sons, 2007.
- [92] Joseph Larmor. Lxiii. on the theory of the magnetic influence on spectra; and on the radiation from moving ions. *The London, Edinburgh, and Dublin Philosophical Magazine and Journal of Science*, 44(271):503–512, 1897.
- [93] Sudhanshu S Jha. Theory of optical harmonic generation at a metal surface. *Physical Review*, 140(6A):A2020, 1965.
- [94] P Drude and P Drude. The theory of metals ions. *Phys Zeitsch*, 1:161, 1900.

- [95] JO Linde. The effective mass of the conduction electrons in metals and the theory of superconductivity. *Physics Letters*, 11(3):199–201, 1964.
- [96] J Szczyrbowski. A new simple method of determining the effective mass of an electron or the thickness of thin metal films. *Journal of Physics D: Applied Physics*, 19(7):1257, 1986.
- [97] JE Sipe, VCY So, M Fukui, and GI Stegeman. Analysis of second-harmonic generation at metal surfaces. *Physical Review B*, 21(10):4389, 1980.
- [98] Cristian Ciracì, Ekaterina Poutrina, Michael Scalora, and David R. Smith. Origin of second-harmonic generation enhancement in optical split-ring resonators. *Physical Review B*, 85:201403, May 2012.
- [99] Kevin O’Brien, Haim Suchowski, Junsuk Rho, Alessandro Salandrino, Boubacar Kante, Xiaobo Yin, and Xiang Zhang. Predicting nonlinear properties of metamaterials from the linear response. *Nature Materials*, 14(4):379, 2015.
- [100] Jérémy Butet and Olivier JF Martin. Evaluation of the nonlinear response of plasmonic metasurfaces: Miller’s rule, nonlinear effective susceptibility method, and full-wave computation. *JOSA B*, 33(2):A8–A15, 2016.
- [101] Esmail Rahimi and Reuven Gordon. Nonlinear plasmonic metasurfaces. *Advanced Optical Materials*, page 1800274, 2018.
- [102] Sylvie Roke, Mischa Bonn, and Andrei V Petukhov. Nonlinear optical scattering: The concept of effective susceptibility. *Physical Review B*, 70(11):115106, 2004.
- [103] John David Jackson. *Classical Electrodynamics*. John Wiley & Sons, 3 edition, 2012.

- [104] Lev Davidovich Landau, JS Bell, MJ Kearsley, LP Pitaevskii, EM Lifshitz, and JB Sykes. *Electrodynamics of continuous media*, volume 8. elsevier, 2013.
- [105] Mohammadreza S Nezami and Reuven Gordon. Localized and propagating surface plasmon resonances in aperture-based third harmonic generation. *Optics Express*, 23(25):32006–32014, 2015.
- [106] Christoffel Jacob Bouwkamp. Diffraction theory. *Reports on progress in physics*, 17(1):35, 1954.
- [107] Timothy H Boyer. The force on a magnetic dipole. *American Journal of Physics*, 56(8):688–692, 1988.
- [108] Allen Taflove and Susan C Hagness. *Computational electrodynamics: the finite-difference time-domain method*. Artech house, 2005.
- [109] Stephen D Gedney. Introduction to the finite-difference time-domain (fdtd) method for electromagnetics. *Synthesis Lectures on Computational Electromagnetics*, 6(1):1–250, 2011.
- [110] Dennis Sullivan, Jun Liu, and Mark Kuzyk. Three-dimensional optical pulse simulation using the fdtd method. *IEEE transactions on microwave theory and techniques*, 48(7):1127–1133, 2000.
- [111] Kane Yee. Numerical solution of initial boundary value problems involving maxwell’s equations in isotropic media. *IEEE Transactions on antennas and propagation*, 14(3):302–307, 1966.
- [112] Thomas Quinn, Neal Katz, Joachim Stadel, and George Lake. Time stepping n-body simulations. *arXiv preprint astro-ph/9710043*, 1997.

- [113] ConstantineA Balanis. Advanced engineering electromagnetics, john willey & sons. *Inc., New York*, 1989.
- [114] NO Sadiku Matthew. *Numerical techniques in electromagnetics*. CRC Press, 2000.
- [115] Antonino Calà Lesina, Alessandro Vaccari, Pierre Berini, and Lora Ramunno. On the convergence and accuracy of the fdtd method for nanoplasmonics. *Optics Express*, 23(8):10481–10497, 2015.
- [116] Lloyd Nicholas Trefethen. Finite difference and spectral methods for ordinary and partial differential equations. 1996.
- [117] Richard Courant, Kurt Friedrichs, and Hans Lewy. On the partial difference equations of mathematical physics. *IBM journal of Research and Development*, 11(2):215–234, 1967.
- [118] Chris J Railton and John B Schneider. An analytical and numerical analysis of several locally conformal fdtd schemes. *IEEE Transactions on Microwave Theory and Techniques*, 47(1):56–66, 1999.
- [119] Andreas C Cangellaris and Diana B Wright. Analysis of the numerical error caused by the stair-stepped approximation of a conducting boundary in fdtd simulations of electromagnetic phenomena. *IEEE transactions on antennas and propagation*, 39(10):1518–1525, 1991.
- [120] Richard Holland. Pitfalls of staircase meshing. *IEEE Transactions on Electromagnetic Compatibility*, 35(4):434–439, 1993.
- [121] Wenhua Yu and Raj Mittra. A conformal finite difference time domain technique for modeling curved dielectric surfaces. *IEEE Microwave and Wireless Components Letters*, 11(1):25–27, 2001.

- [122] Jean-Pierre Bérenger. Perfectly matched layer (pml) for computational electromagnetics. *Synthesis Lectures on Computational Electromagnetics*, 2(1):1–117, 2007.
- [123] Ramesh Kumar and Anurag Sharma. Absorbing boundary condition (abc) and perfectly matched layer (pml) in numerical beam propagation: a comparison. *Optical and Quantum Electronics*, 51(2):1–13, 2019.
- [124] Peter B Johnson and R-W Christy. Optical constants of the noble metals. *Physical review B*, 6(12):4370, 1972.
- [125] William M Haynes. *CRC handbook of chemistry and physics*. CRC press, 2014.
- [126] DY Smith, E Shiles, Mitio Inokuti, and ED Palik. Handbook of optical constants of solids. *Handbook of Optical Constants of Solids*, 1:369–406, 1985.
- [127] Stefan Linden, Christian Enkrich, Martin Wegener, Jiangfeng Zhou, Thomas Koschny, and Costas M Soukoulis. Magnetic response of metamaterials at 100 terahertz. *Science*, 306(5700):1351–1353, 2004.
- [128] Matthias W Klein, Christian Enkrich, Martin Wegener, and Stefan Linden. Second-harmonic generation from magnetic metamaterials. *Science*, 313(5786):502–504, 2006.
- [129] Roberto Merlin. Metamaterials and the landau–lifshitz permeability argument: Large permittivity begets high-frequency magnetism. *Proceedings of the National Academy of Sciences*, 106(6):1693–1698, 2009.
- [130] Zhichao Ruan and Shanhui Fan. Superscattering of light from subwavelength nanostructures. *Physical Review Letters*, 105(1):013901, 2010.

- [131] Pai-Yen Chen, Christos Argyropoulos, and Andrea Alù. Enhanced nonlinearities using plasmonic nanoantennas. *Nanophotonics*, 1(3-4):221–233, 2012.
- [132] Alessio Benedetti, Marco Centini, Mario Bertolotti, and Concita Sibia. Second harmonic generation from 3d nanoantennas: on the surface and bulk contributions by far-field pattern analysis. *Optics Express*, 19(27):26752–26767, 2011.
- [133] WM Robertson, AL Moretti, and Ralph Bray. Surface-plasmon-enhanced brillouin scattering on silver films: double-resonance effect. *Physical Review B*, 35(17):8919, 1987.
- [134] Pavel N Melentiev, Anton E Afanasiev, Artur A Kuzin, Andrey S Baturin, and Victor I Balykin. Giant optical nonlinearity of a single plasmonic nanostructure. *Optics express*, 21(12):13896–13905, 2013.
- [135] PN Melentiev, TV Konstantinova, AE Afanasiev, AA Kuzin, AS Baturin, AV Tausenev, AV Konyaschenko, and VI Balykin. Single nano-hole as a new effective nonlinear element for third-harmonic generation. *Laser Physics Letters*, 10(7):075901, 2013.
- [136] Nima Kalhor, Stuart A Boden, and Hiroshi Mizuta. Sub-10 nm patterning by focused he-ion beam milling for fabrication of downscaled graphene nano devices. *Microelectronic Engineering*, 114:70–77, 2014.
- [137] Xiaoshu Chen, Cristian Ciraci, David R Smith, and Sang-Hyun Oh. Nanogap-enhanced infrared spectroscopy with template-stripped wafer-scale arrays of buried plasmonic cavities. *Nano letters*, 15(1):107–113, 2014.
- [138] R Stosch, F Yaghobian, T Weimann, RJC Brown, MJT Milton, and B Güttler. Lithographical gap-size engineered nanoarrays for surface-enhanced raman probing of biomarkers. *Nanotechnology*, 22(10):105303, 2011.

- [139] Ana Zehtabi-Oskuie, Aurora A Zinck, Ryan M Gelfand, and Reuven Gordon. Template stripped double nanohole in a gold film for nano-optical tweezers. *Nanotechnology*, 25(49):495301, 2014.
- [140] Ghazal Hajisalem, Aftab Ahmed, Yuanjie Pang, and Reuven Gordon. Plasmon hybridization for enhanced nonlinear optical response. *Optics Express*, 20(28):29923–29930, 2012.
- [141] JAH Van Nieuwstadt, M Sandtke, RH Harmsen, Franciscus B Segerink, JC Prangma, Stefan Enoch, and L Kuipers. Strong modification of the nonlinear optical response of metallic subwavelength hole arrays. *Physical Review Letters*, 97(14):146102, 2006.
- [142] Peter Schön, Nicolas Bonod, Eloïse Devaux, Jérôme Wenger, Hervé Rigneault, Thomas W Ebbesen, and Sophie Brasselet. Enhanced second-harmonic generation from individual metallic nanoapertures. *Optics Letters*, 35(23):4063–4065, 2010.
- [143] Tiberiu-Dan Onuta, Matthias Waegle, Christopher C DuFort, William L Schaich, and Bogdan Dragnea. Optical field enhancement at cusps between adjacent nanoapertures. *Nano Letters*, 7(3):557–564, 2007.
- [144] Hua Lu, Xueming Liu, Renlong Zhou, Yongkang Gong, and Dong Mao. Second-harmonic generation from metal-film nanohole arrays. *Applied Optics*, 49(12):2347–2351, 2010.
- [145] Kitsakorn Locharoenrat. Second harmonic generation based on strong field enhancement in metallic nanostructured surface. *Materials Science*, 20(4):387–391, 2014.

- [146] Jongwon Lee, Nishant Nookala, J Sebastian Gomez-Diaz, Mykhailo Tymchenko, Frederic Demmerle, Gerhard Boehm, Markus-Christian Amann, Andrea Alù, and Mikhail A Belkin. Ultrathin second-harmonic metasurfaces with record-high nonlinear optical response. *Advanced Optical Materials*, 4(5):664–670, 2016.
- [147] Fu Xiang Wang, Francisco J Rodriguez, Hannu Husu, and Martti Kauranen. Second-order nonlinear optical properties of metal nanostructures and metamaterials. *Nonlinear Opt. Quantum Opt.*, 40:43–56, 2010.
- [148] Christos Argyropoulos, Giuseppe D’Aguanno, and Andrea Alu. Giant second-harmonic generation efficiency and ideal phase matching with a double  $\varepsilon$ -near-zero cross-slit metamaterial. *Physical Review B*, 89(23):235401, 2014.
- [149] K Liu, L Zhan, ZY Fan, MY Quan, SY Luo, and YX Xia. Enhancement of second-harmonic generation with phase-matching on periodic sub-wavelength structured metal film. *Optics Communications*, 276(1):8–13, 2007.
- [150] Brian K Canfield, Sami Kujala, Konstantins Jefimovs, Yuri Svirko, Jari Tuunanen, and Martti Kauranen. A macroscopic formalism to describe the second-order nonlinear optical response of nanostructures. *Journal of Optics A: Pure and Applied Optics*, 8(4):S278, 2006.
- [151] EH Barakat, M-P Bernal, and FI Baida. Second harmonic generation enhancement by use of annular aperture arrays embedded into silver and filled by lithium niobate. *Optics Express*, 18(7):6530–6536, 2010.
- [152] Ben-Li Wang, Rui Wang, RJ Liu, XH Lu, Jimin Zhao, and Zhi-Yuan Li. Origin of shape resonance in second-harmonic generation from metallic nanohole arrays. *Scientific Reports*, 3(1):1–8, 2013.



- [153] Wenjun Fan, Shuang Zhang, KJ Malloy, SRJ Brueck, NC Panoiu, and RM Osgood. Second harmonic generation from patterned gaas inside a subwavelength metallic hole array. *Optics Express*, 14(21):9570–9575, 2006.
- [154] Wenjun Fan, Shuang Zhang, N-C Panoiu, A Abdenour, S Krishna, RM Osgood, KJ Malloy, and SRJ Brueck. Second harmonic generation from a nanopatterned isotropic nonlinear material. *Nano Letters*, 6(5):1027–1030, 2006.
- [155] MC Hughes and R Gordon. Optical transmission properties and enhanced loss for randomly positioned apertures in a metal film. *Applied Physics B*, 87(2):239–242, 2007.
- [156] Maxim Durach, Anastasia Rusina, and Mark I Stockman. Giant surface-plasmon-induced drag effect in metal nanowires. *Physical Review Letters*, 103(18):186801, 2009.
- [157] Arvind S Vengurlekar and Teruya Ishihara. Surface plasmon enhanced photon drag in metal films. *Applied Physics Letters*, 87(9):091118, 2005.
- [158] Reuven Gordon. Surface plasmon nanophotonics: a tutorial. *IEEE Nanotechnology magazine*, 2(3):12–18, 2008.